THE SYNAPTIC MECHANISMS UNDERLYING BINAURAL INTERACTIONS IN RAT AUDITORY CORTEX

by

MICHAEL KYWERIGA

A DISSERTATION

Presented to the Department of Biology
and the Graduate School of the University of Oregon
in partial fulfillment of the requirements
for the degree of
Doctor of Philosophy

June 2014

DISSERTATION APPROVAL PAGE

Student: Michael Kyweriga

Title: The Synaptic Mechanisms Underlying Binaural Interactions in Rat Auditory Cortex

This dissertation has been accepted and approved in partial fulfillment of the requirements for the Doctor of Philosophy degree in the Department of Biology by:

Judith Eisen	Chairperson
Michael Wehr	Advisor
Shawn Lockery	Core Member
Phillip Washbourne	Core Member
Clifford Kentros	Institutional Representative

and

Kimberly Andrews Espy	Vice President for Research and Innovation; Dean of the Graduate School

Original approval signatures are on file with the University of Oregon Graduate School.

Degree awarded June 2014

© 2014 Michael Kyweriga

DISSERTATION ABSTRACT

Michael Kyweriga

Doctor of Philosophy

Department of Biology

June 2014

Title: The Synaptic Mechanisms Underlying Binaural Interactions in Rat Auditory Cortex

The interaural level difference (ILD) is a sound localization cue first computed in the lateral superior olive (LSO) by comparing the loudness of sounds between the two ears. In the auditory cortex, one class of neurons is excited by contralateral but not ipsilateral monaural sounds. These “EO” neurons prefer ILDs where contralateral sounds are louder than ipsilateral sounds. Another class, the “PB” neurons, are unresponsive to monaural sounds but respond predominantly to binaural ILDs, when both ears receive simultaneous sounds of roughly equal loudness (0 ILD).

Behavioral studies show that ILD sensitivity is invariant to increasing sound levels. However, in the LSO, ILD response functions shift towards the excitatory ear as sound level increases, indicating level-dependence. Thus, changes in firing rate can indicate either a change in sound location or sound level, or both. This suggests a transformation in level-sensitivity between the LSO and the perception of sound sources, yet the location of this transformation remains unknown. I performed recordings in the auditory cortex of the rat to test whether neurons were invariant to overall sound level. I found that with increasing sound levels, ILD responses were level-dependent, suggesting that level invariance of ILD sensitivity is not present in the rat auditory cortex.

In general, neurons follow one of two processing strategies. The tuning of cortical cells typically follows the “inheritance strategy”, such that the spiking output of the cell matches that of the excitatory synaptic input. However, cortical tuning can be modified by inhibition in the “local processing strategy”. In this case, neurons are prevented from spiking at non-preferred stimuli by inhibition that overwhelms excitation. The tuning strategy of cortical neurons to ILD remains unknown. I performed whole-cell recordings in the anesthetized rat and compared the spiking output with synaptic inputs to ILDs within the same neurons. I found that the PB neurons showed evidence of the local processing strategy, which is a novel role for cortical inhibition, whereas the EO neurons utilized the inheritance strategy. This result suggests that an auditory cortical circuit computes sensitivity for midline ILDs.

This dissertation includes previously published/unpublished co-authored material.

CURRICULUM VITAE

NAME OF AUTHOR: Michael Kyweriga

GRADUATE AND UNDERGRADUATE SCHOOLS ATTENDED:

University of Oregon, Eugene, OR
University of California, Santa Cruz, CA
Copper Mountain College, Joshua Tree, CA

DEGREES AWARDED:

Doctor of Philosophy in Biology, Systems Neuroscience emphasis, 2014, University of Oregon, Eugene, OR

Bachelor of Arts in Psychology with Biology minor, 2006, University of California, Santa Cruz, CA

AREAS OF SPECIAL INTEREST:

Auditory system
Sound localization
Neurophysiology
Quantitative analysis of information with Matlab
Visual display of information with Matlab
Animal behavior
Tinnitus
Autism

PROFESSIONAL EXPERIENCE:

Doctoral Candidate, Wehr Lab, Department of Biology, University of Oregon, Eugene, OR, 2009 - 2014

Graduate Teaching Fellow, Department of Biology, University of Oregon, Eugene, OR, 2012 - 2014

Graduate Research Fellow, Wehr Lab, Department of Biology, University of Oregon, Eugene, OR, 2008 - 2012

Graduate Teaching Fellow, Department of Biology, University of Oregon, Eugene, OR, 2007 - 2008

Research Technician, Bermingham Lab, McLaughlin Research Institute, Great Falls, MT, February - May 2007

Undergraduate Scholar, Summer Program for Undergraduate Research, Dassonville Lab, University of Oregon, Eugene, OR, June - September 2006

Undergraduate Field Study, Co-advised by Dr. Fox-Tree and Dr. Long, The Bay School, Santa Cruz, CA, 2005 - 2006

Peer Mentor, Academic Excellence Program, University of California, Santa Cruz, CA, 2003 - 2006

Direct Support Professional, Listen Foundation, Santa Cruz, CA, 2002 - 2004

GRANTS, AWARDS, AND HONORS:

Donald E. Wimber Travel Fund, *Synaptic computation of interaural level differences in rat auditory cortex*, Department of Biology, University of Oregon, 2014

Computational Systems Neuroscience Travel Grant, *Synaptic computation of interaural level differences in rat auditory cortex*, University of Rochester, 2014

Teacher Recognition Award, Department of Biology, University of Oregon, 2013

Veterans Educational Aid, Oregon Department of Veterans Affairs, 2010 - 2014

Naturalized Citizen of the United States of America, March 2010

Post-9/11 GI Bill, US Department of Veterans Affairs, 2010

Systems Training Grant, *Electrophysiological and behavioral characterization of a mouse model for autism spectrum disorders*, Institute of Neuroscience, University of Oregon, 2008 - 2010

Montgomery GI Bill, US Department of Veterans Affairs, 2002 - 2006

Psi Chi National Honor Society in Psychology, 2005

Dean's List, Four Awards, University of California, Santa Cruz, 2004 - 2006

US Navy and Marine Corps Achievement Medal with Gold Star, 2002

US National Defense Service Medal, 2002

US Navy Good Conduct Medal, 2000

National Honor Society, 1996

PUBLICATIONS:

Kyweriga M, Stewart W, Cahill C, Wehr M. Synaptic mechanisms underlying interaural level difference selectivity in rat auditory cortex. *J Neurophysiol*: under first review.

Kyweriga M, Stewart W, Wehr M. Neuronal interaural level difference response shifts are level-dependent in the rat auditory cortex. *J Neurophysiol* 111: 930-938, 2014.

Hoy JL, Haeger PA, Constable JRL, Arias RJ, McCallum R, Kyweriga M, Davis L, Schnell E, Wehr M, Castillo PE, Washbourne P. Neuroligin1 drives synaptic and behavioral maturation through intracellular interactions. *J Neurosci* 33: 9364-9384, 2013.

Kyweriga, M, Stewart W, Cahill C, Wehr M. Inhibitory shaping of binaural response properties in rat auditory cortex. *Society for Neuroscience Abstract Viewer and Itinerary Planner* 42, 2012.

Kyweriga, M, Wolfe W, Cahill C, Wehr M. Synaptic mechanisms of binaural interactions in rat primary auditory cortex. *Society for Neuroscience Abstract Viewer and Itinerary Planner* 40, 2010.

Wehr M, Hostick U, Kyweriga M, Tan A, Weible AP, Wu H, Wu W, Callaway EM, Kentros C. Transgenic silencing of neurons in the mammalian brain by expression of the Allatostatin receptor (AlstR). *J Neurophysiol* 102: 2554-2562, 2009. (Corrigendum. *J Neurophysiol* 102: 3781-3781, 2009).

Bermingham J, Pennington J, Shearin H, Kyweriga M, Jaegle M, Driegen S, van Zon A, Darbas A, Ozkaynak E, Sirkowsky E, Scherer SS, Meijer D. The secreted protein Lgi4 is required for peripheral nerve development. *Society for Neuroscience Abstract Viewer and Itinerary Planner* 38, 2008.

ACKNOWLEDGMENTS

I wish to express sincere appreciation to Professor Mike Wehr for teaching me *in vivo* whole-cell electrophysiology, programming and data analysis in Matlab, writing excellently, and how to be a great scientist and mentor. With gratitude, I thank my Wehr-do labmates Whitney Stewart, Alexandra Moore, Aldis Weible, Iryna Yavorska, and Alex Gusev for thoughtful discussions about experiments, data analysis, and science in general. On this list I would also like to include Cris Niell, Santiago Jaramillo, Jennifer Hoy, Joe Wekselblatt, Liza Yanovick, Leah DeBlander, and Dave Rowland. I am also very grateful for the University of Oregon Animal Care Services for taking exceptional care of our lab animals, especially Jessica Stark, Sylvia Banks, Monte Matthews, Alex Ojerio, Jenny Perez, and Molly Basney. And thank you Allie for keeping close watch on the Wehr-do colony. I thank my dissertation advisory committee: Shawn Lockery, Judith Eisen, Phil Washbourne, and Cliff Kentros; Peter O'Day and the Summer Program for Undergraduate Research; Mark Carrier, Elly Vandegrift, and the UO Science literacy program; The Institute of Neuroscience, Peg Morrow, Ellen McCumsey, Mikel Rhodes, JoLynn Burrett, Don Pate, Mike McHorse, and Terry Winn; The Biology department support staff: Annie Rogers, Jessica Wilson, and Lynne Romans; and to my fellow Wehr-dos both past and present: Xiang Gao, Ben Scholl, Katelyn Dufour-O'Brien, Whitney Stewart, Andrew Tan, Nathan Montgomery, Maddie Norman, Taryn Gillies, Katherine Tomscha, Carolyn Cahill, Lucas Ott, Conor O'Sullivan, Christine Liu, and Kit Maston.

I am honored to have wonderful friends and family keeping me sane through all the long days and nights. With gratitude I thank my Calvin ST roommates whom I rarely

saw, but who always made me feel at home: Alanna Young, Gabriel Yospin, Conor O'Brien, Ida Moadab, Nic Kooyers, Daniel Zhang, and Hagen Hammonds. I thank team ION: Crystal Davey-Hicks (H^+), Liesl McCormick (Li^+), Kat McCormick (Ca^{2+}), and Kelly Heinlein (K^+). I thank my football friends, who were excellent travel companions both to out of state games as well as over the footbridge to Autzen stadium: Christi Hutchinson, Kate Karfilis, Matt Shurtleff, and Levi and Chelsea Simonson. I thank my dear friends, Jason, Cyrus and Carol Yocum, Emily Bass, Brett Fletcher, Brandy Emanuel-Fletcher, Thu Tran, Nilo Alvarado, Xavier Rubio, Erika Elvert, David Courtney, Helen Tauc, Omer Bayraktar, Sarah, Louis, and Glenda Dashofy, Travis and Carrie Carney, Joe Hall, Liesl and Chris McCormick, Diedra Case and Jeff Zimmerman.

Last but not least, I thank my family for supporting me throughout my entire education. To father Raymond, for insisting I "look it up" from a very young age; to my step-mother Karla, for teaching me to write the way I speak; to my sister Andrea, for always supporting me; to my sister Jamie, for teaching me to speak my mind; to my brother Alex and my mother Denice; and to my niece and nephews Alexis, Jayse, and Joel who remind me to remain forever curious about the world around me.

This work was supported by the National Institutes of Health 1R01DC011379, National Institute of Mental Health R01 MH081935 and R21 076289, American Psychological Association DPN T32 MH18882-22, National Institute of Neurological Disorders and Stroke R01 NS065795, Autism Speaks 1368, the Whitehall Foundation, National Science Foundation GK-12 program, DOD W81XWH-07-2-0092, the Oregon Center for Optics and the Post-9/11 Montgomery GI Bill.

For my family, who understand my busy scientific life and love me
just the way I am.

And for Alanna Vale, who patiently listens to my scientific orations.
Thanks to you, I am beginning to understand.

TABLE OF CONTENTS

LIST OF FIGURES

Figure Page

CHAPTER I

INTRODUCTION: BRIEF OVERVIEW OF SOUND LOCALIZATION AND NEURAL CODING IN THE AUDITORY CORTEX

Animal nervous systems are specialized to respond to a variety of sensory information. Sound can be extremely valuable for detecting prey, predators, and conspecifics. The ears collect sound waves which are then converted into electrical signals by the cochlea of the inner ear. Circuits in the auditory pathway extract location information and compare it with other sensory inputs and past experience.

For my dissertation I sought to elucidate the role of cortical neurons encoding the interaural level difference of binaural sounds. Chapter II contains previously published work by myself, Whitney Stewart, and Mike Wehr in which we show that rat cortical neurons are level-dependent to the interaural level difference cue. Chapter III contains work currently under review for publication by myself, Whitney Stewart, Carolyn Cahill, and Mike Wehr, where we show distinct processing strategies of cortical neurons encoding sound location information. From my work on these two projects I became trained in *in vivo* whole-cell electrophysiology, which enabled me to provide assistance on two other projects within the Institute of Neuroscience. Appendix A contains previously published work by myself, Jennifer Hoy, Paola Haeger, John Constable, Renee Arias, Raluca McCallum, Lawrence Davis, Eric Schnell, Mike Wehr, Pablo Castillo, and Philip Washbourne. For this project I contributed valuable insight into the behavioral and neurophysiological changes to transgenic mice with altered Neuroligin1 synaptic proteins. Appendix B contains previously published work by myself, Mike Wehr, Ute Hostick, Andrew Tan, Aldis Weible, Haiyan Wu, Wendy Wu, Edward Callaway, and Cliff Kentros. For this project I demonstrated reversible silencing of cortical sensory neuron responses to sounds with the Allatostatin-tetO system. This is now a useful tool in the study of neuronal circuits.

Sound Localization Cues

Locating the source of a sound is a primary functions of the auditory system. Sound localization enables an individual to locate threats, prey, and conspecifics in the absence of visual or olfactory signals. The precision of sound localization varies across species and depends upon how critical it is for the survival of the individual. For example, in some species such as the pallid bat, their sound localization must be exquisitely accurate to enable hunting in complete darkness. In other species such as the rat, sound localization is useful for predator avoidance, but it is not critical for finding food. To locate a sound source, mammals utilize three main cues: (1) The interaural level difference (ILD) cue is a comparison of the relative loudness between the two ears, (2) The interaural time difference (ITD) cue is a comparison between the relative timing of sounds reaching the two ears, and (3) The head-related transfer function (HRTF) is the unique frequency distortion of sounds traveling past the head and pinna (For review see Grothe et al. 2010). Together these three cues combine to provide the listener with an estimate of the location of the sound source with respect to the self.

The interaural time difference cue

The interaural time difference (ITD) cue conveys information of low frequency sounds on the horizontal azimuth. For example, a pure tone played on the left side of a listener’s head will reach the left ear before the right ear. Neurons in the cochlear nucleus are tuned to a specific phase angle of a sinusoidal pure tone. The phase angle encoded by neurons in the cochlear nucleus of each ear are compared to each other in the medial superior olivary (MSO) complex in the brainstem. Due to the length of time needed for a sound to travel from the left ear to the right ear, when a sound is played on the left side of the listener’s head, the phase angle arriving at each ear is slightly offset in time. Thus, the interaural time difference can provide information about the location of a sound source on the horizontal azimuth. Large ITDs denote a sound coming from the extreme left or right side of the head, while ITDs near zero denote a sound coming from the midline. It is important to note that ITDs are limited to frequencies less than the distance between the two ears of a listener. For example, a human listener has an inter-ear distance of about 15 cm and the speed of sound at sea level is 340 m/s. A sound to traveling from the left to right ear takes about 440 us. This corresponds to approximately 2.3 kHz and since neurons are tuned to the absolute value of the phase angle, the upper limit of useful ITDs is approximately 1150 Hz. For frequencies that are greater than one half of the listener’s head size, the phase locking to these higher frequencies becomes ambiguous to the listener and the cue loses its effectiveness. Sounds above this physical limit however, are more strongly affected by the head shadowing effect.

The interaural level difference cue

The interaural level difference (ILD) is a useful cue for comparing high frequency sounds that are above the physical limit of the interaural time difference. As sounds increase in frequency they become more susceptible to attenuation by the head, fur, and pinna. This is due to the physical diffraction of sound waves. For a single object, lower frequencies can more easily bend around the object, whereas higher frequencies cannot and are more attenuated by diffraction. This is why a home theater surround sound setup must have the high frequency tweeters pointed directly at the couch. However, the low frequency subwoofer can simply be put in a corner under an end table.

The difference in sound levels received by the two ears is compared in the lateral superior olivary (LSO) complex of the brainstem. The loudness of a sound is encoded by higher spike rates in the cochlear nucleus. These signals are delivered to the LSO and compared between the left and right ears. The difference in sound level between the two ears then provides an estimate of the location of the sound on the horizontal azimuth.

Together the ITD and ILD work together to determine the location of a sound source on the horizontal azimuth. While higher frequency sounds are attenuated by the head, this reduction in sound level only occurs for higher frequency sounds. Thus, there is a small range of frequencies where both ITD and ILD fail. Fortunately this is a small range of frequencies and pure tones are rarely observed in nature.

The head related transfer function

A third sound localization cue is the head related transfer function (HRTF), which assists in localizing the elevation of sounds. For this cue the shape of the listener's head, fur, and pinna provide important spectral information about sounds. Specifically, when presented with a range of frequencies all at the same intensity, the sound is distorted and amplified by the pinna of each ear. These distortions are called spectral notches and they are unique to each ear. Furthermore, spectral notches change with the location of the elevation of a sound source. This means that the spectral notches of a range of frequencies to a particular ear changes as the speaker is moved from high to low elevations.

Unlike the binaural ITD and ILD cues discussed above, the HRTF is primarily a monaural cue. Neurons in the dorsal cochlear nucleus (DCN) receive direct monaural inputs from the auditory nerve fibers from each cochlea. Type IV cells in the DCN are particularly receptive to specific frequencies at low intensities. Since the type IV cells project to type O cells in the IC, they are also responsive to the same frequencies at low intensities. When broadband noise is played to type IV cells, they respond robustly to spectral notches except those near the cell's best frequency, which causes a strong suppression of firing especially at louder sound levels. When the same broadband noise with spectral notches is played to type O neurons in the IC, they respond in an opposite manner as type IV cells. The type O cells instead respond robustly to the spectral notch at their preferred frequency. This forms the basis for directional sensitivity to spectral notches on the elevation axis.

Integration of sound localization cues

Sound source localization cues from the ITD, ILD, and HRTF all converge onto the IC through separate streams. The IC sends projections to the superior colliculus (SC), which is an area of the brain that is responsible for directing eye, arm, other body movements, as well as directing attention (for review, see Arnott and Alain 2011). Connecting body movements, especially those of the eyes, head, and attention are helpful in identifying a sound source. Other reports show evidence that the parietal cortex is responsible for shaping a map of auditory space to ego-centric coordinates that can be used by the visual system (Gherri et al. 2008; Stricanne et al. 1996). Heffner (2004) shows evidence that the ability of mammals to localize sounds is correlated with the best field of vision. At one extreme, mammalian species with high visual acuity have excellent sound localization, for example cats and primates. Whereas mammals with poor visual acuity have weak sound localization ability, such as mice and rats. This correlation is striking with an $r = 0.89$ in the 23 mammalian species studied. While animals with poor visual acuity and sound localization, these species are still able to work with what they have. Meaning that even with poor sound localization and visual acuity, they still orient towards sounds in their environment. Therefore, regardless of the ability of mammals to visually orient towards targets in their environment, sound localization plays a strong role in their lives and increases their chances for survival.

Localizing Sounds of Varying Loudness

In the macaque (Recanzone and Beckerman 2004) and human (Altshuler and Comalli 1975), sound localization is independent of the overall sound level of the source. In physiological studies neurons in the LSO are dependent on the overall level of the sound source (Tsai et al. 2010) when measuring ILD response functions. This means that as the sound level of a source increases, neurons respond as though the sound location is changing. In the bat inferior colliculus there is a mix of results with some cells showing invariance and others showing level dependence (Park et al. 2004) to ILD cues. Using free-field sounds, the auditory cortex appears to show invariance to overall sound level in the cat (Mickey and Middlebrooks 2003), pallid bat (Razak 2011), and marmoset (Zhou and Wang 2012). Due to this result we expected to show level-invariance in the rat auditory cortex. However, we were surprised to find that rat auditory cortical neurons are level-dependent (see Chapter II below). This result might be explained by the Heffner hypothesis of sound localization acuity (2004) discussed above.

In addition to our finding that rat auditory cortical cells are level-dependent, we are unaware of any studies investigating the behavioral abilities of rat sound localization to changing sound levels. One possibility is that changes in sound level bias their responses laterally. Rats perform poorly on sound localization tasks (Kavanagh and Kelly 1986) and this could be due to a lack of neural coding mechanisms. Or, perhaps in rodents the integration of sound level and location occurs in other processing centers such as the superior colliculus or parietal cortex. These questions remain open and untested at this time.

Neural Coding Mechanisms Underlying Sound Localization in the Auditory Cortex

After sound information is processed by multiple nuclei in the auditory brainstem and midbrain, it is delivered to the primary auditory cortex from axonal projections leaving the ventral division of the medial geniculate body of the thalamus (MGBv). These thalamic inputs are exclusively excitatory and to date there are no reports of any inhibitory projections entering the cortex from any other brain region. Therefore all inhibition in the cortex is derived from local short range sources with axons limited to only a few millimeters in length (Markram et al. 2004; Thomson and Lamy 2007). When the spiking output of cortical cells matches the excitatory inputs, the tuning responses are said to be "inherited". For example, in Fig. 1A the neuron responds to midline ILDs (near 0 dB) and inhibition is proportional to and lags behind excitation by a few milliseconds (Wehr and Zador 2003). Another possibility in the inheritance strategy is the construction of tuning response by multiple excitatory sources. For example, this has been observed in the visual cortex in orientation tuning. In this case, the role of inhibition is still passive.

In some cases the excitatory inputs received by cortical neurons are more broadly tuned than the spiking output of the cell. For example, in Fig. 1B the neuron is again tuned to midline ILDs (near 0 dB). However, at contralateral ILDs (> 0 dB) the cell receives excitation which by itself would cause the cell to spike. However, strong inhibitory inputs at these ILDs causes the firing rate of the cell to decrease. This is an example of the local processing strategy. The goal of Chapter III in this dissertation was to elucidate which of the these processing strategies is utilized by cortical neurons responding to ILD cues.

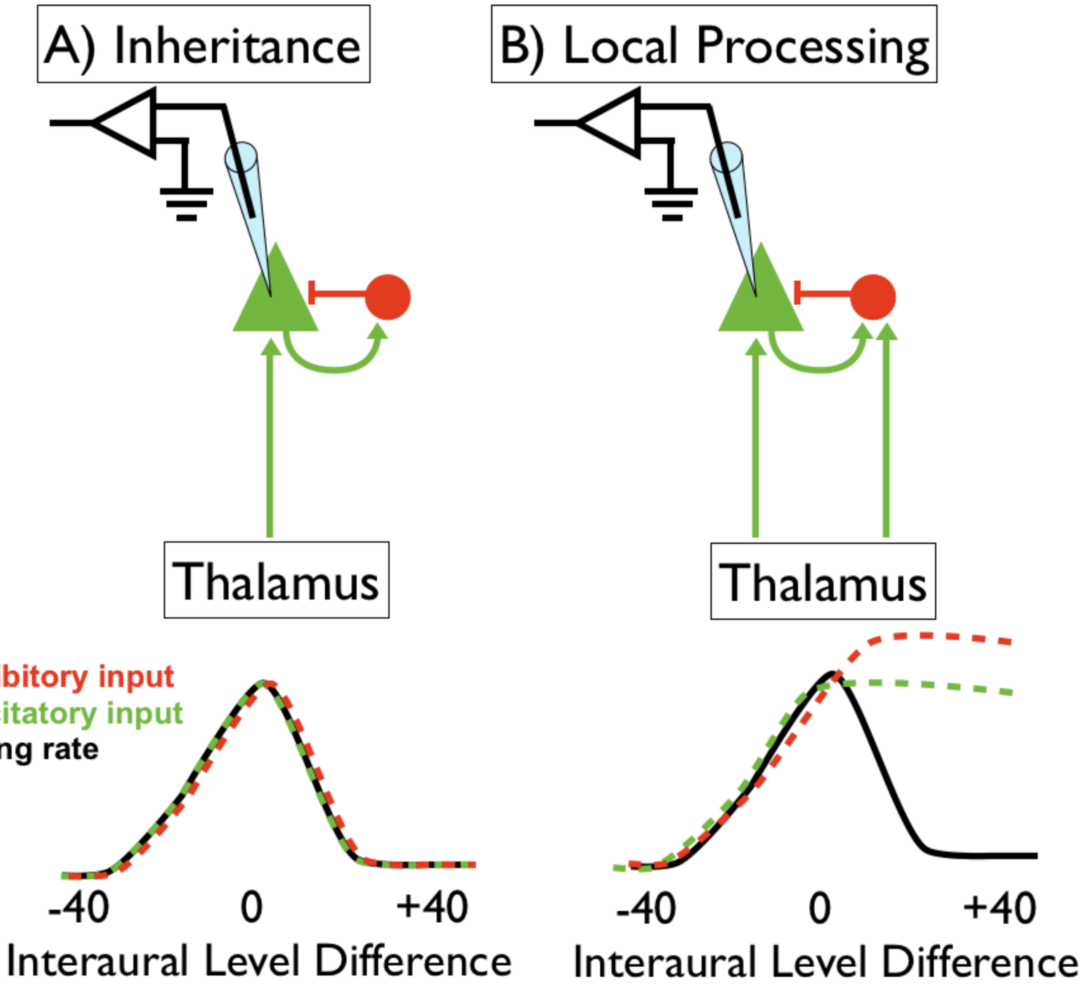

Figure 1. Candidate circuits underlying interaural level difference processing in rat auditory cortex. In the inheritance strategy (A) the firing rate (black) matches that of the excitatory input (green). Here, inhibition is passive (red) and is driven by feed-forward input from the recorded neuron. In the local processing strategy (B) the excitatory inputs are more broadly tuned than the spiking output. In this case the neuron receives excitatory input sufficient to drive spiking output at central ILDs near zero, however an additional thalamic input onto the inhibitory neuron causes suppression of spiking at positive ILDs. These two circuits are simplified implementations to illustrate the conceptual difference between the two strategies; the actual circuits are undoubtedly more complex.

CHAPTER II

NEURONAL INTERAURAL LEVEL DIFFERENCE RESPONSE SHIFTS ARE LEVEL-DEPENDENT IN THE RAT AUDITORY CORTEX

Reproduced with permission from Kyweriga M, Stewart W, Wehr M. Neuronal interaural level difference response shifts are level-dependent in the rat auditory cortex. *J Neurophysiol* 111: 930-938, 2014.

Introduction

Determining the location of unseen predators, prey, and conspecifics is one of the primary functions of the auditory system. Mammals use three cues to localize sounds: interaural time differences (ITD), interaural level differences (ILD), and the head-related transfer function (for review, see Grothe et al. 2010). In animals that hear primarily in the high frequency range, such as the rat (Heffner et al. 1994; Kelly and Masterton 1977), ILD is the primary cue used to determine sound locations on the horizontal azimuth (Kapfer et al. 2002; Wesolek et al. 2010). ILD sensitivity is first computed in the lateral superior olive (LSO: Kavanagh and Kelly 1992; Moore and Caspary 1983). In the LSO, neuronal ILD response shifts are strongly level-dependent (Tsai et al. 2010). This means that early in the processing pathway, changes in firing rate could indicate either changes in sound location or sound level, or both. Yet in psychometric behavioral tasks, ILD sensitivity does not shift with increasing sound levels in macaques (Recanzone and Beckerman 2004) or humans (Altshuler and Comalli 1975; Sabin et al. 2005). How, then, does the brain accomplish sound localization with invariance to total sound level? ILD sensitivity is also observed in higher structures such as the central nucleus of inferior colliculus (ICC: Irvine and Gago 1990; Pollak et al. 1986; Semple and Kitzes 1987) and the auditory cortex (Kelly and Sally 1988; Phillips and Irvine 1983; Zhang et al. 2004). In the LSO, increasing ipsilateral sound levels cause spiking response functions in the LSO to shift towards the ipsilateral ear (Tsai et al. 2010). In the ICC, approximately half of the cells are invariant to increasing sound levels and the remaining cells have leftward, rightward, or mixed shifts with no net shift at the population level (Park et al. 2004). Taken together, these results suggest a gradual transformation from strong level-dependence in the LSO to level-invariance in the perception of sound source location. Consistent with this, a few free-field studies have shown level invariance of azimuth tuning in the auditory cortex of cats (Mickey and Middlebrooks 2003), bats (Razak 2011), and primates (Zhou and Wang 2012), but level dependence of ILD coding in the auditory cortex has not been tested.

Rodents, especially the rat and mouse, are increasingly important model organisms in auditory neuroscience. The rodent auditory system is similar in many ways to those of cats and primates, but different in other ways (for review, see Phillips et al. 2012). For example, ITD and ILD processing differs markedly between rats and other species, such as the cat and primate, which have larger heads (Heffner 2004; Wesolek et al. 2010). It is unknown whether ILD sensitivity in the rat auditory cortex depends on sound level or is level-invariant. It is also unknown whether rats show perceptual invariance to increasing sound levels. Based on previous work in the auditory cortex of cats, bats, and primates, we predicted that ILD response functions in the rat auditory cortex would also be level-invariant. To test this hypothesis, we measured ILD response functions of rat auditory cortical neurons at different sound levels. Surprisingly, we found that ILD responses strongly shifted towards the ipsilateral ear with increasing sound levels in both spiking output and in sub-threshold membrane potential responses. To understand how this transformation is accomplished, we used in vivo whole-cell recordings to measure ILD response functions for synaptic excitation and inhibition. The results suggest that these shifts are not created in the cortex by synaptic processing, and are instead consistent with inheritance from pre-synaptic neurons. We conclude that level invariance of ILD sensitivity is not present in the rat auditory cortex.

Methods

All procedures were in strict accordance with the National Institutes of Health guidelines as approved by the University of Oregon Institutional Animal Care and Use Committee.

Physiology

We recorded from the left auditory cortex of 86 anesthetized (30 mg/kg ketamine, 0.24 mg/kg medetomidine) albino rats (*Rattus norvegicus*, Sprague Dawley), aged 19 - 28 (mean = 23.4, SD = 2.7) days postnatal. We used this age range to improve the yield of in vivo whole-cell recordings (Scholl et al. 2010). Rats older than 14-19 days, like adults, orient correctly toward sounds on the horizontal plane (Kelly et al. 1987). The critical period for hearing in the rats is complete by approximately postnatal day 14 (de Villers-Sidani et al. 2007), although some limited additional maturation of receptive fields and synaptic markers (e.g., NR1, GluR2, and GAD65) occurs until approximately postnatal day 28 (Chang et al. 2005; Lu et al. 2008; Popescu and Polley 2010; Xu et al. 2007; Xu et al. 2010). We tested whether any of our neural ILD measures depended on age within this range (see below for details of these measures and how they were computed). We found no significant effect of age on ILD shifts based on integrated membrane potential ($R^2 = 0.029$, $p = 0.06$), firing rate ($R^2 = 0.003$, $p = 0.62$), inhibitory conductance ($R^2 = 0.004$, $p = 0.65$), or excitatory conductance ($R^2 = 0.003$, $p = 0.71$) indicating that these measures are developmentally stable (and likely mature) during this age range. Nevertheless, it is important to note that our results do not rule out possible changes in cortical ILD processing in adulthood (i.e., >28 days).

At the beginning of each experiment we used tungsten microelectrodes (1-2 MΩ, FHC) to coarsely map the auditory cortex, using multi-unit recordings. We sought to locate sites with robust binaural response properties. Approximately 80% of neurons in this report were located in either the primary auditory cortex (A1) or supra-rhinal auditory field (SRAF; Higgins et al. 2010; Polley et al. 2007), with the remainder from either ventral or posterior auditory fields (VAF or PAF). We identified A1 from the caudal-rostral tonotopic gradient. We also targeted SRAF, which contains a relatively high proportion of cells preferring central ILDs (Higgins et al. 2010). We identified SRAF from the absence of auditory evoked responses along its ventral border.

Single-unit recordings

We obtained single-unit recordings using the loose cell-attached patch method, which provides excellent single-unit isolation. We only included cells in our sample if they had at least one spike following stimulus onset (0 to 125 ms; N = 117 cells) and a minimum of 5 trials per stimulus combination. Subpial depth for these cells ranged from 111 to 1015 μm (mean = 573.8 μm, SD = 205.3), as determined from micromanipulator travel.

Whole-cell recordings

We used standard blind patch-clamp methods to obtain 166 whole-cell recordings. We only included cells in our sample if they had stable pre-stimulus resting membrane potentials (-50 to 0 ms) that were within 5 mV between the beginning and end of the recording. Subpial depth for these cells ranged from 122 to 844 μm (mean = 389.6 μm, SD = 146.3). We did not use voltage-gated channel blockers in the pipette solution, so that we could record both spiking output and synaptic currents from the same cells. The internal solution contained, in mM, K-gluconate 120, $MgCl_2$ 2, $CaCl_2$ 0.05, MgATP 4, NaGTP 0.4, Na_2Phosphocreatine 10, HEPES 10, BAPTA 13, pH 7.28, diluted to 297 mOsm, producing a calculated inhibitory reversal potential of -91.1 mV and an excitatory reversal potential of 3.4 mV. We corrected for a calculated liquid junction potential of 15.0 mV (Barry 1994), based on standard extracellular ionic concentrations (Sykova 1997), body temperature of 37ºC, and dilution of our internal solution concentrations by ~10% (to achieve physiological osmolarity).

In a subset of cells we also obtained voltage-clamp recordings. Holding potentials were stepped (using a 1 s ramp) to a pseudorandom sequence of two values using an Axopatch 200B amplifier. At each potential, after a 1 second equilibration period, ten 10 mV voltage pulses were delivered to monitor series and input resistance, followed by acoustic stimuli. For our sample of neurons recorded with voltage-clamp, input resistance was 55.6 ± 30.2 MΩ, and series resistance was 48.3 ± 4.2 MΩ (median ± interquartile range, N = 73 cells). We measured synaptic currents at two holding potentials (mean = -108.2 mV, SD = 4.7, and mean = +27.5 mV, SD = 19.5; corrected for series resistance and liquid junction potential) and for 5-10 trials (median 10) for each acoustic stimulus. Synaptic conductances, corrected for series resistance, were computed offline assuming an isopotential neuron (for details, see Wehr and Zador 2003). To ensure high-quality voltage-clamp recordings, we discarded cells that failed to show evoked conductances greater than 0.5 nS, and a minimum of 5 trials for each stimulus combination, resulting in a sample of 73 neurons.

In summary, we recorded from 117 cells using the loose cell-attached method and 166 cells using the whole-cell current-clamp method. Our whole-cell data set contained 78 spiking cells recorded in current-clamp mode, which were added to the cell-attached data set to create a total of 195 spiking cells. Our whole-cell data set also contained 73 cells recorded in voltage-clamp mode.

Sound stimuli

All stimuli were generated with custom software in MatLab (Mathworks, Natick, MA) at a sampling rate of 192 kHz using a Lynx-TWO-B sound card and delivered with Etymotics ER-2 earphones in sealed ear configuration. These earphones were suitable for our experiments as the rat audiogram is 7 octaves (0.5-64 kHz; Heffner et al. 1994; Kelly and Masterton 1977) and the ER-2 earphones cover over half of this range (4 octaves: 1-16 kHz). All experiments were performed in a double-walled sound isolation chamber with anechoic surface treatment. We sealed the Etymotics ER-2 earphones along with Knowles omnidirectional electret condenser microphones into each ear.

The sound level inside each ear canal was calibrated with the Knowles microphones, which were in turn calibrated with a Bruel & Kjaer 4939 1/4" microphone prior to each experiment. To characterize binaural response properties we used pseudorandomly interleaved white noise bursts (25 ms duration) presented simultaneously to each ear from 10-50 decibel (dB) sound pressure level, in 10 dB steps (noise was not frozen between left and right or between each level). This produced an array of 25 binaural stimuli, with a range of average binaural levels (ABL; defined as the average of the levels presented to the two ears) from 10 to 50 dB, across a range of ILDs from -40 to +40 dB (corresponding to the maximum physiological range of ILD; Koka et al. 2008). Figure 2B shows this stimulus array with both coordinate systems included; ILD is on the x-axis and ABL is on the y-axis, whereas the levels in the ipsilateral ear and contralateral ear are on the diagonal axes (rotated by 45°). We restricted sound levels to a maximum of 50 dB because we noticed that higher levels produced cross-talk from one ear to the other, presumably due to sound transmission through the head (data not shown). We defined contralateral ILDs as positive. All stimuli had 5 ms onset and offset ramps with 500 ms interstimulus intervals.

For whole-cell recordings, we first recorded membrane potential responses to our stimulus set in current clamp mode. Then we switched to voltage-clamp mode and measured the synaptic currents evoked by the same stimuli. Due to time constraints, we were only able to measure the characteristic frequency in a subset of our recorded cells (N = 47 cells). We presented a monaural tuning curve to the contralateral ear comprised of pure tones, at 5 intensities from 10-50 dB, and at 4 frequencies per octave from 1-16 kHz. As with our binaural stimulus set, all tuning curve stimuli were 25 ms, with 5 ms onset and offset ramps and were presented with 500 ms interstimulus intervals. We determined the CF by finding the frequency eliciting the greatest response at the lowest intensity (for details, see Polley et al. 2007).

Data analysis

To extract spikes, we first high-pass filtered extracellular and intracellular recorded voltages at 300 Hz (Butterworth filter) and used an absolute threshold of 1 - 5 mV (median = 5 mV; mean = 3.7 mV, SD = 1.8). We quantified spiking responses by counting spikes in a 125 ms window beginning at sound stimulus onset in 20 ms bins (Fig. 2, A and D). Baseline firing rate, computed in the 375 ms window ending at sound onset (i.e., the remainder of the inter-stimulus interval), was subtracted from each spiking response (note that baseline firing rate in Fig. 2C,F is zero). We then set negative firing rates to zero.

We quantified membrane potential responses by integrating the trial-averaged membrane potential in the 200 ms window following stimulus onset, wherever the membrane potential was significantly above baseline (z-score with $p < 0.05$; red region in Fig. 3 A&D). Similarly, we quantified synaptic conductance responses by integrating conductances in the 200 ms window following sound onset wherever the conductance was significantly above zero ($p < 0.05$). We set negative conductances to zero.

Interaural level difference response shift calculation

We calculated ILD response shifts for each cell (Park et al. 2004; Tsai et al. 2010). In our binaural stimulus set, for each ipsilateral level, we presented the rat with five contralateral levels from 10 to 50 dB (in 10 dB steps), thereby creating a stimulus array of 5 ILDs for each ipsilateral sound level. Since these response functions could be monotonic or non-monotonic, we employed two different methods to determine the ILD response shift.

The first method focused on responses that increased or decreased monotonically with ILD (i.e., for contralateral-preferring or ipsilateral-preferring cells, respectively). To determine the ILD response shift, we first sought a reliable point on each ILD response function that could be used to measure shifts. For this we chose the half-maximal ILD, which is at the steepest part of the ILD response function and is therefore the most reliable point for measuring shifts. To find the half-maximal ILD, we first measured the maximum of the trial-averaged ILD response function. To ensure these peak responses were significant, for spiking responses we only included ILD response functions where the peak ILD response was >1 S.D. above the baseline firing rate; for membrane potential and conductance responses, we only integrated responses when they were significantly above baseline. We then found the half-maximal response value (halfway between the maximum value and the pre-stimulus baseline). The half-maximal ILD was defined as the interpolated ILD that produced the half-maximal response value, for each ipsilateral stimulus array. These half-maximal values are indicated by circles in Fig. 2C.

We then measured the mean ILD response shift for a cell as the average difference between the half-maximal ILDs for the ILD response functions at each ipsilateral sound level, divided by the change in ipsilateral sound level. For example, in Fig. 2C, the dark blue (7.5 dB) and light blue (-2.5 dB) circles are separated by 10 dB, producing a leftward ILD response shift of -10 dB (-2.5 - 7.5 dB) caused by a 10 dB increase in ipsilateral sound level. This response shift is therefore -10/10 = -1 dB/dB. Altogether, Fig. 2C has four half-maximal ILD shifts of -10 (-2.5 - 7.5 dB), -0.4 (-2.9 - (-2.5) dB), -2.1 (-5 - (-2.9) dB), and -6.7 (-11.7 - (-5) dB) dB, each caused by 10 dB increases in ipsilateral sound levels. This produced four respective response shifts of -1, -0.04, -0.21, and -0.67 dB/dB with a mean response shift of -0.48 dB/dB (SD = 0.44). Thus, on average, for each decibel increase in sound level, the ILD response function of this cell shifted 0.48 dB towards the ipsilateral ear. Note that if we instead calculated the total ILD response shift: [e.g., (-11.7 - 7.5) / (50-10) = -0.48] we obtain the same result, and our overall results remain unchanged (data not shown), as others have reported (Park et al. 2004; Tsai et al.

2010). Negative response shifts indicate leftward shifts towards the ipsilateral ear, and positive response shifts indicate rightward shifts towards the contralateral ear. Response shifts of zero indicate invariance with respect to increasing sound levels.

The second method for calculating response shifts focused on responses that were non-monotonic as a function of ILD (i.e., for binaural-preferring cells), for which we slightly modified the first method. For each ipsilateral stimulus array, we measured the half-maximal response values falling on either side of the peak response of firing rate (Fig. 2F), integrated membrane potential (Fig. 3F), or integrated conductances (data not shown). We then took the average of these two half-maximal ILD values, resulting in a single value approximately corresponding to the peak of the ILD response function (Fig. 2F and 3F, circles). We then used this point to compute the ILD response shifts as described above for contralateral and ipsilateral cells.

For both methods, in order to calculate the response shift, at least two half-maximal ILDs in a single binaural category were required, otherwise the cell was discarded. For example, some response functions had multiple half-maximal values, or were unresponsive. Thus, for these response functions it was not possible to determine half-maximal ILDs and these response functions were omitted from our analysis (e.g., Fig. 3F, red trace). We also tested a more rigorous criterion requiring each cell to produce at least 3 half-maximal ILDs. While this reduced our sample size by ~ 50% for spiking, membrane potential, and conductance measures, our results remained unchanged (data not shown). We did not compute response shifts between half-maximal values computed by two different methods within a cell. For example, no shift was calculated for ILD response functions that were monotonic at one ipsilateral sound level and non-monotonic at another.

To test the significance of the response shifts computed for each cell, we used bootstrap resampling to produce a distribution of 100 resampled response shifts for spiking, membrane potential, and conductance data. We then tested whether these distributions were significantly less than zero using the one-sample t-test for each cell.

Results

Spiking interaural level difference responses in the rat auditory cortex shift towards the ipsilateral ear with increasing ipsilateral sound level

We obtained spiking output from 195 cells using both the loose cell-attached method (117 cells) and the whole-cell method (78 cells in current-clamp mode). Representative examples of two cells are shown in Fig. 2, A-F. Figure 2 A-C shows an example of a contralateral-preferring cell, often referred to in the literature as binaurally inhibited (EI or EO/I; Razak and Fuzessery 2010; Zhang et al. 2004). This cell type shows robust firing to contralateral (+10 to +40 ILDs) and some central (-10 to +10 ILDs) sounds, but did not respond to ipsilateral stimuli (-40 to -10 ILDs; Fig. 2, A and B). Figure 2C shows that the ILD response curves shifted -19.2 dB (-11.7 - 7.5 dB; Fig. 2C, red and dark blue circles, respectively; see methods) when ipsilateral levels were increased from 10 to 50 dB. This corresponded to a -0.48 dB/dB average response shift for this cell (SD = 0.44). In other words, for each 1 dB increase in ipsilateral level, the ILD response functions shifted 0.48 dB towards the ipsilateral ear. This response shift was highly significant ($p = 1.41e\text{-}43$, as determined by bootstrap resampling, mean shift: -0.51, SD = 0.21, see methods).

Figure 2 D-F is an example of a binaural-preferring cell, also referred to in the literature as binaurally facilitated (PB or EE/F; Zhang et al. 2004), predominantly binaural (PB; Razak and Fuzessery 2010), or peaked (Razak 2011). This cell type shows robust firing to central sounds (-10 to +10 ILDs), but weak or no responses to either contralateral (+10 to +40 ILDs) or ipsilateral sounds (-40 to -10 ILDs; Fig. 2, D and E). Figure 2F shows that the ILD response curves shifted -30.3 dB (-10.6 - 19.7 dB; Fig. 2F, red and dark blue circles, respectively), when ipsilateral levels increased from 10 to 50 dB. This corresponded to a -0.76 dB/dB response shift for this cell (SD = 0.33). This response shift was highly significant ($p = 6.72e\text{-}122$, mean bootstrapped shift: -0.77, SD = 0.05).

In our sample of spiking cells, 74/195 had robust ILD response functions and met our inclusion criteria (see methods). Of these cells, 66/74 had negative response shifts, with a mean shift of -0.69 dB/dB (SD = 0.54). This population average shift was significantly negative ($p = 3.8e\text{-}17$, one-sample t-test), and each of the 66/74 negative response shifts were significantly negative (at the $p<0.05$ level, as tested by bootstrap resampling). Previous studies have used an arbitrary criterion of -0.4 dB/dB to classify response shifts as significant (Park et al. 2004; Tsai et al. 2010); by this measure, 55/74 of our cells (74.3%) were significantly below this criterion ($p = 1.6e\text{-}5$, one-sample t-test). There were no significant differences between the response shifts in each binaural preference category (independent samples t-test, all p-values > 0.25). We conclude that

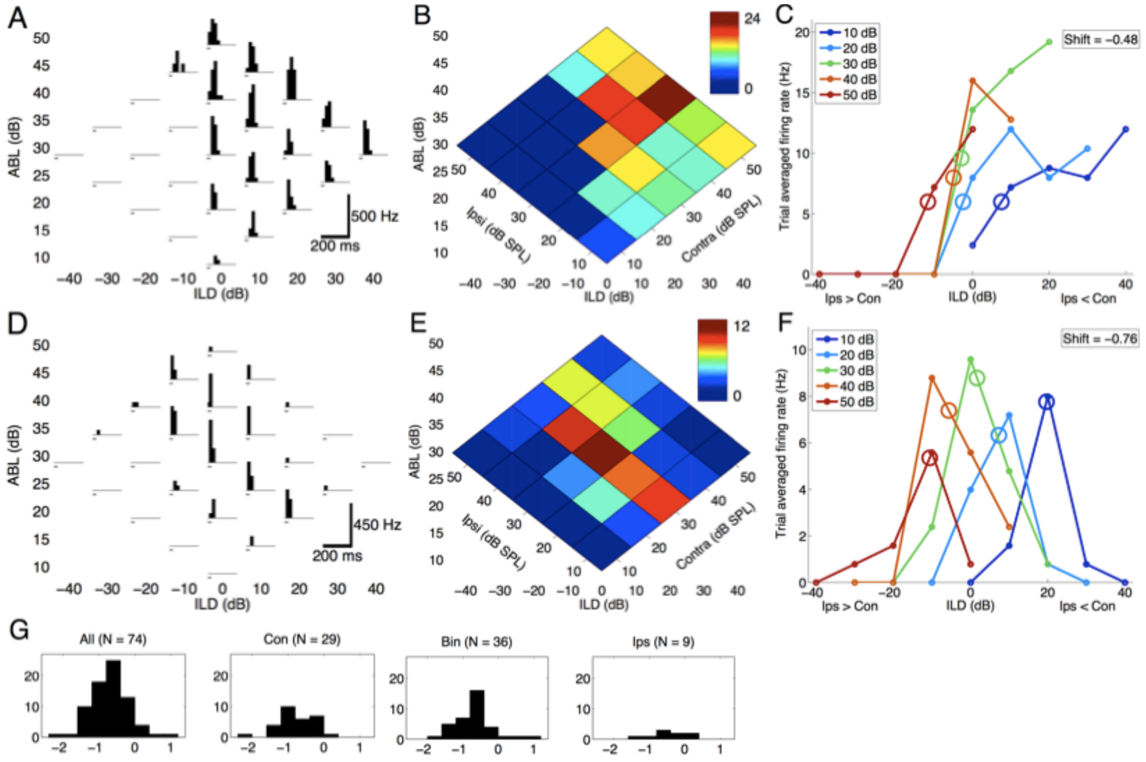

Figure 2. Spiking interaural level difference responses in the rat auditory cortex shift toward the ipsilateral ear (negative shifts) with increasing ipsilateral sound level. *A–F:* 2 representative examples showing negative ILD response shifts in both contralateral-preferring (A–C; *cell 120810-MK-3-2)* and binaural-preferring (D–F; *cell 091410-WS-2-1)* cells. *A* and *D:* spiking responses to the binaural stimulus array. Each histogram shows the firing rate in 20-ms bins (accumulated from 10 trials). White noise bursts (25-ms duration) are indicated in gray. *B* and *E:* trial-averaged normalized firing rate heat maps of the same data shown in *A* and *D.* Dark red indicates maximum firing rate, and dark blue indicates minimum firing rate. Each binaural stimulus can be represented either as an ILD-average binaural level (ABL) combination (x- and *y-axes)* or as a contralateral and ipsilateral sound level (diagonal axes). For example, the green response at ILD 20, ABL 20 corresponds to Contra 30, Ipsi 10. *C* and *F:* firing rate ILD response curves. Ipsilateral level is held constant for each curve (see *inset* for color code) as a function of ILD. In other words, each line is a diagonal slice through *B,* parallel to the Contra axis. *C:* contralateral-preferring cell with a mean ILD response shift of -0.48 dB/dB (SD = 0.44; see METHODS for detailed description). Circles denote half-maximal ILD values. Negative ILDs correspond to greater ipsilateral level (Ips > Con); positive ILDs correspond to greater contralateral level (Ips < Con). *F:* binaural-preferring cell with a mean ILD response shift of -0.76 dB/dB (SD = 0.33). Circles denote the average of left and right half-maximal ILD values; thus the circles are found near the maxima. *G:* population histograms showing that the majority of cells (89.2%) have negative response shifts (top *left,* 66/74 cells), regardless of binaural preference categorization (Con, contralateral preferring; Bin, binaural preferring; Ips, ipsilateral preferring).

the spiking responses of auditory cortical neurons overwhelmingly show negative ILD response shifts with increasing sound level.

In a subset of our spiking data set (47/195 cells), we measured the characteristic frequency (CF) of the cell by presenting a frequency-intensity tuning curve to the contralateral ear. We then presented the rat with the binaural stimulus array at the cell's CF (47 cells: 40 cell-attached, 7 whole-cell). From this sample, 16/47 cells had robust ILD responses and met our inclusion criteria. Consistent with our much larger white noise sample, 15/16 cells had negative response shifts, with a mean shift of -0.85 dB/dB (SD = 0.6). This population average shift was significantly negative (p = 4.59e-5, one-sample t-test) and each of the 15/16 negative response shifts were significantly negative (at the $p<0.05$ level, as tested by bootstrap resampling). We found that 75% of our cells had response shifts that were significantly lower than the arbitrary criterion of -0.4 dB/dB (12/16 cells, p = 8.9e-3, one-sample t-test). This result indicates that leftward ILD response shifts are not specific to white noise stimuli, and are a more general property of the rat auditory cortex.

Membrane potential interaural level difference responses in the rat auditory cortex shift towards the ipsilateral ear with increasing ipsilateral sound level

About half of the neurons in our whole-cell sample (88/166) did not fire any spikes in response to our binaural stimuli. This is consistent with previous reports of sparse spiking responses in the auditory cortex (Chadderton et al. 2009; DeWeese et al. 2003; Hromadka et al. 2008). In fact, this proportion is probably an underestimate of the prevalence of non-spiking cells, since we often aborted recordings from non-spiking cells. However, we wondered whether ILD response shifts also occurred for sub-threshold membrane potential responses. Representative examples of two non-spiking cells are shown in Fig. 3, A-F. Figure 3, A-C is an example of a non-spiking contralateral-preferring cell. This cell showed membrane potential depolarizations to contralateral (+10 to +40 ILDs) and some central (-10 to +10 ILDs) sounds, but had only very weak responses to ipsilateral stimuli (-40 to -10 ILDs; Fig. 3, A and B). To calculate the ILD response functions for each ipsilateral level, we integrated the average membrane potential depolarization wherever it was significantly above baseline (z-score $p < 0.05$, red regions in Fig. 3A&D) for each stimulus combination. Increasing ipsilateral sound levels from 10 to 50 dB caused the ILD response curve to shift -31.7 dB (-7.5 - 24.2 dB; Fig. 3C, red and dark blue circles, respectively), with an average response shift -0.79 dB/dB (SD = 0.68). This response shift was highly significant (p = 1.7e-117, mean bootstrapped shift: -0.80, SD = 0.06).

Figure 3 D-F shows an example of a non-spiking binaural-preferring cell. This cell responded to central (-10 to +10 ILDs) sounds, but had weak or no responses to either contralateral (+10 to +40 ILDs) or ipsilateral sounds (-40 to -10 ILDs; Fig. 3, D and E). Figure 3F shows that increasing ipsilateral levels from 10 to 40 dB caused the ILD response curves to shift -19 dB (-4.5 - 14.5; Fig. 3F, orange and dark blue circles, respectively). This corresponded to a mean response shift of -0.63 dB/dB (SD = 0.33). This response shift was highly significant (p = 1.41e-43, as determined by bootstrap resampling, mean shift: -0.75, SD = 0.32, see methods)

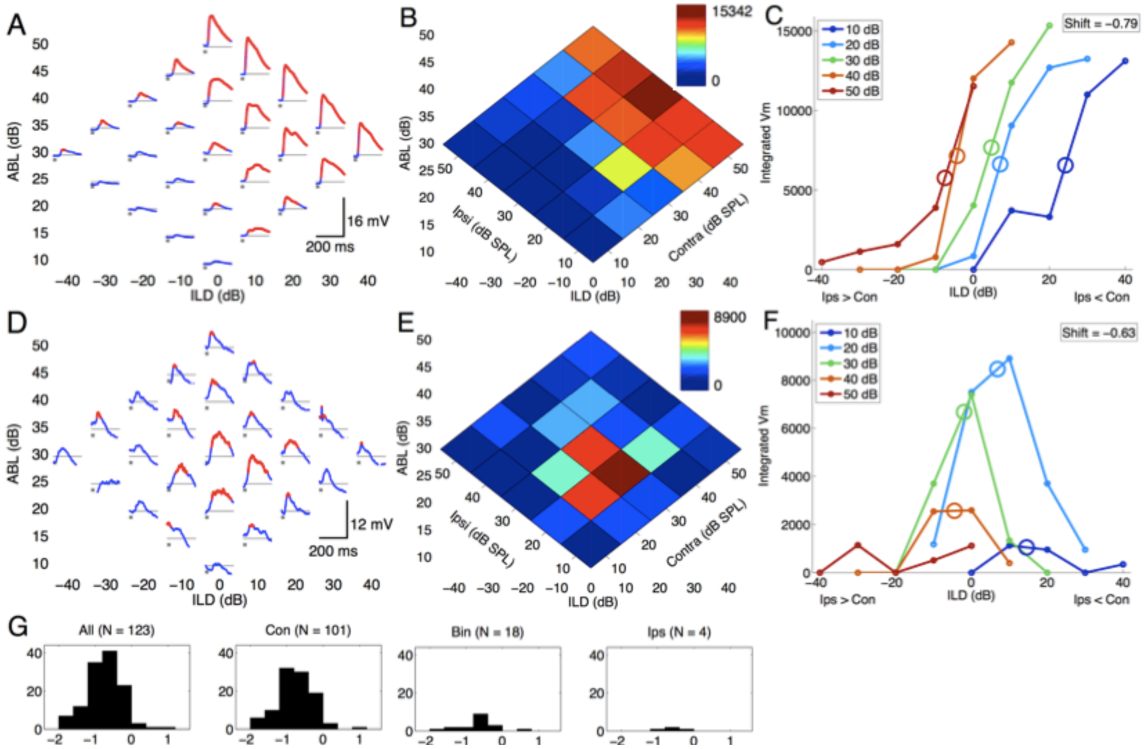

Figure 3. Membrane potential (Vm) interaural level difference responses in the rat auditory cortex shift toward the ipsilateral ear with increasing ipsilateral sound level. *A–F:* 2 representative examples showing negative ILD response shifts in both contralateral-preferring (A–C; *cell 010511-MK-3-8)* and binaural-preferring (D–F; *cell 080910-MK-2-2)* nonspiking cells. *A* and *D:* membrane potential responses to the binaural stimulus array. Each subplot shows the membrane potential (A: mean of 20 trials; *D:* mean of 10 trials). White noise bursts (25 ms duration) are indicated in gray. Resting membrane potential (V_{rest}) is indicated by horizontal thin gray line (A: V_{rest} = -78.8 mV; *D:* V_{rest} = -60.2 mV). Red regions are significantly above baseline and were included in the integrated membrane potential responses in *B* and *C. B* and *E:* normalized integrated membrane potential heat maps of the same data shown in *A* and *D.* Dark red indicates maximum depolarization, and dark blue indicates minimum depolarization. *C* and *F:* integrated membrane potential ILD response curves. Ipsilateral level held constant for each curve as a function of ILD. *C:* contralateral-preferring cell with a mean ILD response shift of -0.79 dB/dB (SD = 0.68).

F: binaural-preferring cell with a mean ILD response shift of -0.63 dB/dB (SD = 0.33).

G: population histograms showing that the majority of cells (95.9%) have negative membrane potential response shifts (top *left,* 118/123 cells), regardless of binaural preference categorization.

In our whole-cell sample, 123/166 had robust ILD responses and met our inclusion criteria. Of these cells, we found that 118/123 had negative response shifts, with a mean shift of -0.74 dB/dB (SD = 0.48), which was significantly negative at the population level (p = 1.06e-33, one-sample t-test). Each of the 118/123 negative response shifts were significantly negative (at the $p<0.05$ level, as tested by bootstrap resampling). We found no significant differences between the response shifts in each binaural preference category (independent samples t-test, all p-values > 0.54). Again, using an arbitrary cut-off of -0.4 dB/dB, we found that 77.2% of our cells had response shifts that were significantly lower than this cut-off value (95/123 cells, p = 3.49e-12, one-sample t-test). We conclude that, like spiking responses, sub-threshold membrane potential responses also show negative ILD response shifts with increasing sound level.

Both excitatory and inhibitory responses in the rat auditory cortex shift towards the ipsilateral ear with increasing ipsilateral sound level

Within our sample of whole-cell recordings we were also able to obtain voltage-clamp recordings in 73/166 cells. Only cells that responded with peak responses of at least 0.5 nS and had at least 5 trials per stimulus combination were included in this count. Figure 4, A-C is a representative example of excitatory and inhibitory inputs in a contralateral-preferring cell. This cell showed excitatory conductances to contralateral (+10 to +40 ILDs) and central (-10 to +10 ILDs) sounds, but not to ipsilateral stimuli (-40 to -10 ILDs; Fig. 4A, green shows excitatory conductance (GE)). While inhibitory conductances were observed at all ILDs (Fig. 4A, red shows inhibitory conductance

(GI)), note the reduction in inhibitory conductance magnitude when comparing ipsilateral ILDs to central and contralateral ILDs. To calculate the ILD response functions for each ipsilateral level, we separately integrated the excitatory (Fig. 4B) and inhibitory conductances (Fig. 4C) at all sample points when the synaptic conductance was significantly above zero ($p < 0.05$). Increasing ipsilateral sound levels from 10 to 50 dB, caused the integrated excitatory conductances to shift -26.8 dB (-12.7 - 14.1; Fig. 4B, red and dark blue circles, respectively), with an average response shift -0.67 dB/dB (SD = 0.61). This response shift was highly significant (p = 2.0e-153, mean bootstrapped shift: -0.67, SD = 0.02). Increasing ipsilateral sound levels from 10 to 50 dB, caused the integrated inhibitory conductances to shift -29.5 dB (-18.6 - 10.9; Fig. 4C, orange and dark blue circles, respectively), with an average response shift of -0.98 dB/dB (SD = 0.4). This response shift was highly significant (p = 3.4e-98, mean bootstrapped shift: -1.05, SD = 0.11).

In our voltage-clamp whole-cell sample, 52/73 cells had robust excitatory conductances and met our inclusion criteria (Fig. 4D). Of these cells we found that 46/52 had negative response shifts, with a mean shift of -0.65 dB/dB (SD = 0.58), which was significantly negative at the population level (p = 1.1e-10, one-sample t-test). Each of the 46/52 negative response shifts were significantly negative (at the $p<0.05$ level, as tested by bootstrap resampling). We found no significant differences between the response shifts in the CP and BP categories (independent samples t-test, p = 0.24), Again, using an arbitrary cut-off of -0.4 dB/dB, we found that 82.7% of our cells had response shifts that were significantly lower than this cut-off value (43/52 cells, p = 0.003, one-sample t-test).

Additionally, in our voltage-clamp data set, 55/73 cells had robust inhibitory conductances and met our inclusion criteria (Fig. 4E). Of these cells we found that 52/55 had negative response shifts, with a mean shift of -0.75 dB/dB (SD = 0.53), which was significantly negative at the population level (p = 1.3e-14, one-sample t-test). Each of the 52/55 negative response shifts were significantly negative (at the p<0.05 level, as tested by bootstrap resampling). We found no significant differences between the response shifts in each binaural preference category (independent samples t-test, all p-values > 0.18).

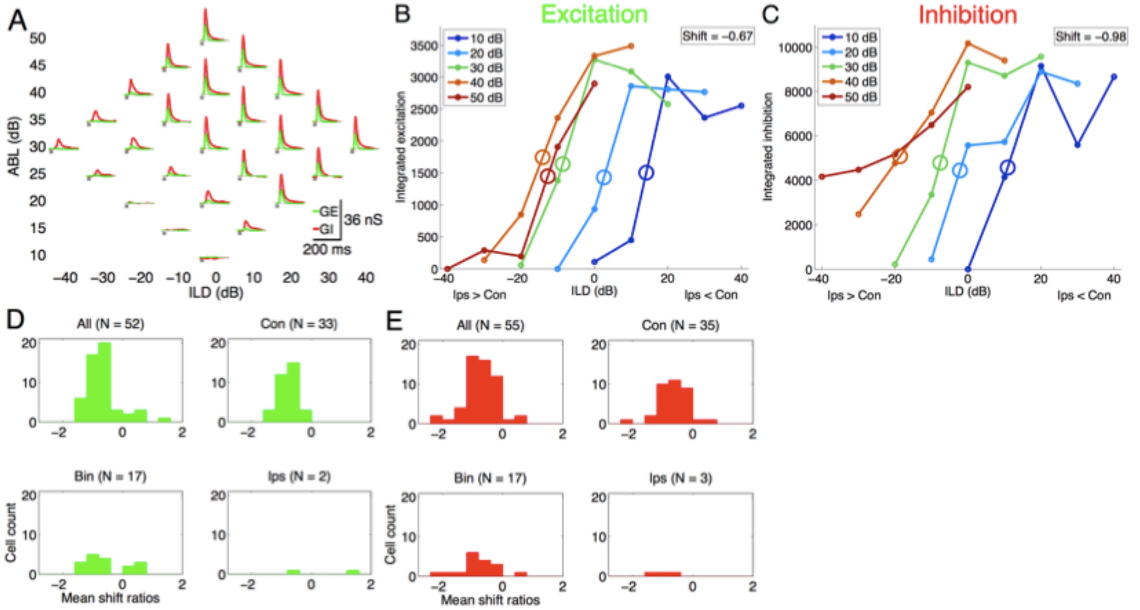

Figure 4. Synaptic conductance interaural level difference responses in the rat auditory cortex shift toward the ipsilateral ear with increasing ipsilateral sound level. *A:* representative example showing negative ILD response shifts to both excitatory (GE, green) and inhibitory (GI, red) conductance responses to the binaural stimulus array (cell *072810-MK-3-1).* White noise bursts (25-ms duration) are indicated in gray. *B* and *C:* integrated synaptic conductance ILD curves (B: excitatory; *C:* inhibitory). Ipsilateral level held constant for each curve as a function of ILD. This cell was contralateral preferring and had a mean ILD response shift of -0.67 dB/dB for excitation (B; SD = 0.61) and -0.98 dB/dB for inhibition (C; SD = 0.4). *D* and *E:* population histograms showing that the majority of cells (88.5%) had negative GE response shifts (D, *top left,* 46/52 cells) and 94.5% of cells had negative GI response shifts (E, *top left,* 52/55 cells), regardless of binaural preference categorization.

Again, using the arbitrary cut-off of -0.4 dB/dB, we found that 72.7% of our cells had response shifts that were significantly lower than this cut-off value (40/55 cells, p = 1.0e-5, one-sample t-test).

Finally, we asked whether excitatory or inhibitory synaptic conductances were predictive of firing rate and membrane potential response shifts. Using linear regression we found that excitatory response shifts were not predictive of firing rate ($R^2 = 0.64$, slope = 1.5, p = 0.4, 3 cells), but did predict membrane potential response shifts ($R^2 = 0.22$, slope = 0.56, p = 0.013, 27 cells). Inhibitory response shifts did not predict firing rate ($R^2 = 0.01$, slope = 0.34, p = 0.91, 4 cells) or membrane potential response shifts ($R^2 = 0.001$, slope = -0.01, p = 0.97, 26 cells). Additionally, at the population level the mean excitatory and inhibitory ILD response shifts were the same (p = 0.588, independent samples t-test) but were uncorrelated with each other (Pearson's rho = 0.27, p = 0.25, 20 cells).

Discussion

Here we report that ILD sensitivity in rat auditory cortical neurons is strongly dependent upon increasing sound levels. We found that as overall sound levels increased, ILD response functions showed significant shifts towards the ipsilateral ear in spiking, membrane potential, and excitatory and inhibitory conductance responses. These shifts occurred regardless of whether the recorded cell responded preferentially to contralateral, ipsilateral or binaural sounds.

How does the brain accomplish sound localization with invariance to total sound level? In the LSO, neuronal ILD response shifts are strongly level-dependent (Tsai et al. 2010). This means that early in the processing pathway, changes in firing rate could indicate either changes in sound location or sound level, or both. Tsai and colleagues (2010) suggested that the ICC corrects this ambiguity by comparing the information from the right and left LSOs via a subtraction model which ultimately leads to sound localization performance that is level-independent, as is seen at the perceptual level (Sabin et al. 2005). One possible scenario is that level dependence decreases gradually with each subsequent processing center, from the LSO, to ICC, auditory cortex and ultimately perception. We reasoned that because sound localization performance is level-invariant, there should be a processing center that encodes ILD in a level-invariant way. Stecker and colleagues hypothesized that the switch from level-dependent to level-independent tuning occurs in a higher cortical area beyond the auditory cortex (2005). Our results support this hypothesis, because we still observed ILD response shifts at the level of the auditory cortex, suggesting that ILD processing is not complete at this point. Another possibility is that although the perception of sound location is level-independent, there need not be an explicit cortical representation of space that is also level-independent. If this were the case, level-dependency may be removed when this information is transformed into motor output, for example in the superior colliculus (Salminen et al. 2012). Yet another possibility is that rats, unlike humans, show level-dependence even at the level of behavioral output. This possibility remains to be tested. It is also possible that cortical ILD processing could change with further maturation, experience-dependent plasticity, or other forms of cortical plasticity.

Although we focused here on ILD processing within the rat auditory cortex, whether and how ILD responses are processed beyond the auditory cortex remains poorly understood. Our results indicate that auditory cortical neurons have level-dependent ILD tuning, but whether or how rats end up with level-invariant perception of sound location remains mysterious. To further understand the implications of cortical ILD response shifts, additional studies investigating this property within the ICC, thalamus, and areas beyond the auditory cortex are required. It is also critical to determine whether perceptual sound localization in rats is level invariant or not. Studies such as these will provide further clarification as to where changes in ILD response shifts occur within the auditory processing pathway, how ILD responses are transformed at each processing level, and ultimately how these transformations define our perception of sound.

Comparison to other studies

Recordings in the LSO of the cat (Tsai et al. 2010) and free-tailed bat (Park et al. 2004) show ILD response curves that shift towards the ipsilateral (excitatory) ear. We found that auditory cortical neurons also showed a shift towards the ipsilateral ear. However, it is important to note that cells in the LSO are almost exclusively driven by the sounds presented to the ipsilateral ear. In the ICC and the auditory cortex, by contrast, most cells are driven by sounds presented to the contralateral ear (due to decussation, in which fibers cross the midline), although many cells are also driven by binaural sounds, especially in SRAF, and in rare cases by ipsilateral sounds. Thus, although neurons in the rat auditory cortex and the cat LSO both show ipsilateral shifts, these shifts are in opposite functional directions (i.e., towards the typically inhibitory and excitatory ears, respectively). In the free-tailed bat, approximately half of the cells in the ICC are invariant to increasing sound levels. The remaining cells have leftward, rightward, or mixed shifts with no net shift at the population level (Park et al. 2004). Park and colleagues therefore suggested that the ICC might be the origin of ILD invariance observed in human sound localization performance.

Two studies have reported level invariance in the auditory cortex. First, in the pentobarbital-anesthetized pallid bat, increasing sound levels produced a diversity of free-field azimuth responses, with about half of the cells showing invariance (Razak 2011). Interestingly, the other half of their cells were level-dependent, but shifted towards the contralateral ear, in the opposite direction from what we observed in the rat. In the second study, in the awake marmoset, free field sounds from a variety of azimuths and elevations elicited response profiles that were invariant with increasing sound levels (Zhou and Wang 2012). Why do our results in the rat auditory cortex differ from those in the pallid bat and marmoset? One possibility is that level-dependence could differ between ILD and free-field stimuli. The invariance observed in these three free-field studies could be the result of integration of ILD cues with ITD and head-related transfer function cues from the cortex or other auditory processing areas, such as the ICC. In other words, it is possible that ILD cues alone could have shown ILD response shifts in these species, but for free-field stimuli the other two binaural cues might have somehow corrected for the shift. This could be tested by directly comparing ILD to free-field responses in the same neurons, for example with the methods used by Razak (2011) or Campbell et al. (2006). A related possibility is that ITD cues help produce level-invariance of ILD sensitivity, perhaps during development, but that this process is absent in species such as rats that do not use ITD cues for sound localization (Wesolek et al. 2010). In this context it would be interesting to test whether ILD sensitivity is also level-dependent in other species that do not use ITD cues, such as mice. It is also intriguing that rats, unlike the species mentioned above, do not suffer deficits in sound localization following lesions to auditory cortex (Kelly 1980; Kelly and Glazier 1978; Kelly and Kavanagh 1986). Sound localization in rats therefore appears to differ in multiple ways from other species.

Another possible explanation for these species differences is based on the hypothesis that sound localization performance is related to the width of visual acuity, which was proposed by Heffner (2004; also see Phillips et al. 2012). Heffner surveyed all known sound localization studies in mammals and found a strong correlation between sound localization acuity and the width of the field of best vision (her Fig. 10). This makes sense, because high-acuity sound localization is important to accurately orient the fovea for animals that have them, like humans, but is less important for animals such as rats that have a broad field of best vision instead of a fovea. Thus, the sound localization errors due to level-dependence would be very costly for cats, bats, and marmosets, which all have narrow visual fields, and therefore would likely provide strong evolutionary pressure towards level-invariance of sound localization. Because of their broad field of best vision, sound localization errors are much less costly for rats, and they may be able to tolerate the errors due to level-dependence. This account predicts that perceptual sound localization performance should be level-dependent in rat, which remains to be tested.

Another possible reason for the difference between our findings and other work in the auditory cortex could arise from anesthesia. However, this seems unlikely since studies in both the awake bat (Park et al. 2004) and ketamine-anesthetized cat (Tsai et al. 2010) show strong evidence of ILD level dependence in the LSO. Additionally, invariance was observed in the awake cat (Mickey and Middlebrooks 2003) and marmoset (Zhou and Wang 2012) as well as in the pentobarbital-anesthetized pallid bat (Razak 2011). Thus, anesthesia seems unlikely to be the reason for the differences between our study and others.

In the auditory cortex, a large proportion of cells are contralateral-preferring, especially in A1 (Chadderton et al. 2009; Imig and Adrian 1977; Kelly and Sally 1988; Phillips and Irvine 1983; Zhang et al. 2004; but see Campbell et al. 2006). However, a higher proportion of cells in the SRAF of auditory cortex are binaural-preferring (Higgins et al. 2010). We wondered whether all cells, and not just contralateral-preferring cells, in the auditory cortex were level-invariant to ILD stimuli. We therefore did not restrict our recordings to A1. Based on our coarse mapping of the auditory cortex using extracellular recordings, approximately 80% of our cells were located in either A1 or SRAF, with the remaining cells located in either VAF or PAF. To our surprise, nearly all of the neurons in our sample had significant ILD shifts towards the ipsilateral ear, throughout these cortical regions. When we subdivided our recordings into specific auditory fields we found no significant differences between the ILD response shifts in these fields.

Cortical inhibition does not appear to shape interaural level difference response shifts

The negative ILD response shifts we observed in the rat auditory cortex did not appear to be shaped by local cortical inhibition. If synaptic processing within the rat auditory cortex had a role in this computation, then we would have expected to find inhibitory conductance ILD response shifts that were more positive than the excitatory ILD response shifts. In that case, active inhibitory shaping would have caused spiking and membrane potential ILD response functions to have more negative shifts than those we observed in the excitatory conductance ILD response shifts. Instead, we observed highly significant negative response shifts in all response types, with no significant differences between spiking, membrane potential, and conductances at the population level. We found that excitatory ILD response shifts significantly predicted membrane potential ILD shifts. However, excitatory and inhibitory conductance response shifts were uncorrelated, and inhibitory response shifts did not predict membrane potential response shifts. Thus, our results are consistent with inheritance from pre-synaptic inputs, since the spiking and membrane potential ILD response shifts matched those of excitatory synaptic inputs. Why, then, are the response shifts of inhibitory inputs uncorrelated with excitation? One possible explanation is that inhibition is involved with a different form of ILD processing, such as the shaping of binaural preferences of cortical cells (Razak and

Fuzessery 2010). With our whole-cell approach, we should be able to test for this possibility.

Bridge

In the work above I suggested that the shaping of cortical responses to ILD cues could explain why inhibition was uncorrelated with excitation. To follow up on this possibility, in Chapter III of this dissertation I investigated the excitatory and inhibitory synaptic interactions in the shaping of binaural preferences in rat auditory cortex. In the present chapter, I focused exclusively on the binaural responses to ILD cues and classified cells accordingly. We did this to directly compare our data with those of previous studies, especially the experiments performed in the LSO by Tsai and colleagues ***(2010)***. In the next chapter, we moved away from our previous classification scheme to focus on common classification of ILD responses in auditory cortex. This scheme classifies cells based on their responses to monaural stimuli and uses a two-letter code. A cell responding significantly to monaural sounds that ear is designated as “E”, otherwise as “O”, with the contralateral ear listed first. For example, a cell responding to contralateral, but not ipsilateral monaural sounds is classified as “EO”. Thus, there are 3 monaural classes, EO for contralateral, OE of ipsilateral, and EE for cells responding to both. A fourth class is unresponsive to monaural sounds but responds predominantly to binaural sounds and is denoted as “PB”. While this classification scheme differs from that reported above, it resulted in similar counts for spiking cells. Our sample of cells reported in Chapter II above was comprised of EO: 39%, OE: 12%, and PB: 49% compared to Chapter III below, which was comprised of EO: 43%, OE: 15%, EE: 6%, and PB: 36%.

In order to investigate the contribution of synaptic inputs to the spiking output of cortical cells in response to the ILD cue, we focused our analyses on cells with both spiking responses and high quality voltage-clamp recordings. This reduced our sample size to 28 cells (15 EO cells and 13 PB cells). Due to the difficulty in obtaining recordings with both spiking and synaptic inputs we were unable to collect data from OE and EE cells. Our findings were that spiking responses of EO cells were not shaped by synaptic inhibition, but rather appear to use an inheritance strategy, where the spiking output matched that of the excitatory input. In marked contrast, the PB cells were actively shaped by cortical inhibition suggesting the utilization of the local processing strategy. The excitatory inputs to PB cells were much broader than the spiking output. The restricted spiking was due to strong inhibition to contralateral ILDs which was only weakly correlated with excitation. This appears to be the reason why excitation and inhibition were uncorrelated in the analyses above.

CHAPTER III

SYNAPTIC MECHANISMS UNDERLYING INTERAURAL LEVEL DIFFERENCE SELECTIVITY IN RAT AUDITORY CORTEX

The work described in this chapter was carried out by myself, Whitney Stewart, and Carolyn Cahill. I was the sole contributor of the data analysis and writing. All experiments, data analysis, and writing was supervised by Michael Wehr, PhD. This chapter is currently under review for publication in the *Journal of Neurophysiology*.

Introduction

In sensory cortex, synaptic interactions can transform neuronal response properties, so that the tuning of the spiking output differs from that of the excitatory input. In this case, synaptic inhibition actively shapes the spiking output, and shows different stimulus sensitivity than that of excitation. However, for many sensory features, the tuning of spiking responses is essentially the same as that of both the excitatory and the inhibitory input. We refer to this as “co-tuning,” in which the ratio of excitation and inhibition is proportional across the entire range of stimuli. In this case inhibition does not have an active role in tuning; rather, the tuning of the neuron is inherited (or in some cases constructed) from the tuning of excitatory presynaptic neurons. Since the axonal projections from inhibitory interneurons are confined to local regions of the cortex (Markram et al. 2004; Thomson and Lamy 2007), an active role for inhibition indicates local synaptic processing. Distinguishing between these inheritance and local processing strategies requires the measurement of both the spiking responses and synaptic conductances within the same neurons. Using this approach in auditory cortex, recent work has shown that frequency tuning is largely inherited (Wehr and Zador 2003), whereas intensity tuning (Tan et al. 2007; Wu et al. 2006) and frequency-modulated sweep selectivity (Zhang et al. 2003) are both partly locally processed. However, little is known about whether or how cortical circuitry contributes to sound localization, a highly conserved auditory function that allows for the detection of unseen threats, prey, or conspecifics. Interaural Level Differences (ILDs) are key binaural sound localization cues for which many auditory cortical neurons are highly selective. The cortical processing strategies for ILD remain largely unknown.

Binaural interactions have been extensively studied with extracellular recordings in the auditory cortex of many different species, such as the rat (Higgins et al. 2010; Kelly and Sally 1988), cat (Imig and Adrian 1977; Kitzes 2008; Phillips and Irvine 1983; Zhang et al. 2004), ferret (Campbell et al. 2006), pallid bat (Razak and Fuzessery 2010), and guinea pig (Rutkowski et al. 2000). However, unlike the visual system, in which binocularity first arises in the cortex, the same binaural selectivities seen in auditory cortex are also seen in the midbrain (Fuzessery et al. 1990; Grothe et al. 2010; Irvine and Gago 1990; Park and Pollak 1993). Whether cortical neurons inherit their ILD selectivity from subcortical neurons, or whether cortical circuitry has an active role in binaural computations, has remained mostly untested. Recent evidence from an intracellular study in cats (Ojima and Murakami 2002), and an extracellular study using a $GABA_A$ antagonist in the pallid bat, suggest that the auditory cortex might actively process ILD cues (Razak and Fuzessery 2010). We therefore sought to directly examine the processing strategy of auditory cortical neurons for ILD sensitivity using in vivo whole-cell recordings in the rat. We focused on two distinct classes of binaural selectivity: contralateral-preferring (EO) cells, which fire robustly to contralateral stimulation, and predominantly-binaural (PB) cells, which fire robustly when both ears receive simultaneous sounds of equal levels (ILDs near zero), but not to monaural stimulation.

Here we show the first direct evidence revealing how synaptic interactions construct spiking ILD selectivity in auditory cortical neurons. We found that EO cells received co-tuned excitation and inhibition, with excitation preceding inhibition by a few ms for all binaural stimuli. ILD selectivity in these cells was not shaped by local inhibition, indicating an inheritance processing strategy. Similar to EO cells, PB cells received minimal synaptic input at ipsilateral ILDs and proportional excitation and inhibition for midline ILDs. However, for contralateral ILDs, PB cells received disproportionately strong synaptic inhibition, which even preceded excitation in some cells, quenching spiking output. This is evidence for the local processing strategy. Our results demonstrate that for a specific class of auditory cortical cells, PB cells, cortical synaptic inhibition plays an active role in shaping the spiking representation of sound localization cues.

Methods

All procedures were in strict accordance with the National Institutes of Health guidelines as approved by the University of Oregon Animal Care and Use Committee.

Physiology

We recorded from neurons in the left auditory cortex of 59 anesthetized (30 mg/kg ketamine, 0.24 mg/kg medetomidine) albino rats (*Rattus norvegicus*, Sprague Dawley) aged 19 - 28 days postnatal (mean = 23.4, SD = 2.7). We used this age range to improve the yield of *in vivo* whole cell recordings (Kyweriga et al. 2014; Scholl et al. 2010). Rats older than 14-19 days, like adults, orient correctly toward sounds on the horizontal plane (Kelly et al. 1987). The critical period for hearing in rats is complete by approximately postnatal day 14 (de Villers-Sidani et al. 2007), although some limited additional maturation of receptive fields and synaptic markers (e.g., NR1, GluR2, and GAD65) occurs until approximately postnatal day 28 (Chang et al. 2005; Lu et al. 2008; Popescu and Polley 2010; Xu et al. 2007, 2010).

At the beginning of each experiment we used multi-unit recordings (1-2 MΩ tungsten microelectrodes, FHC) to coarsely map the auditory cortex. We sought to locate sites with robust binaural response properties. We targeted both primary auditory cortex (A1) and the suprarhinal auditory field (SRAF), which contains a relatively high proportion of PB cells (Higgins et al. 2010). We identified A1 from the caudal-rostral tonotopic gradient. We identified SRAF from the absence of auditory evoked responses along its ventral border (Higgins et al. 2010; Polley et al. 2007).

Single-unit recordings

We obtained single-unit recordings with the loose cell-attached patch method, which provides excellent single-unit isolation. We only included cells in our sample if they had at least one spike following stimulus onset to 75 ms following stimulus offset (0-100 ms) with a minimum of five trials per stimulus combination (n = 58 cells). Subpial depth for these cells ranged from 210 to 925 µm (mean = 561.0 µm, SD = 172.9), as determined from micromanipulator travel. Approximately 80% of these cells were located in A1 or SRAF with the remainder from either ventral (VAF) or posterior (PAF) auditory field.

Whole-cell recordings

We used standard blind patch-clamp methods to obtain 58 whole-cell recordings. We only included cells in our sample if they had at least one spike following stimulus onset to 75 ms following stimulus offset (0-100 or 0-175 ms for 25 and 100 ms stimuli, respectively) and a minimum of five trials per stimulus combination (n = 58 cells). Subpial depth for these cells ranged from 187 to 857 µm (mean = 450.0 µm, SD = 167.1). Our whole-cell recordings with both spiking and conductance data (28 cells) were located in either A1 (12 EO and 8 PB) or SRAF (3 EO and 5 PB). We did not use voltage-gated channel blockers in the pipette solution, so that we could record both spiking output and synaptic currents from the same cells. The internal solution contained (in mM), 120 K-gluconate, 2 $MgCl_2$, 0.05 $CaCl_2$, 4 MgATP, 0.4 NaGTP, 10 Na_2Phosphocreatine, 13 BAPTA, 10 HEPES, pH 7.28, diluted to 297 mosM, producing a calculated inhibitory reversal potential of -91.1 mV and an excitatory reversal potential of 3.4 mV. We corrected for a calculated liquid junction potential of 15.0 mV (Barry 1994), based on standard extracellular ionic concentrations (Sykova 1997), body temperature of 37ºC, and dilution of our internal solution concentrations by ~10% (to achieve physiological osmolarity).

Many cells recorded in current-clamp did not spike at rest (I=0 mode; Hromadka et al. 2008), but since many showed robust membrane potential depolarizations evoked by our stimulus array, we injected positive current to promote spiking in current-clamp mode (43-403 pA; mean = 147.6, SD = 98.3; n = 20 cells).

In a subset of spiking cells we also obtained voltage-clamp recordings in order to measure inhibitory and excitatory synaptic conductances. Holding potentials were stepped (with a 1-s ramp) to a pseudorandom sequence of two values using an Axopatch 200B amplifier. At each potential, after a 1-s equilibration period, ten 10-mV voltage pulses were delivered to monitor series and input resistance, followed by acoustic stimuli. Across the voltage-clamp population, input resistance was 47.0 ± 25.8 MΩ, and series resistance was 40.1 ± 5.7 MΩ (median ± interquartile range, n = 28 cells). We measured synaptic currents at two holding potentials (mean = -110.6, SD = 6.9 mV, and mean = +27.6, SD = 23.9 mV; corrected for series resistance and liquid junction potential) and for 5-10 trials (median 10) for each acoustic stimulus. Synaptic conductances, corrected for series resistance, were computed off-line assuming an isopotential neuron (for details, see Wehr and Zador 2003). Deviations from this assumption lead to underestimates of the magnitude of conductances. Thus, all of our results are presented as relative measurements within cells, and are normalized for group data analysis. To ensure high-quality voltage-clamp recordings, we only included cells with conductances greater than 0.5 nS to at least 5 stimulus combinations, resulting in a sample of 28 neurons.

In summary, we recorded from 116 cells: 58 spiking cells with the cell-attached method and 58 spiking cells with the whole-cell current-clamp method. Our whole-cell data set contained 28 cells recorded in voltage-clamp mode.

Sound stimuli

Sound source localization depends on three cues: (1) Spectral cues due to the shape of the listener's head, pinnae, and hair, (2) Interaural Time Difference (ITD), and (3) ILD. A recent study suggests that rats are unable to use ITD cues in sound localization tasks (Wesolek et al. 2010). We therefore used stimuli with ILD as the only sound localization cue. All stimuli were generated with custom software in MATLAB (MathWorks, Natick, MA) at a sampling rate of 192 kHz with a Lynx-TWO-B sound card and delivered with Etymotics ER-2 earphones in sealed ear configuration. These earphones were suitable for our experiments as the rat audiogram is 7 octaves (0.5–64 kHz; Heffner et al. 1994; Kelly and Masterton 1977) and the ER-2 earphones cover over half of this range (4 octaves: 1–16 kHz). All experiments were performed in a double-walled sound isolation chamber with anechoic surface treatment. We sealed the Etymotics ER-2 earphones along with Knowles omnidirectional electret condenser microphones into each ear.

The sound level inside each ear canal was then calibrated with the Knowles microphones, which were in turn calibrated with a Bruel & Kjaer 4939 1/4" microphone prior to each experiment. To characterize binaural response properties we used pseudorandomly interleaved white noise bursts (25 or 100 ms duration) presented simultaneously to each ear from 10 to 50 decibel, in 10-dB steps (noise was not frozen between left and right or between each level). “dB” indicates decibel and “SPL” indicates Sound Pressure Level. This produced an array of 25 binaural stimuli, with a range of average binaural levels (ABLs; defined as the average of the levels presented to the 2 ears) from 10 to 50 dB, across a range of ILDs from -40 to +40 dB (corresponding to the maximum physiological range of ILD; Koka et al. 2008). Figure 5A shows this stimulus array with both coordinate systems included; ILD is on the *x-axis* and ABL is on the *y-axis,* whereas the levels in the ipsilateral ear and contralateral ear are on the diagonal axes (rotated by 45°). We also presented monaural sounds to each ear from 10 to 50 dB. These monaural responses are presented on each side of the binaural stimulus diamond (Fig. 5A) with ipsilateral (Ips) sounds on the left and contralateral (Con) sounds on the right. This format is maintained throughout this report. We restricted sound levels to a maximum of 50 dB because we noted that higher levels produced cross talk from one ear to the other, presumably due to sound transmission through the head (data not shown). We defined contralateral ILDs as positive. All stimuli had 5-ms onset and offset ramps with 500-ms interstimulus intervals.

At the beginning of each experiment we mapped auditory cortex with extracellular tungsten electrodes using pseudorandomly interleaved pure tone pips (25 ms duration) to the contralateral ear. We presented four tones per octave from 1 to 16 kHz, at 5 levels from 10 to 50 dB (SPL). All stimuli had 5 ms onset and offset ramps with 500 ms interstimulus intervals. Characteristic frequency was designated as the frequency that evoked responses at the lowest intensity. We were typically unable to measure the characteristic frequency of our whole-cell recordings due to time constraints.

For whole cell recordings, we first recorded membrane potential responses to our stimulus set in current-clamp mode. Then we switched to voltage-clamp mode and measured the synaptic currents evoked by the same stimuli. Because of time constraints, we were often unable to record a voltage-clamp protocol with more than 5 trials for each holding potential, hence the reduced sample size (n = 28).

Classification of cells

To investigate the role of excitation and inhibition in cortical neurons responding to binaural stimuli, we first classified the spiking output of cells according to the monaural and binaural response categories presented by Kitzes and colleagues (Zhang et al. 2004; see their Fig. 1), and then investigated the role of excitation and inhibition. Cells for which monaural sounds elicited firing rates 3 times above baseline firing rate for at least 2 sound levels were designated as "E", otherwise as "O," for each ear. By convention we listed the contralateral ear first, followed by the ipsilateral ear. For example, a cell responding only to contralateral sounds was designated "EO". If a cell was unresponsive to monaural sounds in either ear (OO), but responded significantly to at least 5 binaural sounds, it was classified as predominantly binaural (PB). Cells failing to meet these criteria were considered unresponsive and were excluded from further analysis. While responsive cells likely exist on a continuum instead of discrete categories (Campbell et al. 2006), here we grouped our cells into four categories to specifically test whether these groups have distinct synaptic processing strategies. Thus, cells could be classified as EO (preferring contralateral sounds), OE (preferring ipsilateral sounds), EE (preferring both contralateral and ipsilateral sounds), or PB (unresponsive to monaural but responding predominantly to binaural sounds). In our sample of whole-cell recordings with both spiking and conductances, we only observed two cell types: the EO and PB groups.

Data analysis

To extract spikes, we first high-pass filtered extracellular and intracellular recorded voltages at 300 Hz (Butterworth filter) and used an absolute threshold of 1–5 mV (median = 5 mV; mean = 3.8 mV, SD = 1.8). We quantified spiking responses by counting spikes in a 100 ms window (for 25 ms stimuli) or a 175 ms window (for 100 ms stimuli) following sound stimulus onset. We determine baseline firing rate from the time-averaged firing rate across the entire recording session (from sound onset of the first sound presented to 500 ms following the final stimulus).

To compute the ratio of excitation to inhibition we divided the peak of excitation by the sum of the peaks of excitation and inhibition. This produces a set of ratios that ranges from 0 (no excitation) to 1 (no inhibition), with 0.5 corresponding to equal peak conductances. To minimize the effects of potential errors in the estimation of absolute excitatory and inhibitory conductance amplitudes, we compared relative conductances within each cell. To perform ratio group analysis across cells, we first calculated the ratio for all stimulus combinations and then subtracted the lowest ratio from all stimulus combinations. We then divided all these by the highest ratio. This produced a range of ratios in each cell between 0 and 1. Very small excitatory and inhibitory responses did not contribute to spiking, but very small values in the ratio denominator could lead to numerically unstable ratios. We therefore excluded stimulus combinations with conductances below 1 nS in the ratio analysis.

Results

Neurons in auditory cortex are tuned to a range of interaural level differences

We classified auditory cortical neurons into 4 categories (EE, EO, OE, or PB) based on their spiking responses to monaural and binaural ILD stimuli (Fuzessery et al. 1990; Zhang et al. 2004). Here E denotes monaurally-responsive and O denotes unresponsive, with the contralateral ear listed first. For example, an EO cell is responsive to monaural contralateral sounds, but not monaural ipsilateral sounds. Figure 5 shows examples and group data for each of these 4 cell types.

Figure 5A shows a representative example of an EO cell. This cell responded robustly to contralateral monaural sounds (Con; vertical bar on right side), but not to ipsilateral monaural sounds (Ips; vertical bar on left side). Binaural stimuli elicited strong responses to ILDs from 0 to +40 dB, but not to ILDs from -40 to -10 dB. The response profile of this EO cell was typical of all of our EO cells (Fig. 5B; n = 50 cells), which comprised 43.1% of our sample.

Figure 5C shows a representative example of an OE cell. This cell responded robustly to ipsilateral monaural sounds, but not to contralateral monaural sounds.

Binaural stimuli elicited strong responses to ILDs from -40 to +10 dB, but not to ILDs from +20 to +40 dB. This response profile was typical of OE cells (Fig. 5D; -40 to 0 dB; n = 17 cells), which comprised only 14.7% of our spiking sample. We did not obtain any whole-cell recordings from OE cells.

Figure 5E shows a representative example of an EE cell. This cell responded robustly to both contralateral and ipsilateral monaural sounds, and across all ILDs. This response profile was typical of all EE cells (Fig. 5F; n = 7 cells), which were quite rare and comprised only 6% of our spiking sample. We did not obtain any whole-cell recordings from EE cells.

Figure 5G shows a representative example of a PB cell. This cell was unresponsive to monaural sounds, and would therefore be categorized as OO based only on monaural responses. However, this cell responded robustly to ILDs from -10 to 0 dB, which was was typical of PB cells (Fig. 5H; n = 42 cells). PB cells comprised 36.2% of our spiking sample.

Contralateral-preferring cells inherit binaural response properties

We found that EO cells in rat auditory cortex inherited their binaural response properties. Figure 6 shows a representative example of an EO cell. The top traces (black) in Fig. 6A show membrane potential responses at 5 ILDs from -40 to +40 dB at an average binaural level (ABL) of 30 dB. This cell spiked robustly to contralateral stimulation at ILDs from 0 to +40 dB. After we recorded membrane potential responses in current-clamp mode, we switched to voltage-clamp and recorded excitatory and

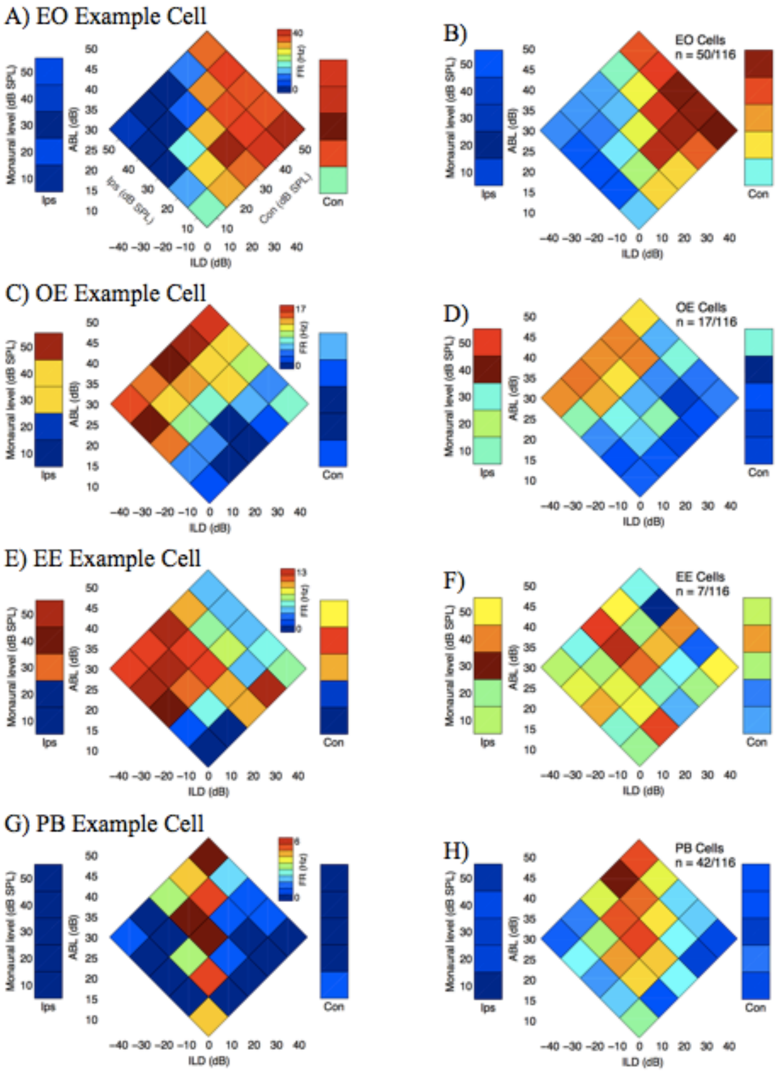

Figure 5. Representative examples (left column) and group data (right column) of spiking responses comprising four binaural cell classes. A) An example of an EO cell (072710-WS-4) that responded to contralateral monaural and binaural sounds. The axes on the left side bar (Ips) show monaural sound levels from 10 to 50 dB (same scale for Con, right side bar). The axes on the central binaural plot show ABLs from 10 to 50 dB and ILDs from -40 to +40 dB. These binaural sounds are composed of simultaneous monaural sounds denoted by the 45 degree rotated axes. These axes are consistent throughout this report. B) EO group data of normalized firing rate averaged across all cells. C) An example of an OE cell (080910-WS-3) that responded to ipsilateral monaural and binaural sounds. D) OE group data. E) An example of an EE example cell (080210-WS-1) that responded to monaural sounds from both ears and across all ILDs. F) EE group data. G) An example of a PB example cell (120810-MK-4) that was unresponsive to monaural sounds but responded strongly to ILDs from -10 to +10 dB. H) PB group data. Dark red indicates high firing rate and dark blue indicates lack of response. ABL: Average Binaural Level; dB: decibel; FR: Firing Rate; ILD: Interaural Level Difference; SPL: Sound Pressure Level.

inhibitory currents and computed the synaptic conductances (bottom traces). Synaptic excitation (green) had the same ILD sensitivity as spiking output, and inhibition (red) was proportional to excitation. Figure 6B shows that this relationship remained consistent throughout all sound combinations in the full array of monaural and binaural sounds. Note that Fig. 6A is an excerpt from Fig. 6B (purple panels, center row). This cell responded robustly to monaural contralateral sounds and binaural ILDs greater than -10 dB.

We next determined how excitatory-inhibitory interactions contributed to spiking output in the same neuron. To do this we asked how firing rate depended on excitation and inhibition, using linear regression analysis (Fig. 6C-E). Firing rate strongly depended on excitatory conductance (Fig. 6C; $R^2 = 0.69$, $p = 3.8\times10^{-10}$; $n = 35$ stimulus combinations). Firing rate also depended significantly on inhibitory conductance (Fig. 6D; $R^2 = 0.68$, $p = 6.4\times10^{-10}$, $n = 35$ stimulus combinations), which may seem surprising at first glance, because inhibition usually suppresses rather than increases spiking output. However, excitation was tightly correlated with inhibition ($r = 0.96$, $p = 1.4\times10^{-20}$, $n = 35$ stimulus combinations), indicating co-tuning of excitation and inhibition, as has been previously reported (Wehr and Zador 2003). Indeed, firing rate was not significantly correlated with inhibition after controlling for the effect of excitatory conductance (partial correlation = 0.17, $p = 0.32$). Furthermore, spiking did not depend on the ratio of excitation to inhibition (Fig. 6E; $R^2 = 0.0$, $p = 0.73$). The relative timing of excitation to inhibition can affect spiking output. For example, inhibition typically lags behind excitation by a few milliseconds (Wehr and Zador 2003), but in some cases the timing of

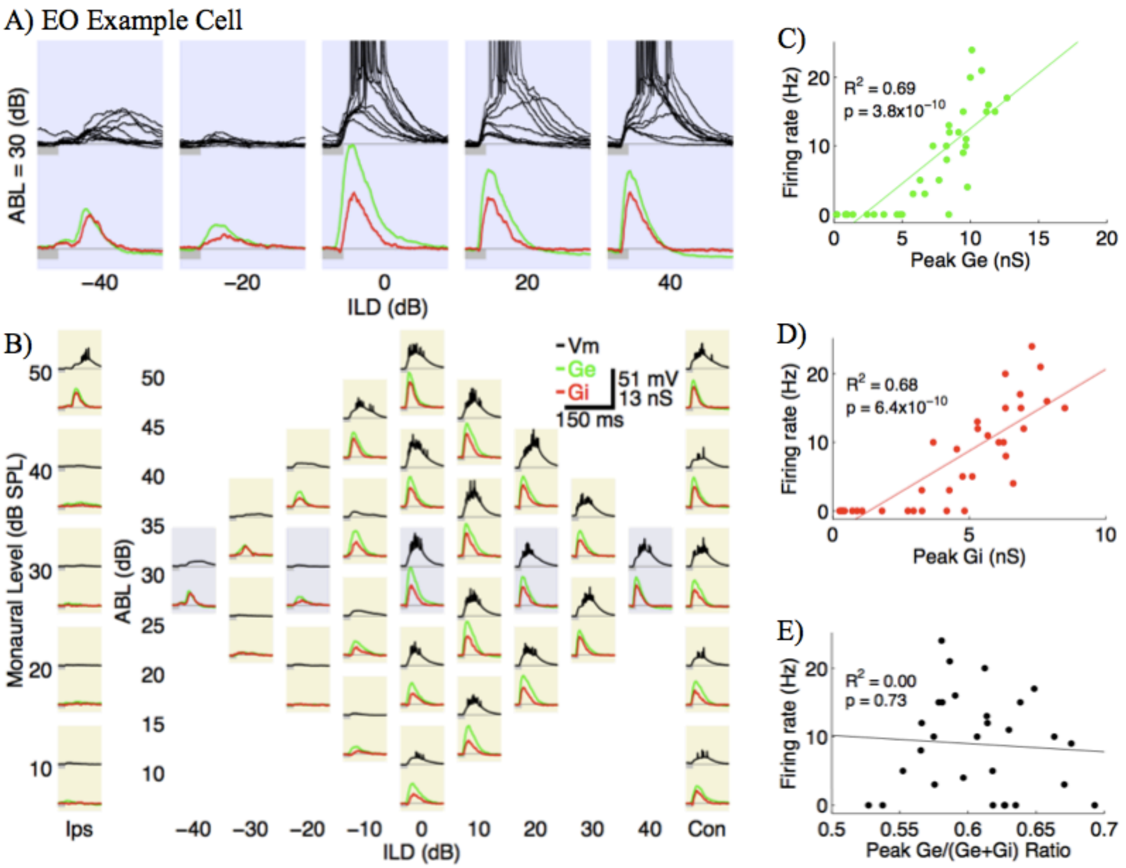

Figure 6. Representative example of a contralateral-preferring cell (120810-MK-3) showing inheritance. A) Top traces (black) show membrane potential at 5 ILDs (ABL = 30 dB) with strong spiking responses from 0 to +40 dB (n = 10 trials for each ILD; spikes are truncated). Resting membrane potential is thin gray line (-67.7 mV). Bottom traces show excitation (Ge: green) and inhibition (Gi: red). Stimulus: 25 ms white noise burst (gray bars). B) Complete binaural and monaural response map. Monaural sounds are columns on each side with ipsilateral (Ips) on the left and contralateral (Con) on the right. The binaural stimulus map is the middle diamond. Note that Fig. 6A is an excerpt from 6B (purple panels). C-E) Regressions showing relationship between firing rate and conductance measures. Increases in excitation (C) and inhibition (D) strongly predicted increased firing rate. The ratio of excitation to inhibition (E) did not predict firing. In (E), 6/35 stimulus combinations with excitation and inhibition less than 1 nS were excluded (see Methods).

inhibition can reduce firing rates when it becomes coincident or precedes excitation (Higley and Contreras 2006). For this EO cell, the relative timing between excitation and inhibition did not affect spiking output, since spiking showed a negative dependence on inhibitory delay ($R^2 = 0.23$, $p = 8.8 \times 10^{-3}$, n = 29/35 stimulus combinations). In this cell, inhibition lagged behind excitation across all stimulus combinations with a mean delay of 3.5 ms (SD = 2.9). To further show the co-tuning of excitation and inhibition with firing rate we plotted excitation and inhibition (Fig. 7A) and depicted the firing rate by circle size. Here the highest firing rates are located in the upper right quadrant. Since the dependence of firing rate on excitation and inhibition suggested a linear threshold (see Fig. 6 C-E), we found the minimal root mean square (RMS) error by exploring 100 thresholds and 100 slopes for both excitation (Fig. 7B) and inhibition (Fig. 7C). These results indicate that the ILD sensitivity of the spiking output was inherited from that of the excitatory input and that the co-tuned inhibition did not actively shape the ILD sensitivity of the cell.

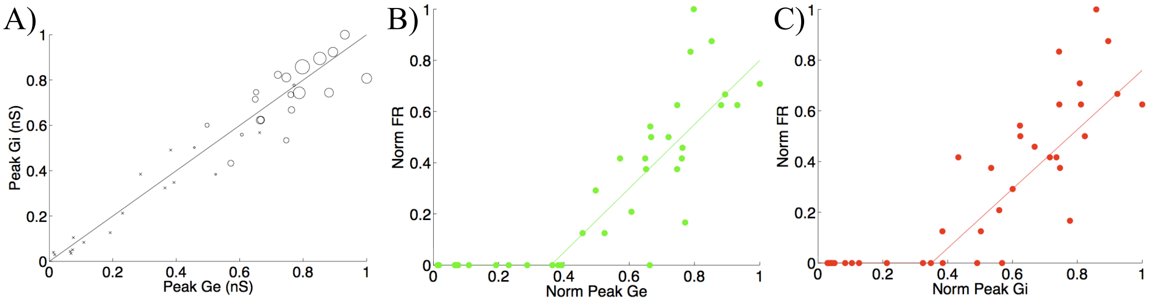

Figure 7. Representative example of a contralateral-preferring cell (120810-MK-3) showing co-tuning of excitation and inhibition. A) Peak excitation (Ge) and peak inhibition (Gi) are highly correlated and firing rate depends on peak synaptic input (x: no spikes, larger circles denote higher firing rates). Note that these values straddle the line of unity and the highest firing is in the upper left quadrant. Threshold-linear fits for peak excitation (B; Ge: green) and inhibition (C; Gi: red) reduced RMS error (compare with Fig. 6 C&D).

Figure 8 shows spiking and conductance data for all 15 EO cells. Figure 8A shows the population spiking responses of EO cells after normalizing to their peak firing rates and averaging. These cells spiked to contralateral monaural sounds and to ILDs from 0 to +40 dB. Synaptic excitation and inhibition showed the identical pattern. On average, EO cells received strong excitation to monaural sounds and to ILDs from 0 to +40 dB (Fig. 8B). Similarly, these cells received strong inhibition to monaural sounds and to ILDs from 0 to +40 dB (Fig. 8C). As in the example cell above (Fig. 6), excitation and inhibition closely matched the spiking output of EO cells. To demonstrate this, we calculated the ratio of peak excitation to the sum of peak excitation and peak inhibition, normalized to the range 0 to 1 for each cell. Across the population (Fig. 8D), this ratio was essentially equal across all stimulus combinations (light brown color).

To directly assess how firing rate depended on excitation and inhibition, we again used linear regression analysis. Figure 8E-G shows, for all EO cells, the same linear regressions as shown for the example cell above (Figure 6C-E). Across the population, spiking output significantly depended on synaptic excitation (Fig. 8E; $R^2 = 0.24$, $p = 1.4 \times 10^{-33}$). Because of co-tuning, spiking output also depended on inhibition (Fig. 8F; $R^2 = 0.16$, $p = 1.1 \times 10^{-21}$), and excitation and inhibition were tightly correlated ($r = 0.74$, $p = 6.1 \times 10^{-94}$). Thus after accounting for excitation, inhibition was no longer predictive of firing (partial correlation = 0.06, p = 0.16). The spiking of EO cells was independent of the ratio of peak excitation to the sum peak of excitation and inhibition (Fig. 8G; $R^2 = 0.01$, $p = 0.23$). Lastly, we found a weak and negative dependence on the relative timing between excitation and inhibition ($R^2 = 0.02$, $p = 0.03$). We conclude that the ratio and

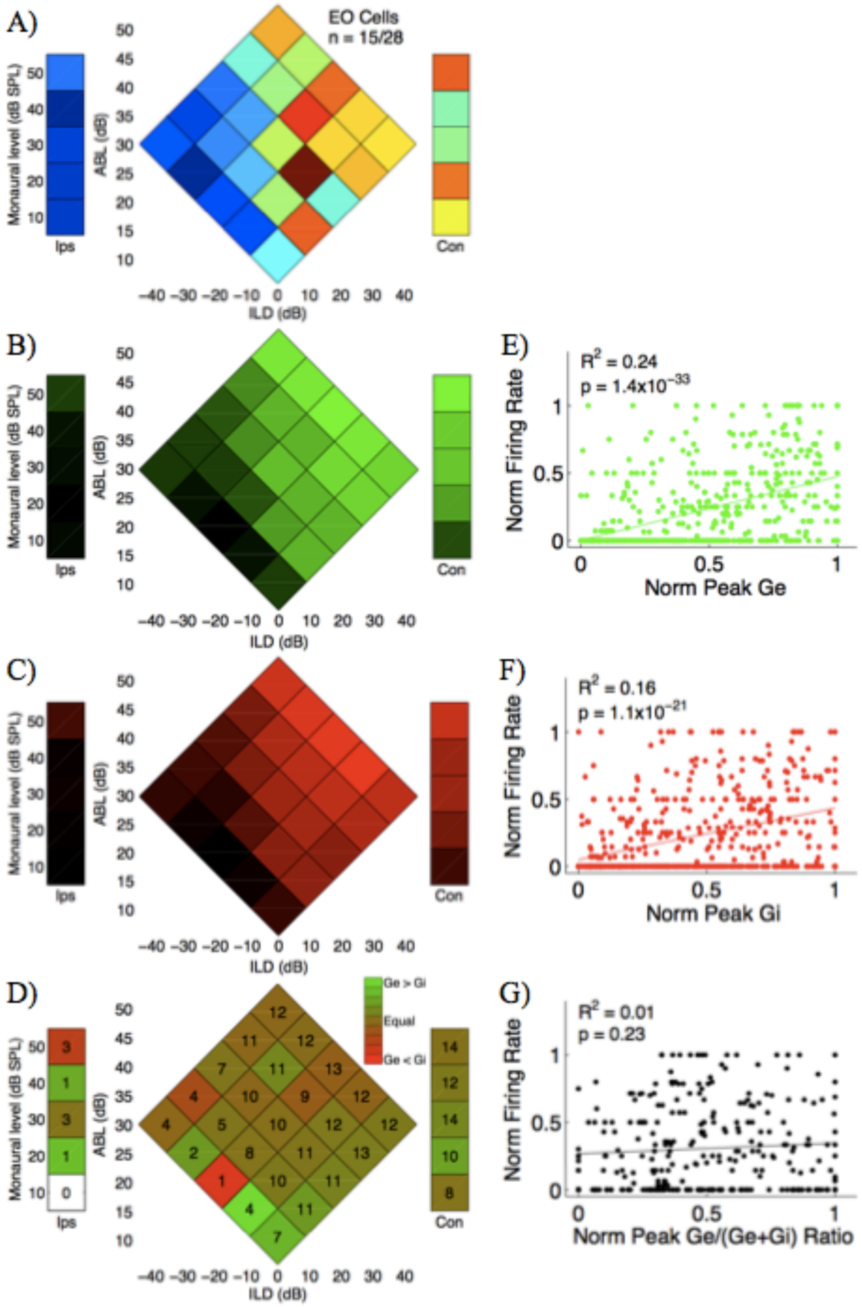

Figure 8. Whole-cell group data showing that contralateral-preferring cells inherit their spiking response profiles (n = 15 cells). A) Averaged normalized firing rate. Maximal responses are red and minimal responses are blue. B) Averaged normalized peak excitatory conductances. C) Averaged normalized peak inhibitory conductances. B & C: maximal conductances are colored and minimal conductances are black. D) Averaged normalized ratio of excitation to inhibition. Number of cells included are overlaid on each stimulus combination. Note that the few unbalanced ratios (bright red or green) are due to increased variance from low N. E-G) Linear regression analysis between firing rate and conductance measures. Firing rate was strongly dependent upon peak excitation (E) and peak inhibition (F), but independent of the ratio of excitation to inhibition (G).

relative timing of excitation and inhibition did not have a role in shaping the spiking ILD selectivity of EO cells.

To further explore the co-tuning of EO cells we performed linear-threshold fits for each cell in an effort to reduce the root mean square (RMS) error. Figure 9 shows all 15 linear-threshold slopes for excitation (Fig. 9A) and inhibition (Fig. 9B). These slopes were not significantly different (Fig. 9C; Paired t-test, p = 0.21), nor was the RMS error (Fig. 9D; Paired t-test, p = 0.052).

These results taken together suggest that the monaural and binaural ILD sensitivity of EO cells is inherited. The spiking output of EO cells depended simply upon the total magnitude of synaptic conductance. For non-preferred ILDs and monaural sounds, EO cells did not fire simply because they received little or no synaptic input.

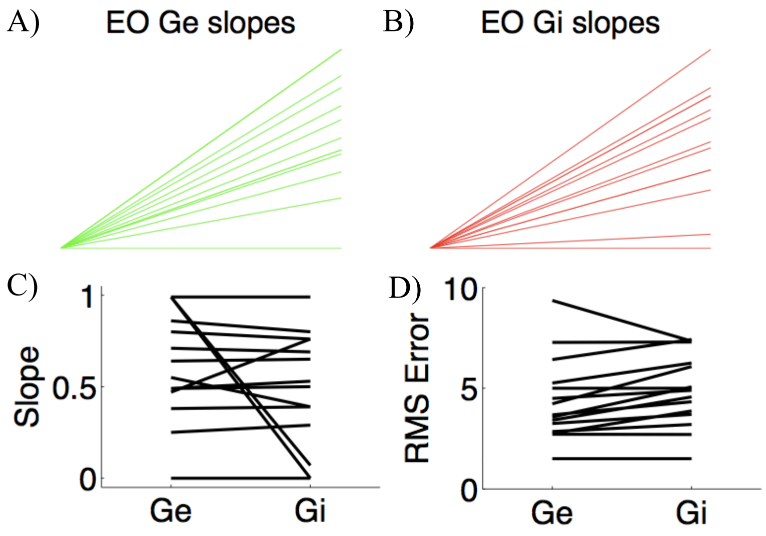

Figure 9. Whole-cell group data showing co-tuning in contralateral-preferring cells using linear-threshold fits (n = 15 cells). Both excitation (A; Ge: green) and inhibition (B; Gi: red) when adjusted for spiking threshold had similar slopes (C) and similar RMS error (D).

Predominantly-binaural cells exhibit synaptic computation of binaural response properties

PB cells showed a strikingly different pattern of synaptic input than EO cells. Rather than the inheritance strategy, PB cells displayed evidence of the local processing strategy. Figure 10 shows a representative example of a PB cell. The top traces (black, Fig. 10A) show membrane potential responses at 5 ILDs from -40 to +40 dB. This cell spiked robustly only to a narrow range of ILDs from -20 to 0 dB. In contrast to EO cells, the balance of excitation and inhibition depended strongly on ILD. At -20 dB ILD, excitation and inhibition were approximately balanced, which drove robust spiking responses. However, at +20 and +40 dB ILD inhibition far outweighed excitation, and the cell fired no spikes. The full binaural array in Figure 10B shows that spiking in this cell was unresponsive to monaural stimuli, but was robust for ILDs of -30 to +10 dB (top traces, black). The imbalance of inhibition at contralateral ILDs is apparent in the bottom red and green traces. For ipsilateral monaural sounds and ILDs of -40 to -10 dB, peak excitation and inhibition were roughly equal. However, for contralateral ILDs (0 to +40 dB) there was both a withdrawal of excitation and very strong inhibition that together prevented spiking output.

To quantify how these synaptic interactions shaped spiking output, we asked how firing rate depended on excitation and inhibition using linear regression analysis (Fig. 10C-E). Firing rate strongly depended on excitatory conductance (Fig. 10C; $R^2 = 0.59$, $p = 4.6 \times 10^{-8}$; n = 35 stimulus combinations), but only weakly depended on inhibitory conductance (Fig. 10D; $R^2 = 0.14$, $p = 0.025$, n = 35 stimulus combinations). This makes sense, because unlike in EO cells, which showed co-tuning of excitation and inhibition (r = 0.96 for the EO cell in Fig. 7), synaptic excitation and inhibition in this PB cell were less correlated ($r = 0.85$, $p = 3.3 \times 10^{-11}$). When we controlled for the effect of excitatory conductance, firing rate was strongly negatively correlated with inhibition (partial correlation: $r = -0.85$, $p = 7.6 \times 10^{-11}$). This lack of co-tuning is a signature of the local processing strategy: as inhibition increased, spiking decreased. Accordingly, spiking was dependent on the ratio of excitation to inhibition (Fig. 10E; $R^2 = 0.54$, $p = 1.2 \times 10^{-5}$), unlike EO cells. In this cell, the relative timing between excitation and inhibition weakly affected spiking output ($R^2 = 0.22$, $p = 0.01$, n = 27/35 stimulus combinations). As the inhibitory lag decreased, so too did the firing rate. For this cell, inhibition lagged behind excitation at negative ILDs (see Fig. 10A at ILDs of -40 and -20 dB), but preceded excitation at positive ILDs (see Fig. 10A at ILDs of +20 and +40 dB), adding to inhibitory shaping of the spiking output of the cell.

To further examine the role of inhibition in the shaping of PB cells, we plotted excitation against inhibition with firing rate depicted by circle size (Fig. 11A). Above the line of unity there is a cluster of non-spiking stimulus combinations (x’s). These data show that unlike EO cells, PB cells utilize strong inhibition to suppress spiking output when they would otherwise spike (Note circles below the line of unity where inhibition prevented spiking). The linear-threshold fits for excitation (Fig. 11B) and inhibition (Fig. 11C) both had reduced RMS error when compared with the linear regressions in Figure 10 C&D. These results indicate that the spiking output of this PB cell were strongly shaped by excitatory-inhibitory interactions. At ipsilateral and central ILDs, the spiking

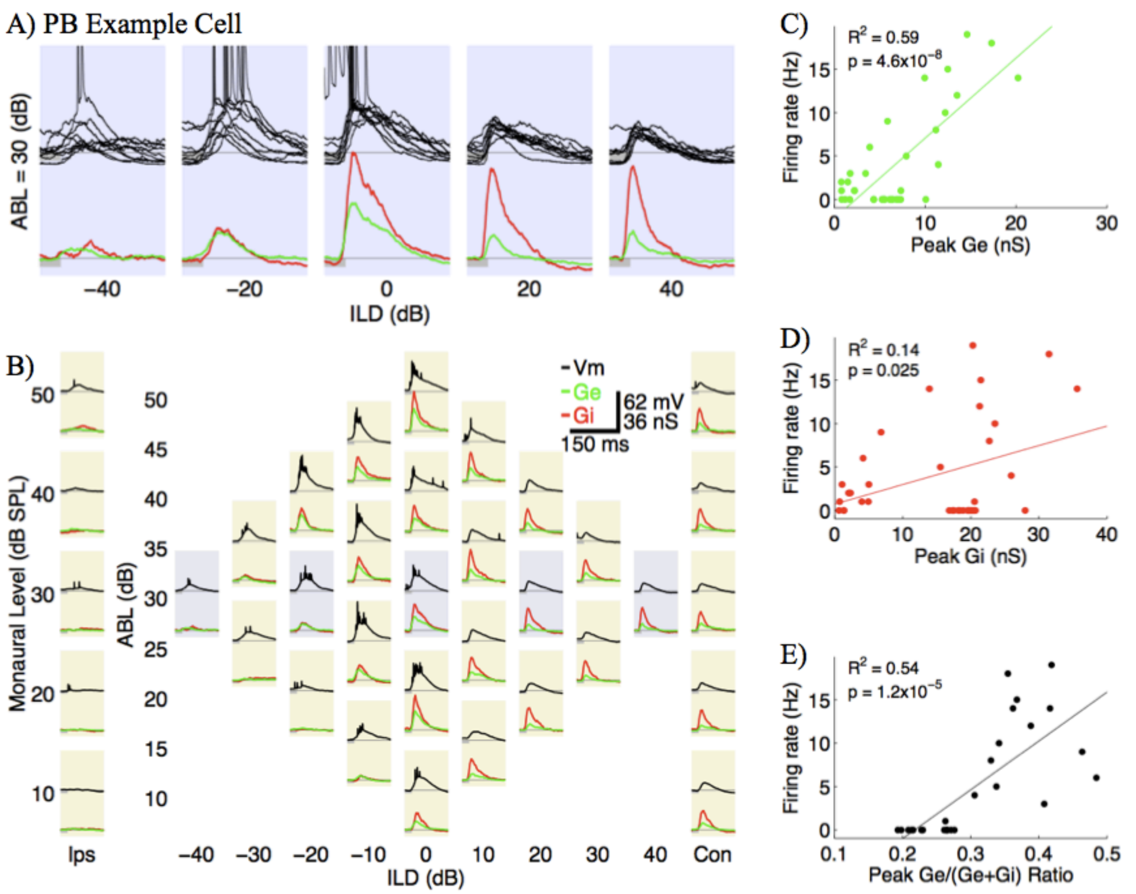

Figure 10. Representative example of a predominantly-binaural cell (120810-MK-5), showing the local processing strategy. A) Top traces (black) show membrane potential at 5 ILDs (ABL = 30 dB) showing strong spiking responses to ILDs at -20 and 0 dB ILD (10 trials for each ILD; spikes are truncated). Resting membrane potential is thin gray line (-61.8 mV). Bottom traces show excitation (Ge: green) and inhibition (Gi: red). Stimulus: 25 ms white noise burst (gray bars). B) Complete binaural and monaural response map. Note that Fig. 10A is an excerpt from 10B (purple panels). C-E) Regressions showing relationship between firing rate and conductance measures. Excitation strongly predicted the firing rate (C), but inhibition only weakly (D). The ratio of excitation to inhibition (E) predicted firing rate. In (E), 8/35 stimulus combinations with peak excitation and peak inhibition less than 2 nS were excluded.

response of this PB cell was driven by a volley of balanced excitation and inhibition. At contralateral ILDs, however, spiking was quenched by inhibition that was both more powerful than and preceded excitation.

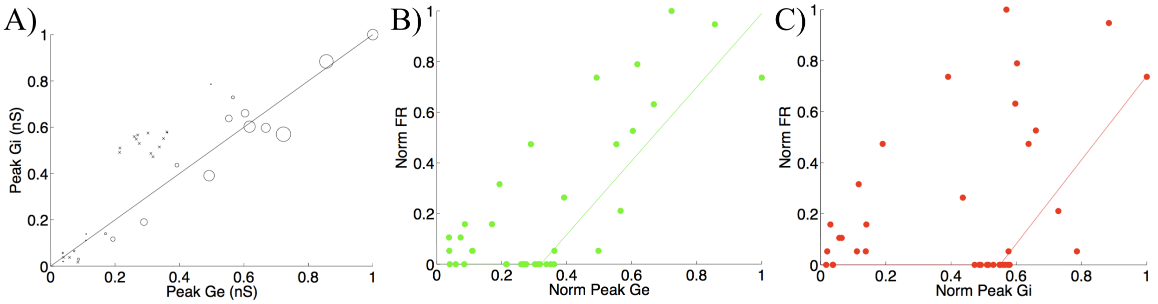

Figure 11. Representative example of a predominantly-binaural cell (120810-MK-5) showing local processing of spiking output. A) Peak excitation (Ge) and peak inhibition (Gi) are moderately correlated and firing rate does not always depend on peak synaptic input (x: no spikes, larger circles denote higher firing rates). Note that unlike the EO cell in Fig. 7 there is a cluster of non-spiking stimulus combinations above the line of unity. Threshold-linear fits for peak excitation (B; Ge: green) and inhibition (C; Gi: red) reduced RMS error, but not as well as we observed for EO cells (compare with Fig. 6 C&D and Fig. 7).

Across the population (Fig. 12), PB cells were generally very similar to the example cell shown in Figure 10. PB cells were unresponsive to monaural sounds and fired predominantly to ILDs near 0 dB (Fig. 12A). They received strong excitation at central ILDs from -20 to +20 dB, and modest excitation at contralateral monaural sounds and ILDs at +30-40 dB. However, these cells received strong contralateral inhibition to monaural sounds and ILDs from -10 to +40 dB (Fig. 12C). As shown for the example PB cell (Fig. 10), inhibition far outweighed excitation at contralateral ILDs and monaural contralateral sounds, across all PB cells. Excitatory input showed some weak selectivity for best ILD, indicating that the PB spiking response profiles were partially inherited. However, spiking at contralateral ILDs was suppressed by inhibitory drive that overpowered excitation (Compare Figure 12A with 12 B&C). To further demonstrate how these excitatory-inhibitory interactions drove spiking output, we again normalized the ratio of peak excitation to the sum peak of excitation and inhibition (as we did above for EO cells). Figure 12D shows that excitation and inhibition were *not* co-tuned, but rather, that the relative contributions of excitation and inhibition varied systematically with ILD. The E/I ratio at ipsilateral ILDs from -40 to -10 dB showed more excitation (green), however, at contralateral monaural sounds and ILDs from 0 to +40, inhibition was much stronger than excitation (red; compare Fig. 12D with Fig. 8D).

To directly assess how firing rate depended on excitation and inhibition, we again used linear regression. Figure 12E-G shows, for all PB cells, linear regressions of firing rate to synaptic input. As with the example PB cell shown in Figure 10, spiking output significantly depended on synaptic excitation in all PB cells (Fig. 12E; $R^2 = 0.18$, $p = 3.6x10^{-22}$). However, spiking output was only weakly dependent on inhibition (Fig. 12F; $R^2 = 0.02$, $p = 3.3x10^{-3}$). This suggests that inhibition actively suppressed the spiking output of most PB cells. Similar to EO cells, excitation and inhibition were correlated ($r = 0.57$, $p = 5.9x10^{-41}$), but when accounting for excitation, spiking output of PB cells was negatively correlated with inhibition (partial correlation = -0.14, $p = 2.1x10^{-3}$). Accordingly, and in contrast with EO cells, the ratio of excitation and inhibition had a strong role in shaping the spiking output of PB cells (Fig. 12G; $R^2 = 0.22$, $p = 3.2x10^{-16}$). In a subset of PB cells (3/13, e.g. Fig. 10), spiking showed a significant dependence on the timing of excitation to inhibition, but this was not true at the population level ($R^2 = 0.0$, $p = 0.33$). To further explore the inhibitory shaping of PB cells we performed linear-threshold fits for each cell in an effort to reduce the root mean square (RMS) error. Figure 13 shows all 13 linear-threshold slopes for excitation (Fig. 13A) and inhibition (Fig. 13B). Excitatory slopes were significantly greater than inhibitory slopes (Fig. 13C; Paired

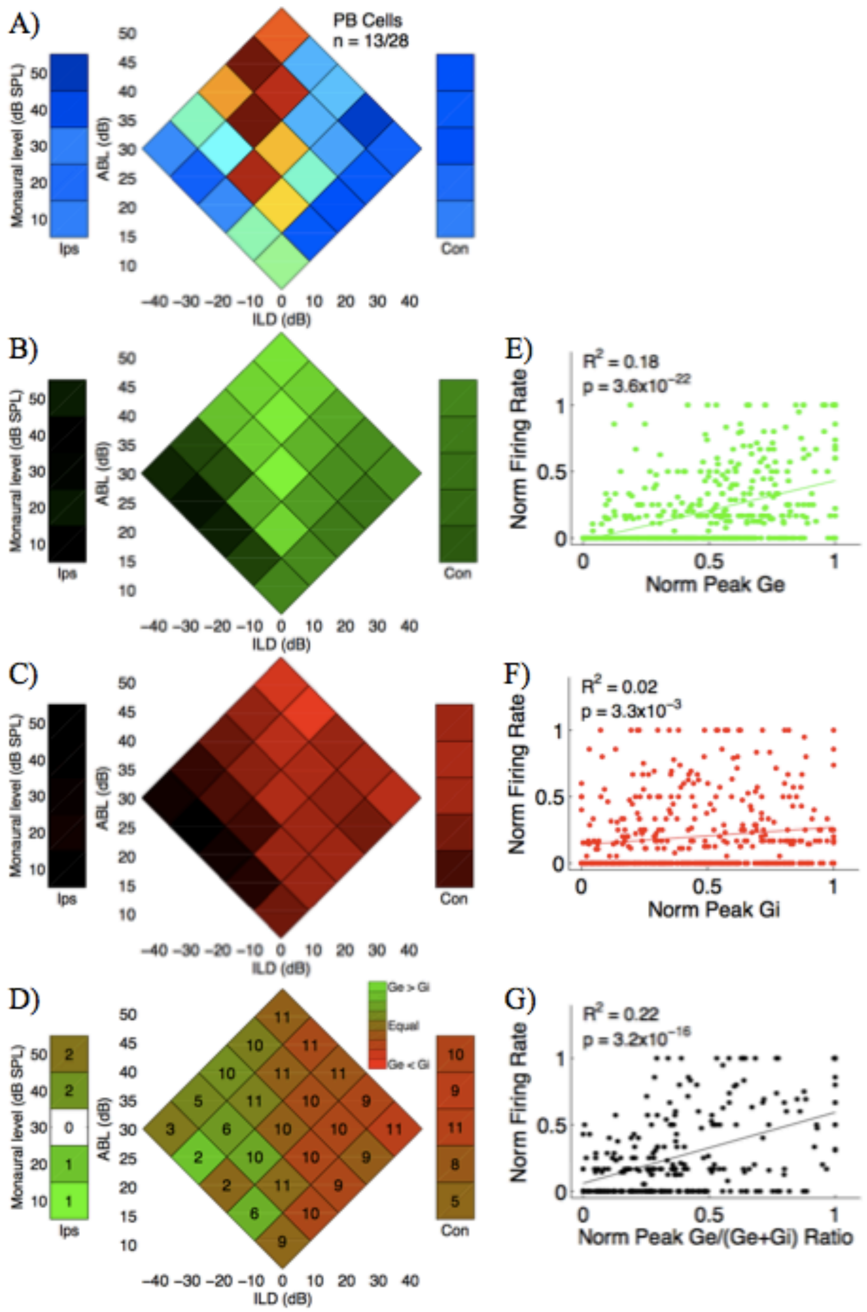

Figure 12. Whole-cell group data showing that the spiking of predominantly-binaural cells (n = 13) is controlled by excitatory-inhibitory interactions (local processing). A) Averaged normalized firing rate. Maximal responses are red and minimal responses are blue. B) Averaged normalized peak excitatory conductances. C) Averaged normalized peak inhibitory conductances. In Fig. 12 B & C maximal conductances are colored and minimal conductances are black. D) Averaged normalized ratio of excitation to inhibition. Number of cells included are overlaid on each stimulus combination. E-G) Linear regression analyses between firing rate and conductance measures. Firing rate was strongly dependent on peak excitation (E), but more weakly dependent on inhibition (F). G) Firing rate was strongly dependent on the ratio of excitation to inhibition.

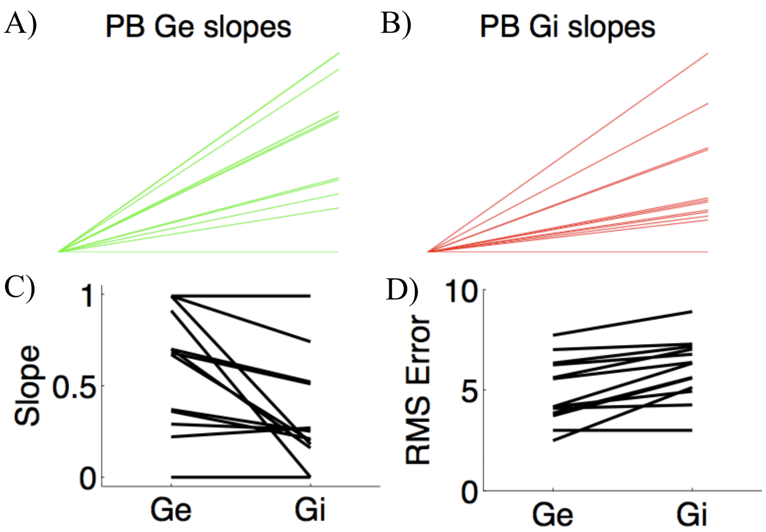

Figure 13. Whole-cell group data showing inhibitory shaping of predominantly-binaural cells using linear-threshold fits (n = 13 cells). Excitation (A; Ge: green) had significantly higher slopes than inhibition (B; Gi: red) when adjusted for spiking threshold had similar slopes (C). The RMS error was significantly greater for inhibition than excitation (D).

t-test, p = 0.008). Additionally, the RMS error was significantly greater for inhibition (Fig. 13D; Paired t-test, $p = 3.6 \times 10^{-4}$).

Taken together, these results indicate that PB cells in auditory cortex show local synaptic processing of binaural ILD cues. At central ILDs, spiking output in these cells directly depended upon the magnitude of synaptic conductances. In contrast, at contralateral ILDs PB cells received strong excitation, but did not spike due to even more powerful synaptic inhibition.

We finally directly compared the role of inhibition in shaping spiking responses. Figure 14 shows the role of excitation and inhibition in the firing rate of all cells (higher firing rates are denoted by larger circles; lack of firing is denoted by red x's). EO cells are co-tuned (Fig. 14A) with spiking and non-spiking stimulus combinations straddling the line of unity. In contrast, PB cells show a disproportionate amount of non-firing stimulus combinations above the line unity with the majority of spiking responses occurring below the line of unity (Fig. 14B). These results emphasize the distinct processing strategies utilized by these two cell classes.

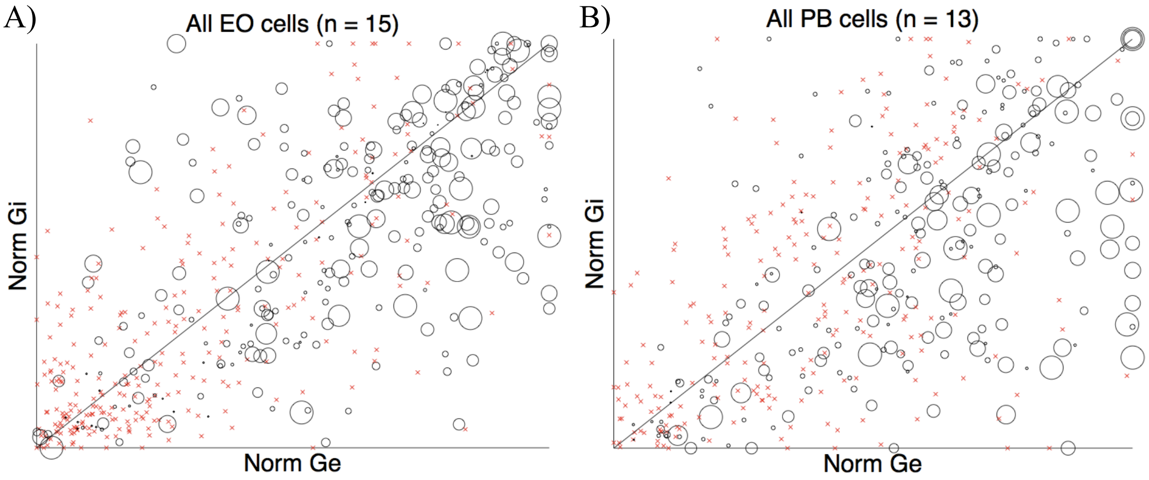

Figure 14. Whole-cell group data comparing the relationship between excitation (Ge) and inhibition (Gi) for EO and PB cells. Larger circles denote higher firing rates while red x's denote a lack of spiking. In EO cells (A) spiking responses straddle the line of unity, whereas in PB cells (B), spiking responses are more likely to be inhibited above the line of unity demonstrating local processing.

Discussion

Here we have demonstrated a novel role for inhibition in sensory cortex in the shaping of binaural sensitivity in predominantly binaural cells. These PB cells responded robustly when sound level was similar in each ear (ILDs near 0 dB). These cells were somewhat similar to contralateral-preferring (EO) cells in that ipsilateral monaural and binaural ILDs (-40 to 0 dB) evoked excitation and inhibition that was proportional, but usually too weak to evoke spiking output (ILDs from -40 to -20 dB). Both of these cell classes began to spike at ILDs near 0 dB, once they received sufficient excitation.

However, unlike EO cells, at contralateral monaural and binaural ILDs, PB cells received disproportionately stronger synaptic inhibition than excitation. This contralateral-evoked inhibition silenced spiking by reversing of the relative magnitudes of excitation and inhibition. In a few cases there was also a reversal of the relative timing of synaptic inhibition (3/13 PB cells).

Neurons in sensory cortex typically show co-tuning of excitation and inhibition for stimulus dimensions such as frequency in auditory cortex (Wehr and Zador 2003) and orientation in visual cortex (Tan et al. 2011). Co-tuning of excitation and inhibition indicates that the tuning of spiking responses is not actively shaped by inhibition, but rather is is inherited from the tuning of presynaptic excitatory neurons. The simplest scenario for this is that all presynaptic neurons have ILD sensitivity similar to that of the excitatory input. This is consistent with the existence of both EO and PB neurons in subcortical structures such as the inferior colliculus (Fuzessery et al. 1990; Irvine and Gago 1990). However, because our methods measured the summed excitatory input by the neuron, it is also possible that this excitation is pooled across a population of neurons with distinct ILD sensitivity. In the visual cortex, for example, orientation selectivity arises from pooled thalamic inputs that have aligned circularly-symmetric receptive fields (Reid and Alonso 1995). Orientation tuning is further refined by local cortical inhibition (Hirsch and Martinez 2006), suggesting a similar principle of operation as seen in our PB cells, for which ILD sensitivity is partially inherited and is markedly refined by local cortical inhibition.

Role of inhibition in cortical interaural level difference selectivity

The ILD selectivity of PB cells is the result of broad excitatory inputs from midline (ILD = 0 dB) to contralateral (ILDs > 0 dB) stimulus combinations. At the more contralateral stimulus combinations, inhibition reduced or abolished spiking output because it overwhelmed excitation. In a few cases this effect was enhanced by shifts in the relative timing of excitation and inhibition, with inhibition preceding excitation for contralateral ILDs. An effect of the relative timing of inhibition has only been observed in a few cases in the cortex, such as FM sweep selectivity (Zhang et al. 2003), whisker directional selectivity (Wilent and Contreras 2005), and silencing of auditory layer VI cells (Zhou et al. 2010). While only 3/13 PB cells in our sample showed preceding inhibition that suppressed spiking, we never observed this in our EO sample (0/15 cells). Due to our small sample size, we cannot rule out the possibility that EO cells use this strategy, but our results suggest that the relative timing of excitation and inhibition may specifically contribute to PB but not EO response properties in auditory cortex. These results are an important first step towards understanding the role of cortical inhibitory interneurons in sound localization. The direct comparison between synaptic conductances and spiking output in the same cells is central to understanding cortical circuits (Isaacson and Scanziani 2011) but is still rare (Wehr and Zador 2003; Wu et al. 2011). With this approach, we have identified the computation of PB selectivity as an important role for cortical inhibition; but several questions remain about the neuronal sources of these inhibitory inputs. Which class or classes of inhibitory interneurons target PB cells? Do they receive the same or a different set of excitatory inputs than the PB cell they target?

Does the contralaterally-evoked inhibition that converts EO neurons into PB neurons arise from the same or a different set of inhibitory neurons than the centrally-evoked inhibition? Further investigation using molecular-genetic methods for identification and manipulation of these neurons and circuits may help provide answers to these questions.

Comparison to previous studies

It is still not entirely clear whether binaural response properties in cortex fall into discrete classes, as has been widely proposed (e.g. Zhang et al. 2004), or fall along a continuum, as recent work suggests (Campbell et al. 2006). Our findings provide novel insight into this debate, because we have shown that two distinct classes of binaural spiking responses, EO and PB, are produced by distinct synaptic processing strategies. However, it is important to note that because we targeted EO and PB neurons, our sample could be biased towards discrete categories, suggesting that the existence of a continuum should not be ruled out.

Two recent studies showed that cortical responses to binaural sounds in the rat are tuned to contralateral sources. Yao et al. (2013) reported that cells in rat primary auditory cortex are exclusively tuned to contralateral azimuths. Similarly, Chadderton and colleagues (2009) found panoramic synaptic representations of free-field sound sources with half of their sample spiking to contralateral sources and the remainder divided between center and ipsilateral locations. Many of our cells, especially EO cells, received synaptic inputs across all ILDs (see Fig. 6B). However, cells in our PB sample tended to receive contralateral but not ipsilateral synaptic input (see Fig. 8B). The discrepancy between our present work and that of Yao et al. (2013), could be due to a differences between free-field and binaural stimuli. For free field sounds, cortical cells may integrate information from both ILD and the head-related transfer function. Future studies in the rat are necessary to reveal the mechanisms underlying the integration of these two sound localization cues in the cortex.

In future studies, optogenetic silencing may provide a means to directly test the role of auditory cortex in sound localization without the long-term complications of conventional lesion studies. In the pallid bat, local inhibitory blockade in auditory cortex converts PB cells into EO cells, whereas EO cells remain unchanged (Razak and Fuzessery 2010). Our results are consistent with this finding, suggesting that cortical inhibition shapes the spiking output of PB cells. Here, by directly measuring the membrane potential and synaptic excitation and inhibition, we show that inhibition shapes spiking output of PB cells both by overpowering excitation in magnitude and, in some cases, by preceding excitation in time. These results suggest a role for the auditory cortex in processing binaural cues for sound localization. Moreover, our results demonstrate that cortical synaptic processing of binaural cues is not just a specialization in a nocturnal predator, suggesting that this auditory cortical circuit is a general feature of mammalian auditory systems.

Why is binaural selectivity computed at multiple levels of the auditory system?

Binaural cues such as ILD undergo extensive synaptic processing in the auditory brainstem and midbrain (Grothe et al. 2010; Li et al. 2010), and both EO and PB neurons are present in the inferior colliculus (Fuzessery et al. 1990; Irvine and Gago 1990). Why then should PB selectivity be re-computed in auditory cortex, rather than simply inherited from subcortical PB neurons, as with cortical EO neurons? One possibility is that there is a lack of precision in axonal projections from the thalamus into the cortex (Miller et al. 2001). This would require a re-computation of PB selectivity. However, this would not explain why only PB cells and not EO cells require active processing. Another interpretation of our finding is that it underscores the adaptive value of sound localization; some neural computations may be redundant precisely because they are critical to survival of a species over evolutionary time frames. However, cortical re-computation of binaural selectivity might serve a different purpose than subcortical binaural representations. We speculate that cortical synaptic control over binaural selectivity might provide a substrate for modulation by selective attention (Lee and Middlebrooks 2011). The mechanisms by which we can attend to a particular location in space are not well understood, but on-line regulation of the binaural selectivity of cortical neurons by modulation of inhibitory circuitry is an interesting possibility.

CHAPTER IV

CONCLUSION AND FUTURE DIRECTIONS

In this dissertation I investigated how auditory cortical neurons respond to the ILD sound localization cues, and the synaptic mechanisms underlying these spiking responses. In Chapter II, I first demonstrated the novel finding that neurons in the rat auditory cortex are level-dependent. This result is in contrast to previous reports from the primate and bat. In these species, neurons in the auditory cortex are level-invariant in response to the ILD cue. This result is an important contribution to the field of auditory neuroscience because it suggests that not all mammals share the same ILD processing strategies. Stecker and colleagues (2005) proposed that the switch from level-dependence of ILD cues to level-invariance occurs in higher cortical areas such as the the parietal lobes. Another possibility is that level-invariance may be computed in the superior colliculus. This brain region is a likely candidate for integrating sound localization cues, since it is also responsible for coordinating saccadic eye movements, limb movements, and attention. Yet another possible scenario is that rats are not level-invariant in their behavior. While this seems unlikely, this species has comparatively poor sound localization abilities and has yet to be tested behaviorally for level-dependence. Future studies will be necessary to resolve this open and important question.

In Chapter III, I showed direct evidence that neurons in the rat auditory cortex utilize inhibition to shape ILD preferences in PB cells. These cells are unresponsive to monaural sounds but respond robustly when both ears are simultaneously stimulated by sounds of equal loudness. These neurons are candidates for representing sound source locations originating from the midline of the listener. Our data corroborates a recent report using pharmacology in the bat, suggesting that the active shaping of midline sound sources by the cortex is a general feature of mammalian neural circuitry. In that study they used extracellular recordings in a secondary auditory area, the binaural cluster, that contains a high proportion of PB cells (Razak and Fuzessery 2010). They showed that 17/22 PB cells were converted into EO cells when they locally applied Gabazine, a drug that blocks the inhibitory neurotransmitter $GABA_A$. Our result shows a similar scenario, in which PB cells receive far more excitation to contralateral monaural sounds and ILDs than to ipsilateral sounds and ILDs. In these cells inhibition was also minimal in response to ipsilateral monaural and binaural ILDs and was proportional to excitation. However, at contralateral monaural and binaural ILDs, inhibition became disproportionately stronger than excitation which caused a suppression of spiking output.

What is the source of the inhibition shaping the spiking output of PB cells? Current research strongly suggests that the inhibitory inputs acting in cortical circuits are from local inhibitory cells. These cells have short range projections that do not exit the cortical mini-column. One possibility is that excitatory projections from the contralateral auditory cortex synapse onto the inhibitory cells, which in turn cause the suppressive effects we observed for contralateral monaural and binaural ILDs. Another possibility is that parallel pathways from subcortical structures may also be relayed through the MGBv but synapse onto inhibitory cells. The majority of axonal projections exiting the brainstem undergo decussation, crossing the midline causing the well known contralateralization of higher auditory brain regions. However, a small proportion of axonal projections remain on the ipsilateral side. The inferior colliculus receives projections from both the ipsilateral and contralateral superior olivary complexes during further processing of ILD cues (Li et al. 2010). Some of these cells inherit their responses, while others are actively constructed. Since this processing center receives both ipsilateral and contralateral projections from the LSO, it is possible that the same may be true for neurons in the auditory cortex. This could explain why Razak and Fuzessery saw some PB that inherited their response properties while the majority were actively processed. Future experiments utilizing optogenetic silencing of inhibitory cells in the auditory cortex may reveal the types of cells and/or the specific layers of the cortical mini-column involved in the processing of PB cells.

APPENDIX A

NEUROLIGIN1 DRIVES SYNAPTIC AND BEHAVIORAL MATURATION THROUGH INTRACELLULAR INTERACTIONS

Reproduced with permission from Hoy JL, Haeger PA, Constable JRL, Arias RJ, McCallum R, Kyweriga M, Davis L, Schnell E, Wehr M, Castillo PE, Washbourne P. Neuroligin1 drives synaptic and behavioral maturation through intracellular interactions. *J Neurosci* 33: 9364-9384, 2013.

Abstract

In vitro studies suggest that the intracellular C terminus of Neuroligin1 (NL1) could play a central role in the maturation of excitatory synapses. However, it is unknown how this activity affects synapses *in vivo,* and whether it may impact the development of complex behaviors. To determine how NL1 influences the state of glutamatergic synapses *in vivo,* we compared the synaptic and behavioral phenotypes of mice overexpressing a full-length version of NL1 (NL1FL) with mice overexpressing a version missing part of the intracellular domain (NL1ΔC). We show that overexpression of full-length NL1 yielded an increase in the proportion of synapses with mature characteristics and impaired learning and flexibility. In contrast, the overexpression of NL1ΔC increased the number of excitatory postsynaptic structures and led to enhanced flexibility in mnemonic and social behaviors. Transient overexpression of NL1FL revealed that elevated levels are not necessary to maintain synaptic and behavioral states altered earlier in

development. In contrast, overexpression of NL1FL in the fully mature adult was able to impair normal learning behavior after 1 month of expression. These results provide the first evidence that NL1 significantly impacts key developmental processes that permanently shape circuit function and behavior, as well as the function of fully developed neural circuits. Overall, these manipulations of NL1 function illuminate the significance of NL1 intracellular signaling *in vivo,* and enhance our understanding of the factors that gate the maturation of glutamatergic synapses and complex behavior. This has significant implications for our ability to address disorders such as autism spectrum disorders.

Introduction

It is hypothesized that neurodevelopmental disorders such as autism spectrum disorders (ASD) could be a consequence of disrupting specific aspects of synapse formation or maturation (Bourgeron 2009; Penzes et al. 2011; Zoghbi 2003). Molecules known as synaptogenic cell adhesion molecules (CAMs) powerfully regulate these processes and have been repeatedly linked to the etiology of ASD (Gilman et al. 2011). However, few studies explore how targeted perturbations of CAMs affect synaptic state across development to modulate behaviors impacted in neurodevelopmental disorders. Recent genetic association studies have linked copy number variation, null and gain of function mutations in one particular family of CAMs, the Neuroligins, to ASD (Comoletti et al. 2004; Glessner et al. 2009; Jamain et al. 2003; Philippe et al. 1999; Shao et al. 2002; Zhiling et al. 2008). Alterations of Neuroligin1 (NL1) levels in mice also alter memory in adult animals (Dahlhaus et al. 2010; Jung et al. 2010; Kim et al. 2008), while NL1 deletion impacts both learning and normal social interactions (Blundell et al. 2010). As changes in social behavior are a core diagnostic criteria in human cases of ASD, and heterogeneous alterations in learning and memory behavior are comorbid with the disorder (Amaral et al. 2008; Lord et al. 2000; Pardo and Eberhart 2007), NL1 manipulation has been validated to impact behavioral domains in mice homologous to those impacted in ASD. This suggests that detailed studies of how, when, and where the CAM NL1 impacts synaptic state and behavior will facilitate our ability to understand the etiology of ASD.

However, it is unclear which molecular mechanisms regulated by NL1 are relevant to the occurrence of behavioral changes characteristic of neurodevelopmental disorders. NL1 plays a prominent role in activity-dependent synaptic maturation *in vitro* (Chubykin et al. 2007; Wittenmayer et al. 2009), as well as altering synapse number (Burton et al. 2012; Sara et al. 2005; Shipman and Nicoll 2012). *In vitro* studies implicate NL1's intracellular PDZ and WW binding domains in facilitating its maturational activities (Barrow et al. 2009; Chih et al. 2005; Iida et al. 2004; Meyer et al. 2004; Tallafuss et al. 2010), while at least one other study proposes that a novel intracellular region drives synapse formation (Shipman et al. 2011). Other recent studies now provide compelling evidence that NL1's extracellular domain is sufficient for its posited role in glutamate receptor recruitment and influencing synapse number (Budreck et al. 2013; Shipman and Nicoll 2012). A lack of understanding about when, where, and how these mechanisms yield reliable changes in behavior over development limits our ability to predict how specific perturbations in NL function lead to disease states.

Here, we address this gap through phenotypic analysis of targeted NL1 overexpression, a genetic perturbation specifically linked to human cases of ASD. Furthermore, we compared the synaptic and behavioral phenotypes of mice overexpressing the full-length version of NL1 (hemagglutinin (HA)-NL1FL) to a version missing the terminal 55 aa (HA-NL1ΔC) to determine which molecular mechanisms exerted by NL1 overexpression impact behavior. We found changes in spine morphology and synaptic protein content that were consistent with inducing a large-scale maturation of synapses in HA-NL1FL animals. This corresponded to deficits in learning and behavioral flexibility in the same mice. In contrast, these aspects of synaptic maturation could not be induced by overexpression of HA-NL1ΔC in mice; instead, we observed an increase in synapse number and retention of a distinct set of scaffolding molecules. These changes corresponded to more flexible behavior in complex tasks. Finally, we demonstrate that transient HA-NL1FL overexpression in juveniles led to persistent changes in synaptic state and behavior in adults where overexpression had been eliminated for 1 month. Overexpression in the fully mature adult was also able to impair normal learning behavior. These results provide the first evidence that NL1 significantly impacts developmental processes that permanently shape circuit function and behavior, as well as the function of fully developed neural circuits.

Materials and Methods

All studies were conducted with approved protocols from the University of Oregon and the Albert Einstein College of Medicine Institutional Animal Care and Use Committees, in compliance with National Institutes of Health guidelines for the care and use of experimental animals.

Transgenic mouse generation

The green fluorescent protein (GFP) within the GFP-NL1FL construct (Fu et al. 2003) was replaced with an HA epitope tag sequence via PCR. HA-NL1FL was then removed from pCDNA3 vector and inserted into the pTRE-tight vector (Clontech) using serial digests of HindIII and XhoI followed by HindIII and XbaI. The TetO-HA-NL1FL was linearized and cut from the pTRE-tight vector with XhoI and injected into embryos. TetO-HA-NL1ΔC was similarly created except that the last 55 aa were deleted via PCR with the following reverse primer (NL1-ΔC: ggtctcgagctacctcctcatagcaagagtataatctggg). Constructs were confirmed with sequencing and successful transgenesis was confirmed via genomic PCR and Western blot of forebrain homogenate for the HA tag.

All single transgenic mice (TetO-HA-NL1ΔC$^{+/-}$ or TetO-HA-NL1FL$^{+/-}$) as well as double transgenic mice (CaMKIIα-tTA$^{+/-}$; TetO-HA-NL1ΔC$^{+/-}$ or CaMKIIα-tTA$^{+/-}$; TetO-HA-NL1FL$^{+/-}$) were first examined for basic health and behavior according to standard methods (Moy et al. 2004). It was important to consider that the insertion of novel transgenes could lead to deleterious mutations at the insertion site and result in biological effects unrelated to the specifics of transgene expression. Based on the following five observations, we are confident that all effects reported are specifically due to NL1 transgene expression and function. (1) No overt changes in health, reproduction, and reflexive behavior were observed in any single positive transgenic line. (2) The TetO-HA-NL1$^{+/-}$ and TetO-HA-NL1ΔC$^{+/-}$ transgenes are never present in the homozygous state. Thus, any functional consequences of TetO transgene integration would have to be due to haplo-insufficiency. The possibility of haplo-insufficiency explaining our results is excluded as all control animals were the single positive littermates: TetO-HA-NL1FL$^{+/-}$, TetO-HA-NL1ΔC$^{+/-}$, or CaMKII-tTA$^{+/-}$. Further, water maze data analysis comparing single positive TetO-HA-NL1FL$^{+/-}$ transgenics (n=5) to single positive CaMKIIα-tTA$^{+/-}$ transgenics (n = 5) from the same litter revealed that the time spent in the target quadrant ($p = 0.186$) distance to platform ($p = 0.453$) and number of crosses ($p = 0.934$) were statistically indistinguishable between single transgenic control groups. This was also true for TetO-HA-NL1ΔC$^{+/-}$ versus CaMKIIα-tTA$^{+/-}$ mice (p = 0.864, $p = 0.358$ and $p = 0.691$, $n = 6$ in each group). This result allowed us to pool both types of single positive animals (TetO and CaMKIIα-tTA) as a single control group for the remainder of our studies. (3) The immunohistochemical effects of both transgenes are largely confined to the SLM of the CA1 region of the hippocampus, the region in which the two transgenic proteins are predominantly localized (see Fig. 1C,D). (4) Key immunohistochemistry experiments using double positive transgenics continually on Dox revealed that there were no changes in Shank levels in the CaMKII-tTA$^{+/-}$; TetO-HA-NL1FL$^{+/-}$ mice on Dox compared with single transgenics on Dox (Intensity: 94.8 ± 10.7% vs 100 ± 8%, respectively, $p > 0.05$, Area: 90.6 ± 11.2% vs 100 ± 15.9%, $p > 0.05$, $n = 4$ animals in each group). Similarly, NR2B staining characteristics in the SLM of CaMKII-tTA$^{+/-}$; TetO-HA-NL1ΔC$^{+/-}$ double positive mice on Dox were the same as those with either the TetO-HA-NL1ΔC$^{+/-}$ transgene or the CaMKII-tTA$^{+/-}$ transgene on Dox (Intensity: 90 ± 12.1% vs 100 ± 15.1%, respectively, $p > 0.05$, Area: 114.2 ± 12.6% vs 100 ± 7.8%, $p > 0.05$, $n = 4$ animals in each group). (5) CaMKII-tTA$^{+/-}$; TetO-HA-NL1FL$^{+/-}$ mice, i.e., “double positive,” mice that were administered doxycycline from birth, and therefore did not express the transgene as a protein but did have both transgenes in the genome at the times of initial testing, did not show any deficits in learning and memory behavior (see Fig. 8C, Late OEs, Test 1 and Test 2) or spine size (Fig. 8E). These observations rule out the possibility that genetic disruptions by transgene insertion account for the phenotypes described in this study, but that such effects are related to expression of the proteins of interest.

Immunocytochemistry, microscopy, and image processing.

The brains from four animals of each genotype were removed immediately after death and flash frozen with liquid nitrogen. Brains were stored at -80°C for up to 3 weeks and then cryosectioned. Sections (10 μm thick) were air dried on slides, fixed with 4% paraformaldehyde (PFA) solution in PBS (1xPBS) for 30 min at 4°C, and washed three times in 1xPBS with gentle agitation. Antigen retrieval was performed with a 0.05% trypsin treatment for 5 min at room temperature. One percent Roche Block (Roche) and 10% normal goat sera in 1xPBS was applied for 1 h at room temperature to block nonspecific staining. Sections were incubated overnight at 4°C in the following primaries diluted in blocking solution: αHA (1:500, purified mouse IgG1; Covance), αPSD95 (1:400, mouse IgG2a 28/43; NeuroMab), Synapsin1 (1:400, rabbit polyclonal; Millipore), pan-SHANK (1:400, mouse IgG1 N23B/49; NeuroMab), and NR2B (1:300, mouse IgG2a N59/20; NeuroMab). Sections were washed three times for 5 min in 1x PBS at room temperature with gentle agitation before applying Alexa Fluor dye-labeled secondary antibodies (1:500, goat; Invitrogen) for 2 h at room temperature. Slides were washed and mounted in Fluoromount G+DAPI (SouthernBiotech).

Images were taken on an inverted Nikon TU-2000 microscope with an EZ-C1 confocal system (Nikon) using either a 10x air or 100x oil-immersion objective (1.45 NA). Slides were blinded to genotype. A scan at low magnification was used to determine the brightest section stained for each antibody. Laser intensities, gain, and offset ceilings were normalized to the brightest section, with saturation set to levels just above the brightest puncta of that slide. Subsequently, we confirmed that specifically stained puncta in each channel imaged were detectable in all samples. Intensity and average measures were made using Image Pro Plus (Media Cybernetics). Briefly, three 100 μm^2 regions within each hippocampal area per section were selected for analysis. Puncta were automatically thresholded and selected with the automatic bright objects feature. Measures of mean intensity and area were recorded for each punctum and average densities of puncta per 100 μm^2 were calculated. The process was repeated for 2–3 separate sections from 2–3 slides for each mouse analyzed to control for slide treatment and tissue penetration variability. Three to four mice of each genotype were analyzed in each condition constituting at least three independent experiments. The puncta analyzed additionally met the criteria of being segregated regions of intensity that were at least two SDs more intense than diffuse background regions and between 0.8 and 4 μm^2. Staining in CA1 stratum radiatum (SR), stratum lacunosum moleculare (SLM), and the molecular layer of CA3 were measured. Group means were compared and statistical significance was determined using the Student's *t* test with α level set at 0.05.

Synaptosomal preparations and Western blotting.

The hippocampal formation, including the subiculum, was dissected and homogenized in 1.5 ml of buffer [(4 mM HEPES, 320 mM sucrose, protease inhibitor tablets (Roche), pH 7.4] using a Potter–Elvehjem tissue grinder (Huttner et al. 1983). Homogenate was centrifuged for 10 min at 850 x *g,* the supernatant was removed and centrifuged at 12,000 x *g* for an additional 10 min. Pellet was resuspended in 2 ml of buffer and centrifuged for 10 min at 14,000 x *g.* The final pellet was resuspended in 500 µl of buffer. Protein concentration was determined using the Bio-Rad DC Protein Assay kit. Samples were diluted in sample buffer (312 mM Tris-HCl, pH 6.8, 50% glycerol, 10% SDS, 0.05 bromophenol blue, and 25% β-mercaptoethanol) to a final concentration of 0.3 µg/µl. A total of 3 µg was loaded onto an SDS-PAGE gel, with samples from four to five animals per genotype, transferred to nitrocellulose membranes, and probed with the following antibodies at a dilution of 1:1000: αPSD95 (mouse IgG2a 28/43; NeuroMab), αSynapsin1 (rabbit polyclonal; Millipore), αNR1 (mouse IgG1; BD PharMingen), αNR2B (mouse IgG2a N59/20; NeuroMab), αNR2A (rabbit; Abcam), αNeuroligin1 (mouse IgG1 N97A/31; NeuroMab), αNeuroligin1 (mouse IgG1 4C12;

Synaptic Systems), αHA (rabbit; Bethyl Laboratories), αActin (mouse IgG2; Millipore), αGephyrin (mouse IgG1; Synaptic Systems), αGluR1 (rabbit; Abcam), αGluR2 (mouse IgG2a; Millipore), αPanShank (mouse IgG1 N23B/49; NeuroMab), αPick1 (mouse IgG1 L20/8; NeuroMab), αSAP97 (mouse IgG1 K64/15; NeuroMab), and αSAP102 (mouse IgG1 N19/2; NeuroMab).

For immunoprecipitation experiments cortices and hippocampi were dissected and homogenized in 50 mM HEPES, pH 7.4, 0.1 mM EGTA, 100 mM NaCl, and protease inhibitors leupeptin, pepstatin TLCK, and PMSF. Triton X-100 was added to a final concentration of 1% and incubated for 2 h at 4°C. Insoluble material was removed by centrifugation at 100,000 x *g* for 1 h. The homogenate was then adjusted to 2 mM $MgCl_2$ and 2 mM $CaCl_2$ and incubated with mouse anti-HA (HA.11; Covance) and incubated overnight at 4°C. Protein G Sepharose beads (100 µl) were added for 1 h at 4°C. The beads were washed three times in homogenization buffer with 1% Triton X-100 and the bound protein submitted to SDS-PAGE and immunoblotting using rabbit anti-pan-NRX1 (ABN161; Millipore). All Western blots were quantified using Image Pro Plus and intensity was expressed as percentage of control. Statistical analysis was performed using Student's *t* test with α level set at 0.05.

Behavior

Basic reflex and health assessment follows (Moy et al. 2004). Briefly, mice were screened for weight differences, coat condition, abnormal tooth length, reproductive capability, gross visual functions such as forepaw reaching toward a distant object, and basic motor capabilities such as climbing rates and clinging times to an inverted wire cage lid.

Morris water maze

The Morris water maze task was based on the standard methods for spatial learning in rodents (Vorhees and Williams 2006). Each transgenic cohort consisted of 10 double positive male mice and 10 control males positive for either the CaMKII-tTA$^{+/-}$ transgene or one of the TetO-driven transgenes. In the juvenile analysis, eight juvenile males and eight adult males from the same parents were compared. Briefly, the mice were tested for their ability to find an escape platform (diameter = 12 cm) on four different components of the task in the following order: (1) a 2 d visible platform acquisition, (2) a 7 d hidden (submerged) platform acquisition phase with the target moved to a different location, (3) a subsequent probe trial in the absence of the platform, and (4) hidden platform training in a new location (reversal training). In the visible platform test, each animal was given four trials per day across 2 d to swim to an escape platform cued by a textured cylinder extending above the surface of the water. For each trial, the mouse was placed in the pool at one of four possible locations (randomly ordered) and then given 60 s to find the cued platform. Once on the platform, even if placed there, they remained for at least 10 s. Measures were taken of latency to find the platform, swimming distance, and swimming velocity via Image Pro Plus's automated tracking system and custom MATLAB programs. Following visual training, mice were trained on the hidden platform test. At day 8, mice were given a 1 min probe trial in the pool with the platform removed.

On day 9 mice were tested for reversal learning using the same procedure but with the target moved to the opposite quadrant. All data were analyzed with repeated-measures ANOVA (RMANOVA), followed by Tukey–Kramer HSD *post hoc* test to compare means of interest, α level set at 0.05.

Object recognition

The experiment was performed as described by (Bevins and Besheer 2006). Briefly, mice were individually habituated to an open-field round container (30 cm in diameter x 30 cm in height) for 15 min. The training session followed the habituation session by 10 min. During the training session, two novel objects were placed in the open field, and the animal was allowed to explore for 20 min. All trials were recorded by video, and measures of time spent exploring each object, time to first make contact with an object, percent of thigmotaxis, and which object was first approached were scored. Criteria for active exploration included sniffing, touching, and whisking the objects. After a delay from initial exploration of 1 h, the animal was placed back into the same box in which one of the familiar objects during training was replaced by a novel object and allowed to explore freely for 15 min. A preference index, a ratio of the time spent exploring the novel object (retention session) over the total time spent exploring both objects, was used to measure recognition memory. Data were calculated as mean ± SEM. Significant differences from chance performance were determined by Wilcoxon signed rank test, with α level of 0.05. Chance performance was assumed to be 50% time at each object.

Three-chambered social preference test

This test was performed as described by Moy et al. (2004). The test was performed in three phases: habituation, sociability, and preference for social novelty. During habituation the test mouse was first placed in the middle chamber and allowed to explore for 10 min, with the doorways into the two side chambers open. Each of the two sides contained an empty wire cage. The wire cages were 11 cm in height, with a bottom diameter of 10.5 cm. A weight was placed on the top of each cage to prevent movement. Wire cages were cleaned with EtOH between trials and washed thoroughly at the end of each testing day. To measure sociability, after the habituation period, the test mouse was enclosed in the center compartment of the social test box, and an unfamiliar mouse (a group housed "stranger" mouse), was placed in one of the wire cages of the side chambers chosen semi-randomly. This ensured a mixture of right and left locations were tested within each group and accounted for potential biases in side preference. After the stranger mouse was in place, the test mouse was allowed to explore the entire social test box for a 10 min session. Sessions were recorded by video and scored by two blinded and trained observers. Number of approaches of stranger and object were scored. Total time and track distribution within each chamber was calculated using Image Pro Plus, and percentage of time spent near either cup was the metric displayed in Figure 6. To measure preference for social novelty, immediately following the sociability test, each mouse was tested in a third 10 min session with a choice of the familiar stranger versus a novel group housed stranger mouse of the same strain, age, and sex. The same measures as mentioned above were calculated and social novelty preference could be calculated by comparing time differences in the interactions with the familiar and novel mouse. Significance was determined by repeated-measures ANOVA and the α level set at 0.05.

Social dominance tube test

The dominance tube apparatus (Messeri et al. 1975) was constructed out of Plexiglas and consisted of a 36 cm long tube with a diameter of 3.5 cm attached on either end to a start cylinder (measuring 10 cm in diameter). At the center of the tube was a removable perforated partition that allowed for olfactory investigation, but not physical contact. A singly housed experimental mouse and an unfamiliar group-housed mouse of similar age, weight, and sex were placed in opposite start boxes and allowed to habituate to the apparatus for 10 min. When the animals met in the middle of the tube after the habituation period the center partition was lifted. The test was video recorded and concluded once one mouse had forced the other back. In the event of a tie, where the mice managed to squeeze past each other, the trial was noted but not included in the comparison statistics. Each mouse was subjected to three to four bouts with the same partner. Dominance behavior was measured over three separate trials for each mouse as compared with three different age and sex matched strangers. Start sides were randomized. Significance was determined by repeated-measures ANOVA with α level set at 0.05 and Tukey's *post hoc* test to report significant differences in mean performances.

Resident intruder test

Mice were housed individually for 7– 8 d before an unfamiliar group-housed control mouse of the same sex and comparable weight was introduced to the resident's home cage. Food was removed 1 h before testing and all mice were habituated to the testing room for 1 h before introduction of the intruder mouse. Behavior was monitored and video recorded for the first 10 min after introduction of the intruder, or until an attack occurred, whichever came first. Measures of attack frequency, attack latency, dominant mounting, investigatory sniffing (sniffing directed toward the partner), chasing, and grooming were recorded as described previously (Duncan et al. 2004). All measures were scored by two blinded observers and the total scores between the two observers were averaged. Animals were subject to three rounds of intruder presentation. Significance was determined by repeated measures ANOVA and the α level set at 0.05.

Spine density and morphology quantification

Brains from three animals of each genotype were sectioned immediately after being killed by isoflurane followed by decapitation. Coronal sections (150 µm thick) were cut at room temperature on a vibratome and placed into 2% PFA for 30 min. Sections were then placed on slides and covered in 1xPBS. DiI crystals (Sigma-Aldrich) were sparsely inserted into stratum oriens (SO) of region CA1 in the dorsal hippocampus. Tissue was monitored for distribution of DiI labeling between 1 and 2 d. Four to five serial sections containing both hemispheres from each animal were labeled with DiI. Twelve well-isolated dendrites from both proximal SR, and SLM were imaged at 100x magnification using a Nikon C1 confocal microscope (see above) and quantified. Dendrites were selected for analysis on the basis of the following: (1) location within the hippocampal stratum, (2) isolation from neighboring neurites, (3) clarity of spine labeling, (4) close proximity to tissue surface to minimize light scattering, (5) low frequency of regularly spaced varicosities ~2 µm in diameter, and (6) validation that the neurite came from a CA1 pyramidal neuron. Regions of interest within each layer were chosen based on their distance between flanking anatomical regions, which are easily identifiable in labeled tissue. Regions >10 µm from their flanking anatomical borders were chosen to facilitate analyzing structures near the middle of each layer. Results were averaged across three animals for each genotype, yielding a total of 36 individual dendrites analyzed per hippocampal layer, per genotype. Composite images were created from 10- to 20-µm-thick *z-stacks* taken at 0.2 µm increments with a small pinhole. Spine density, number of spines per 10 µm dendrite, and spine head area were measured using ImageJ. Before outlining spines for analysis, images were converted to 8-bit grayscale, deconvolved, and thresholded until individual spines were clearly dissociable. Spine head area in control animals within CA1 SLM ranged from ~0 0.1 to 0.78 µm^2, closely resembling measures reported in other studies of spine head size in SLM.

Slice electrophysiology

Animals were deeply anesthetized with isoflurane, decapitated, and the brain was rapidly removed. Transverse hippocampal slices (400 µm thick) were prepared from 4- to 9-month-old C57BL mice on a VT 1200S slicer (Leica Microsystems) in ice-cold cutting solution containing the following (in mM): 215 sucrose, 2.5 KCl, 20 glucose, 26 $NaHCO_3$, 1.6 NaH_2PO_4, 1 $CaCl_2$, and 4 $MgCl_2$. This solution was slowly exchanged to the artificial CSF (ACSF) containing 124 NaCl, 2.5 KCl, 10 glucose, 26 $NaHCO_3$, 1.6 NaH_2PO_4, 2.5 $CaCl_2$, and 1.3 $MgCl_2$. Both cutting and ACSF solutions were saturated with 95% O_2 and 5% CO_2, pH 7.4. The slices were incubated at room temperature for at least 1.5 h before recording.

Slices were transferred to a recording chamber and perfused with ACSF (2 ml/min). All recordings were done at 30°C and the CA3 region was separated from the slices by a single diagonal cut. CA1 pyramidal cells were voltage clamped at – 60 or +30 mV using patch-type pipette electrodes (~3–4 MΩ) containing the following: (in mM): 123 cesium gluconate, 8 NaCl, 1 $CaCl_2$, 10 EGTA, 10 HEPES, and 10 glucose, pH 7.3 (290 – 295 mOsm), and connected to a Multiclamp 700A amplifier (Molecular Devices). The series resistance (Rs), typically 8 –15 MΩ, was monitored throughout the recording using -5 mV, 80 ms voltage steps, and those experiments in which there was a >10% change in *Rs* were excluded for analysis. Pipettes were pulled on a PP-830 vertical puller (Narishige). EPSCs were evoked by monopolar stimulation with a broken patch pipette (~10 µm tip) and filled with ACSF. The stimulation pipettes were placed in SR (~100 µm from CA1 pyramidal cell body) and in SLM (~350 µm from CA1 pyramidal cell body). NMDAR/AMPAR ratios were determined as follows: for AMPAR-EPSCs, cells were voltage clamped at -60 mV, and recordings were performed in the presence of the $GABA_A$ receptor antagonist picrotoxin (100 µM). Due to the inward rectification of the PP-CA1 NMDAR-EPSC (Otmakhova et al. 2002), NMDAR-EPSCs were also measured at -60 mV and isolated by adding the AMPAR and kainate receptor antagonist NBQX (10 μM). The baseline stimulation frequency for all experiments was 0.05 Hz. Averaged traces include at least 15 successive synaptic responses. Paired-pulse facilitation was analyzed dividing the second pulse by the first pulse amplitude with a 40 or 50 ms interstimulus interval in SR or SLM, respectively. NMDAR-EPSC decay kinetics was analyzed by clamping to +30 mV and fitting a single exponential using Origin 8.6 (OriginLab). EPSCs were elicited at 20 s intervals, filtered at 2.2 kHz, and acquired at 5 kHz using custom software written in Igor Pro 4.09A (Wavemetrics). Field potentials were recorded extracellularly with patch-type pipettes filled with 1 M NaCl and placed in the SLM. The functional contribution of NR2B-containing NMDARs was assessed by monitoring NMDAR-fEPSPs in the presence of NBQX (10 μM) and picrotoxin (100 μM).

Long-term potentiation at the PP-CA1 synapse (PP LTP) was measured in acute slices perfused with picrotoxin (100 μM) and CGP-55845 (3 μM) to block $GABA_A$ and $GABA_B$ receptors, respectively. Two independent pathways were alternately stimulated at 15 s intervals; one pathway received the LTP induction protocol whereas the other (naive) pathway served as control. PP LTP was induced with a theta-burst stimulation (TBS) protocol consisting of four theta-burst trains of stimuli once every 10 s. Each theta-burst train consisted of 10 bursts every 200 ms, each burst containing 5 stimuli at 100 Hz. Student's *t* test was used to determine statistical significance, with $^{*}p < 0.05$, $^{**}p < 0.01$, and $^{***}p < 0.01$. All statistics and analyses were performed with OriginPro 8.6. All data are presented as mean ± SEM.

Auditory cortex electrophysiology.

Briefly, each mouse was anesthetized with a ketamine (100 mg/kg body mass), medetomidine, and acepromazine mixture, and given supplemental doses to maintain anesthesia. Atropine and dexamethasone were also administered to reduce tracheal secretions and cerebral edema. The mouse's temperature was maintained at 37 ± 1°C. The left temporal cortex was surgically exposed (craniotomy and durotomy) and covered with 1.5% agarose in 0.9% saline. Tungsten electrodes, with 1–2 MΩ impedances were used to find cortical regions with strong multiunit responses to click trains, determined audio-visually. White noise clicks were presented at 30–80 dB sound pressure level (SPL), for 25 ms in duration with interstimulus intervals of 500 ms or 1000 ms. Each mouse had one to four recording sites in layer 3–5 of auditory cortex (mean depth: 419 µm; range: 314 – 580 µm; $n = 21$). The rate level function measures neural spike counts driven by increasing sound amplitude in dB SPL for white noise clicks. The number of spikes was summed from a 50 ms window, beginning at the stimulus onset using a spike detection threshold of 3 SD over 40 trials. Subjects: five control male mice with 11 recording sites (range of 1– 4) and five double positive male mice with 10 recording sites (range of 1–3) were used for these experiments. Significance was determined with repeated-measures ANOVA with the α level set at 0.05.

Doxycycline regulation of NL1 overexpression

The HA-NL1FL construct contained the Tet-off responsive genetic element and was there-fore silenced in the presence of the tetracycline analog, Doxycycline (Dox).

The Early Overexpresser (Early OE) cohort was left on a normal diet until 2 months of age, thus expressing their transgene until they were adults. They were fed a diet containing 2 g/kg Dox for 5 d to induce a rapid silencing of transgene expression. That diet was replaced with a 50 mg/kg concentration to maintain transgene suppression for the remainder of the animal's lives. Western blots on a random subset of animals from this cohort confirmed the absence of transgene expression after 7 d of Dox administration (5 d on 2 g/kg Dox diet, 2 d on the 40 mg/kg diet). The mothers of postnatal 10 (P10) pups of the Late Overexpresser (Late OE) cohort were given a diet of 2 g/kg Dox for 5 d and then transitioned onto the 50 mg/kg Dox until weaning. The Late OE pups were weaned onto 40 mg/kg Dox until 2 months of age, thus not expressing the transgene until 2 months of age. The cohort remained on a regular diet for the remainder of their lives, ~1 month. Half of each brain from each subject was used in Western blot analysis to assay for transgene expression. The other half of the brain from each animal was used for DiI spine morphology analysis.

Results

Generation of HA-NL1FL and HA-NL1ΔC transgenic mice

The intracellular C terminus of NL1 contains both PDZ binding and WW binding motifs, which are thought to underlie important aspects of glutamatergic postsynaptic development and brain function. To understand the contribution of these signaling domains to NL1's influence over behavioral and synaptic maturation within known mnemonic neural systems *in vivo,* we used a temporally regulated genetic system to target our manipulations to the forebrain. We generated mice that express the coding region for either NL1 full-length (NL1FL) or NL1 missing the terminal 55 aa (NL1ΔC) under the promoter that is induced by the tetracycline transactivator protein (tTA). Both versions of NL1 were tagged with the HA peptide sequence on the N terminus to facilitate localization and quantification of transgene expression *in situ* (HA-NL1FL and HA-NL1ΔC; Fig. 1A). After generation of founder groups, mice were backcrossed to the C57BL/6J strain of mice before being crossed to mice that expressed the tetracycline transactivator driven by the CaMKIIα promoter, CaMKII-tTA$^{+/-}$ mice. This system drives tetracycline-regulated expression in forebrain excitatory neurons (Mayford et al. 1996). Double transgenic progeny from these crosses, either CaMKII-tTA$^{+/-}$; TetO-HA-NL1FL$^{+/-}$ (HA-NL1FL mice) or CaMKII-tTA$^{+/-}$; TetO-HA-NL1ΔC$^{+/-}$ (HA-NL1ΔC mice) were obtained at the expected Mendelian frequencies in both cases and Western blot analysis revealed that doxycycline administration, 2 g/kg followed by 40 mg/kg in mother's food, from birth was effective in suppressing transgene protein expression (Fig. 8A'; data not shown). At 2 months of age, continuously expressing double positives from both lines were examined for their coat condition, exploratory behavior in an open field, anxiety in the elevated plus maze, ability to climb a pole, and ability to maintain grip when clinging to a cage lid. We also screened for the presence of normal acoustic startle reflexes, average weight, and incidence of mortality before testing in more complicated behavioral assays (Moy et al. 2006; Moy et al. 2004). In these and all subsequent assays except where stated, control groups were composed of an equal mixture of single positives possessing the CaMKII-tTA$^{+/-}$, TetO-HA-NL1FL$^{+/-}$ or TetO-HA-NL1ΔC$^{+/-}$ transgenes

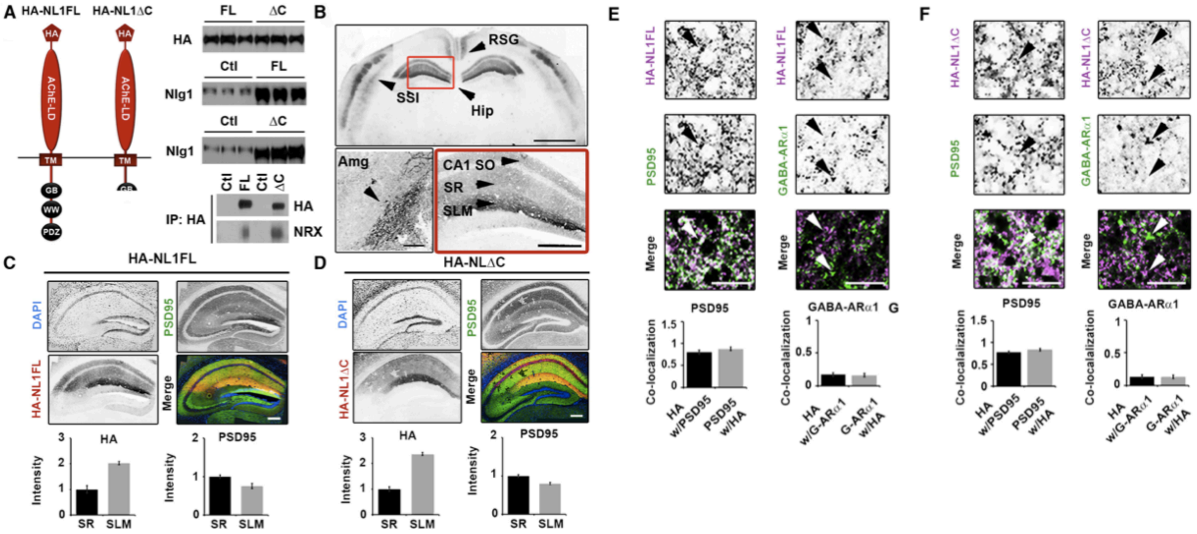

Figure 1. Expression of HA-NL1FL and HA-NL1ΔC in transgenic mice. ***A,*** Left, Schematic of the protein structure of HA-NL1FL and HA-NL1ΔC encoded by the constructs that were used to generate transgenic mice. Right, Absolute levels of HA compared between HA-NL1FL mice and HA-NL1ΔC mice (top), NL1 levels compared between transgenics and their controls (middle). Five micrograms of total protein loaded into each lane. Immunoprecipitation (IP) using antibodies to HA and immunoblotting for Neurexins 1, 2, and 3 reveals similar level of interaction with HA-NL1FL (FL) and HA-NL1ΔC (p = 0.37, *n* = 2 independent IPs). HA, hemagglutinin epitope tag; TM, transmembrane domain; GB, gephyrin binding motif; WW, WW binding domain; PDZ, PDZ type II binding domain; Ctl, control. ***B,*** Immunolabeling of HA shows localization patterns of the HA-NL1 constructs. Top, RSG, layers II/III and V of somatosensory cortex (SS1) and the hippocampus (Hip), arrowheads. Scale bar, 2 mm. Lower left, Expression in the lateral amygdala (Amg), arrowhead. Scale bar, 300 µm. Lower right, Expression in specific strata of the hippocampus, arrowheads, SO, SR, and SLM. Scale bar, 200 µm. Dark areas reflect positive labeling. Sections analyzed were between -1.58 and -2.30 mm bregma. ***C, D,*** Immunolabeling of PSD-95 (green), DAPI (blue), and HA epitope tag (red) for HA-NL1FL (C) and HA-NL1ΔC (D). Scale bar, 200 µm. Quantification of both HA and PSD-95 intensity levels between SLM and SR. All intensities normalized to SR levels. ***E, F,*** Higher magnification and quantification of colocalization between HA and markers of excitatory (PSD- 95) versus inhibitory (GABA-ARα1) synaptic markers, HA-NL1FL mice (E) and HA-NL1ΔC mice (F). Differences in colocalization patterns in all cases were not significant. All data shown are mean ± SEM, significance determined by Student's *t* test, *n* = 3 paired littermates per test (3 double positives compared with 3 littermates of mixed single transgenic backgrounds).

only. In addition, normal fertility rates and the ability to successfully breed suggested preserved olfactory-mediated behaviors, consistent with the findings in subsequent behavioral assays. As no significant differences in all of these measures were found (data not shown), we proceeded to more detailed biochemical, electrophysiological, and behavioral testing.

To effectively compare and contrast the synaptic and behavioral profiles between the two lines of mice, we assayed expression levels of total HA in the hippocampus between the two lines, as well as how much NL1 was overexpressed relative to endogenous control levels via quantitative Western blot. We found no significant difference in amount of HA protein present per 5 μg of forebrain homogenate (100 ± 5.23% HA in HA-NL1FL mice vs 102.96 ± 1.55% HA in HA-NL1ΔC mice, normalized to HA-NL1FL levels, $p > 0.05$; Fig. 1A, right, top). Moreover, blots using an antibody that recognized endogenous NL1 as well as the overexpressed forms revealed each transgenic line overexpressed their respective transgenes similarly relative to single positive littermate controls (207.73 ± 3.45% overexpression HA-NL1FL mice vs 219.33 ± 2.9% overexpression in HA-NL1ΔC mice; Fig. 1A, right, middle). Furthermore, immunoprecipitation of the tagged constructs revealed that the samples from each line similarly coimmunoprecipitated the *trans-synaptic* binding partner Neurexin *in vivo* (Fig. 1A, bottom, right). This argues that both transgenes, the FL and the truncated form, were correctly targeted to the synaptic density and engaged in key *trans-synaptic* interactions. Immunohistochemistry on cryosectioned tissue found comparable expression levels of the transgenes in the same cell types within both transgenic lines (Fig. 1B–D). HA immunolabeling was detected in a subset of the expected forebrain nuclei and neural circuits, based on the CaMKIIα-tTA driver line. This included the amygdala (Amg) and specific cell populations within the neocortex such as the retrosplenial granular (RSG) formation and layers IV and VI of the primary sensory cortices (Fig. 1B). Neither transgene was detected in the striatum (data not shown). Importantly, HA expression in both lines of mice was observed within the hippocampal circuit, the system primarily associated with the explicit forms of learning and memory behaviors previously shown to rely on NL1 function (Blundell et al. 2010; Dahlhaus et al. 2010) (Fig. 1B, red box). Expression was observed throughout CA1, absent from region CA3, and was weak and sparsely found in dentate gyrus (Fig. 1C,D). Accordingly, HA immunoreactivity was localized within the hippocampal circuit to the SO, SR, and SLM of CA1. This suggests targeting of the overexpressed proteins to relevant dendritic structures, as expected for NL proteins.

Surprisingly, we noticed an ~2-fold increase in levels of HA-NL1FL and HA-NL1ΔC in the SLM relative to the SR (SLM:SR intensity ratio 2.1 ± 0.3 vs 2.5 ± 0.4, HA-NL1FL and HA-NL1ΔC respectively, $p > 0.05$; Fig. 1B, lower right,C,D). This relative increase in HA levels in the SLM versus the SR does not parallel the relative intensity levels of PSD-95 between SLM and SR (SLM:SR ratio of PSD-95: 0.75 ± 0.04 vs 0.80 ± 0.04 respectively, $p > 0.05$; Fig. 1C, D), thus synapse density cannot account for the difference in HA levels between these two strata. It is unlikely that any difference in HA localization is due to differences in trafficking between NL1FL and NL1ΔC, as both lines showed the same subcellular localization patterns. Also, we observed that both

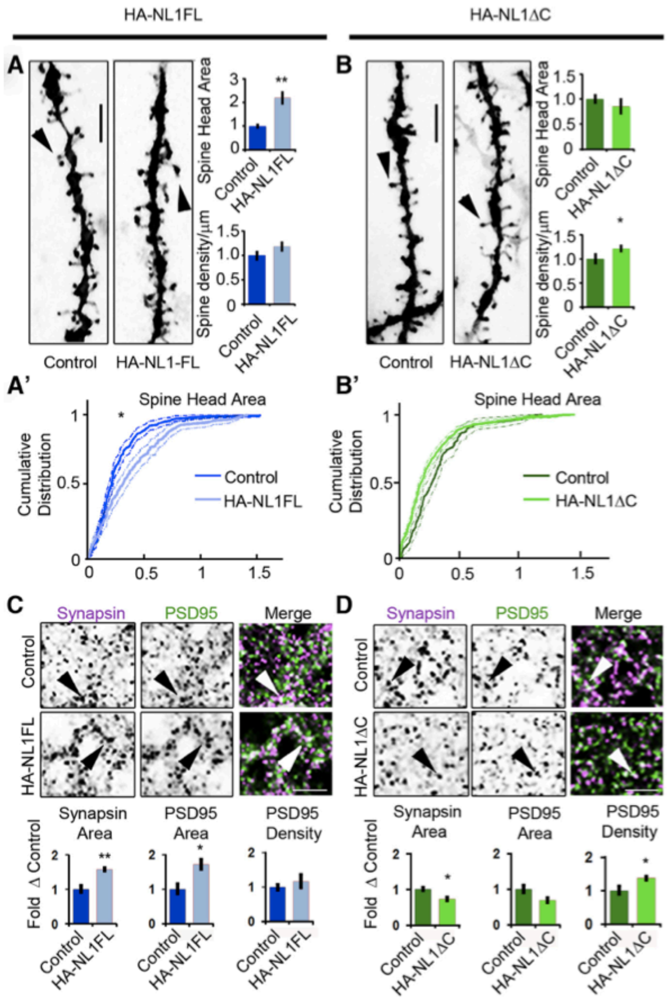

Figure 2. NL1 intracellular signaling regulates the morphological characteristics of spines and synapses in SLM. ***A, B,*** Representative images of dendritic spine segments labeled with DiI of control versus HA-NL1FL mice (A) and control versus HA-NL1ΔC mice (B). Scale bar, 2.5 µm. The mean spine head area was increased for only the HA-NL1FL mice, while spine density was only increased in the HA-NL1ΔC mice ($p < 0.05$, Student's *t* test, $n = 36$ pairs). ***A', B',*** Cumulative distributions with confidence intervals of spine head sizes across 36 dendritic segments from each transgenic group compared with their controls. Significant differences in the distributions were tested with the Kolmogorov–Smirnov test, $p < 0.00001$ for controls versus HA-NL1FL mice and $p = 0.077$ for controls versus HA-NL1ΔC mice. ***C, D,*** Representative images and quantification of Synapsin I and PSD-95- positive puncta characteristics of controls versus HA-NL1FL mice (C) and controls versus HA-NL1ΔC mice (D). Areas positive for immunostaining are black. The merge image is shown in color, with Synapsin I in magenta, PSD-95 in green and areas of overlap appearing white. Arrows highlight Synapsin I and PSD-95 colocalization. Scale bar, 2.5 µm. All data are shown mean ± SEM. Student's *t* test performed in all cases unless otherwise noted, $*p < 0.05$, $**p < 0.01$, $n = 4$ pairs (4 double positive transgenics in each group or 4 mixed single transgenic controls).

transgenes, when imaged at higher magnification in the SLM and SR, primarily localized to sites positive for PSD-95 immunolabeling and were far less frequently observed to colocalize with GABA-ARα1 (Fig. 1 E, F). This is consistent with previous reports that NL1 trafficking to synapses is independent of C terminus signaling (Dresbach et al. 2004; Prange et al. 2004).

Finally, labeling of the HA-tag together with cell nuclei (DAPI) in hippocampal sections showed that 88 ± 3.12% of cells in CA1 of the HA-NL1 mice express the transgene, while 93 ± 1.42% of cells in CA1 of the HA-NL1ΔC mice express that transgene. Overall cell densities in the CA1 regions of both lines were not different from each other, suggesting that nonspecific effects such as cell death would not interfere with subsequent analyses. Therefore, the expression patterns present in the two lines of mice are comparable and allowed for a straightforward comparison of synaptic and behavioral profiles.

Overexpression of NL1FL and NL1ΔC differentially modulate spines and synapses in the SLM

Previous *in vivo* studies of NL1 function suggest that this gene positively regulates the size and function of excitatory synapses (Dahlhaus et al. 2010). Therefore, we hypothesized that our manipulations would significantly impact morphological features of synaptic maturity. To determine whether we could identify the predicted shifts in the synaptic population, we measured both spine morphology and the presence of mature synaptic proteins in the hippocampus of both HA-NL1FL and HA-NLΔC mice.

Given the expression pattern of our transgenes, we were afforded the opportunity to examine how such alterations may have been specific to targeted layers within the hippocampus (Fig. 1C,D). We labeled CA1 neurons in the hippocampus with DiI and imaged dendrites and spines from the SLM and SR target layers at high magnification. In HA-NL1FL mice, there was a >2-fold increase in the average area of spine heads in the SLM (220.4 ± 25.0% vs 100 ± 8.3%, respectively, $p < 0.01$, $n = 36$, Student's *t* test), but no significant change in density (Fig. 2A). Interestingly, we did not see significant changes in spine head area (119.8 ± 8.2% vs 100 ± 9.9%, $p > 0.05$), nor density (110.0 ± 8.2% vs 100 ± 4.1%, $p > 0.05$) in the SR of HA-NL1FL animals. This is consistent with the idea that the region with the highest level of transgene expression was the most affected. In HA-NL1ΔC animals, we found a significant 21% increase in the density of spines in SLM (121.0 ± 6.2% vs 100 ± 10.0% normalized density, $p < 0.05$), and no significant change in spine head area (85.9 ± 14.1% vs 100 ± 8.5% normalized area, $p = 0.08$, $n = 36$, Student's *t* test; Fig. 2B). No significant difference in density (114.1 ± 4.9% vs 100 ± 8.7%, $p > 0.05$), nor spine head area (115.1 ± 10.9% vs 100 ± 16.8%, $p > 0.05$) was found in the SR. Therefore, overexpression of HA-NL1ΔC distinctly alters synaptic number as compared with the overexpression of HA-NL1FL. Such differences between the two transgenic lines suggest that the intracellular region deleted in NL1ΔC is required to drive an increase in the proportion of morphologically mature synaptic phenotypes when NL1FL is overexpressed.

As another measure of the maturity of synapses, we quantified the area and density of Synapsin I puncta, a marker of mature presynaptic terminals, and PSD-95-

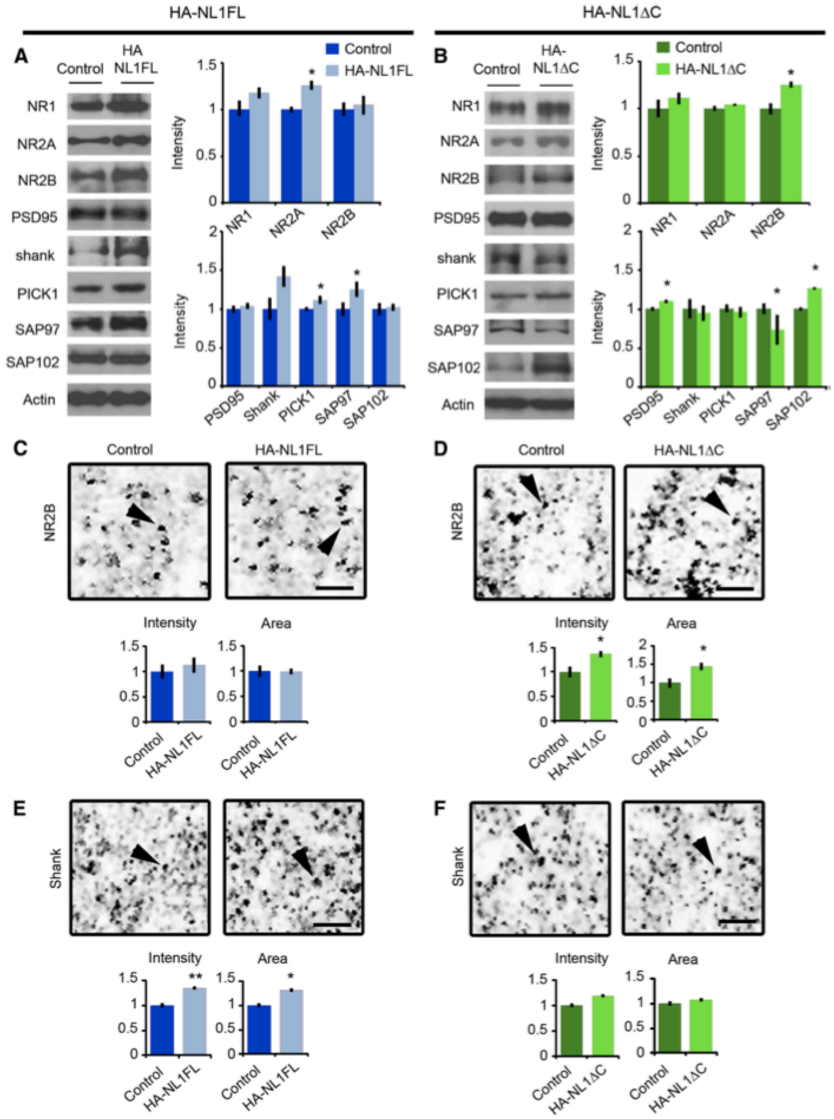

Figure 3. Distinct changes in synaptic protein composition in HA-NL1FL versus HA-NL1ΔC mice. Representative Western blots of synaptosomal fractions from the hippocampus of controls versus HA-NL1FL mice (A) and controls vs HA-NL1ΔC mice (B). Lanes are aligned to show the same mouse from each group, with the mean intensity from four individuals plotted on the right normalized to control levels. A subset of the total blots performed showing the significant differences are shown here, detailed statistics and additional blot shown in Tables 1 and 2. Representative images of a $36\ \mu m^2$ region of SLM from sectioned tissue immunolabeled for NR2B from controls versus HA-NL1FL mice (C) and controls versus HA-NL1ΔC mice (D). Average intensity and area of puncta from the four individuals from each group is graphed below. Scale bar, 2 μm. Arrows highlight puncta for comparison. Representative images of a region of SLM labeled for panShank from controls versus HA-NL1FL mice (E) and controls versus HA-NL1ΔC mice (F). Scale bar, 2 μm, and arrows highlight puncta for comparison. Significance was determined with Student's *t* test, all data are shown mean ± SEM, $^{*}p < 0.05$, $^{**}p < 0.01$, $n = 4$ pairs (4 mice in each group).

Table 1. Differences in protein expression levels in synaptosome fractions between HA-NL1FL and HA-NL1ΔC mice

Protein	% Δ	SEM	*p* value	Effect size	Cohen's *d*
HA-NLIFL					
NL1	183.00	1.23	0.0004**	0.96	7.93
NL3	155.68	56.80	0.2372	0.75	2.29
NR1	118.26	5.00	0.0610	0.76	2.33
NR2A	126.48	3.73	0.0161*	0.89	3.80
NR2B	109.27	10.36	0.7633	0.48	1.08
GluR1	111.98	4.55	0.0518	0.80	2.71
GluR2	120.86	5.74	0.1127	0.86	3.31
PSD-95	103.96	2.83	0.4515	0.57	1.37
PanShank	141.98	12.23	0.1035	0.85	3.29
Gephyrin	108.17	7.12	0.2058	0.51	1.19
PICK1	111.49	4.04	0.0370*	0.88	3.81
SAP97	125.33	8.71	0.0322*	0.85	3.17
SAP102	102.26	3.35	0.4964	0.19	0.39
SNAP25	107.86	2.69	0.4745	0.53	1.24
Synapsin1	119.35	2.67	0.0185*	0.97	7.56
VGLUT1	101.17	1.51	0.0799	0.39	0.85

Summary statistics for levels of all synaptic proteins analyzed from hippocampal synaptosome fractions from controls versus HA-NL1FL mice. Significance was determined with Student's *t* test, *$p < 0.05$ and **$p > 0.01$, $n = 4$ animals in each group.

Table 2. Differences in protein expression levels in synaptosome fractions between HA-NL1FL and HA-NL1ΔC mice

Protein	% Δ	SEM	*p* value	Effect size	Cohen's *d*
HA-NL1ΔC					
NL1	198.43	5.73	0.0021**	0.99	15.88
NL3	108.73	0.94	0.1380	0.63	1.65
NR1	111.18	5.12	0.1481	0.62	1.56
NR2A	104.31	0.27	0.1732	0.78	2.48
NR2B	125.34	2.46	0.0443*	0.96	6.51
GluR1	148.80	7.49	0.2250	0.83	2.98
GluR2	116.56	4.04	0.1018	0.85	3.16
PSD-95	109.92	0.87	0.1834	0.97	7.37
PanShank	94.61	8.89	0.7536	−0.25	−0.52
Gephyrin	96.73	1.17	0.1823	−0.78	−2.65
PICK1	95.85	5.67	0.6600	−0.37	−0.79
SAP97	73.14	18.44	0.0213*	−0.70	−1.95
SAP102	126.59	0.40	0.0316*	0.99	44.66
SNAP25	105.48	0.96	0.0065**	0.92	4.65
Synapsin1	112.16	1.78	0.0782	0.81	2.75
VGLUT1	98.99	0.73	0.2849	−0.52	−1.22

Summary statistics for levels of all synaptic proteins analyzed from hippocampal synaptosome fractions from controls versus HA-NL1ΔC mice. Significance was determined with Student's *t* test, *$p < 0.05$ and **$p > 0.01$, $n = 4$ animals in each group.

positive puncta, a marker of mature postsynaptic densities. In HA-NL1FL mice, we found significant changes consistent with an increase in the prevalence of mature synaptic structures in SLM. The average area of Synapsin I puncta was increased relative to littermate controls (area: 158.5 ± 5.4% vs 100 ± 11.5%, $p < 0.01$; Fig. 2C). The average area of PSD-95 puncta was also enhanced without significant changes in intensity (area: 173.2 ± 15.0% vs 100 ± 16.1%, $p < 0.01$; Fig. 2C). These changes are consistent with an increase in the proportion of mature synaptic structures present. However, we did not observe a significant increase in the number of PSD-95 and Synapsin I-positive puncta per 100 μm^2 (123.5 ± 9.8% vs 100 ± 13.5%, $p > 0.05$). This corroborates the idea that HA-NLFL overexpression altered the state of the synapses present, but without a significant increase in synapse number in the SLM.

Remarkably, we observed distinct changes in Synapsin I and PSD-95 labeling in mice overexpressing HA-NL1ΔC. We detected a significant decrease in the area of Synapsin I-positive puncta (area: 72.9 ± 4.9% vs 100 ± 5.8%, $p < 0.05$; Fig. 2D), without a significant decrease in the area of PSD-95 puncta (70.1 ± 6.12% vs 100 ± 12.2%, $p > 0.05$; Fig. 2D). Consistent with the changes in spine numbers, we also observed a significant increase in the density of PSD-95 puncta (137.8 ± 4.4% vs 100 ± 7.8%, $p < 0.05$; Fig. 2D). These results substantiate that in contrast to HA-NL1FL overexpression, HA-NL1ΔC overexpression increased the total number of synapses.

HA-NL1FL and HA-NL1ΔC overexpression induce distinct changes in synaptic protein localization

Studies characterizing the molecular composition of excitatory synapses across development have found activity-dependent changes in the prevalence of postsynaptic scaffolding molecules and glutamate receptors at distinct developmental stages (Petralia et al. 2005; van Zundert et al. 2004; Zheng et al. 2011). We therefore predicted that our manipulations of NL1 function should impact the postsynaptic scaffolding molecules and glutamate receptors associated with progression through development and synaptic maturation. We examined protein levels at synapses in both the HA-NL1FL and HA-NL1ΔC animals via quantitative immunoblotting of isolated synaptosome fractions from hippocampal tissue. Overexpression of NL1FL within restricted regions of the hippocampal formation led to a significant increase in synaptic levels of Synapsin I, SAP97, PICK1, and NR2A (Fig. 3A, Table 1). We observed no significant changes in the synaptic levels of PSD-95, nor the key inhibitory synaptic marker Gephyrin. In contrast, overexpression of HA-NL1ΔC resulted in enhanced levels of SAP102 and PSD-95, a modest increase in NR2B levels and a decrease in SAP97 (Fig. 3B, Tables 1, 2). Together, these changes indicate that there was an overall enrichment of synaptic proteins associated with mature features of excitatory synapses in the hippocampi of the HA-NL1FL animals, whereas HA-NL1ΔC overexpression modulated proteins particularly relevant to developing synapses.

To confirm that the changes in synaptic protein levels were directly related to the level of expression of our transgenes, we analyzed immunostaining characteristics of a

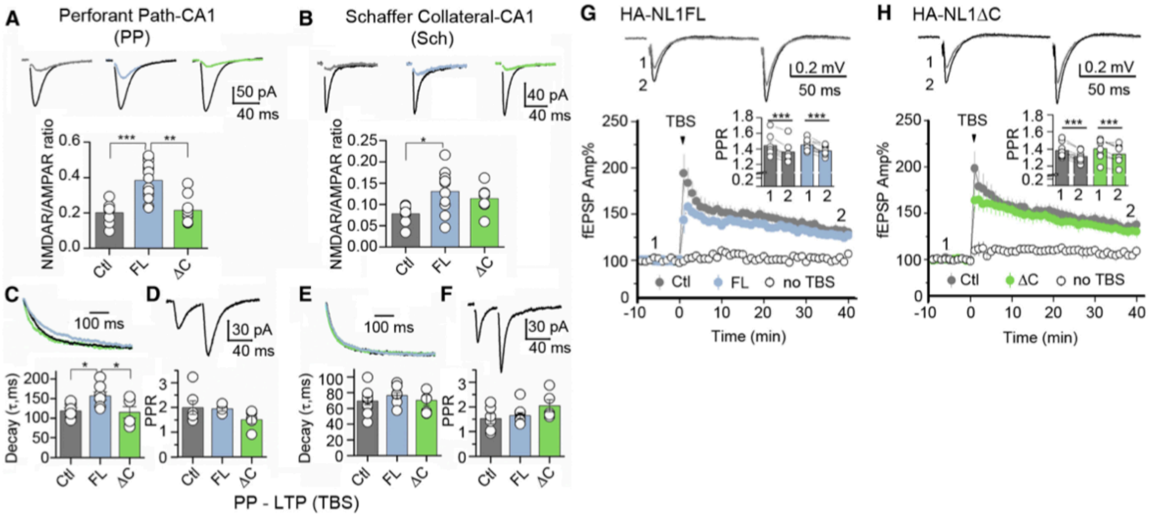

Figure 4. Manipulations of NL1 specifically affect NMDAR-mediated synaptic transmission in hippocampus. Comparisons of NMDAR-mediated synaptic transmission at PP-CA1 versus Sch-CA1 synapses. ***A,*** AMPAR and NMDAR-mediated EPSCs were measured from the same CA1 neuron (V_h = -60 mV) in the continuous presence of 100 µM picrotoxin for AMPAR-EPSCs or picrotoxin and 10 µM NBQX for NMDAR-EPSCs. Representative AMPAR-EPSC traces (black) and NMDAR- EPSCs (representative colors) are shown on top, *N* = 7 cells in each group (13 cells max). ***B,*** Similar measures taken at the Sch. ***C,*** Decay kinetics of NMDAR-EPSCs. NMDAR-EPSCs were measured at +30 mV in the presence of picrotoxin and NBQX, *N* = 6 (max 10). Representative traces are shown at top, and group averages are shown in a graph below. ***D,*** Paired-pulse ratio (PPR) of AMPA EPSCs was measured at -60mV, 50ms apart in the PP revealing no differences between transgenic lines and controls. ***E,*** No differences were found in decay kinetics at the Sch, and (F) no differences were found in PPR of AMPAR EPSCs measured at -60 mV, 40ms apart, *N* = 4 (max 9). ***G, H,*** LTP at the PP-CA1 synapse. Field EPSPs were measured in presence of 100 µM picrotoxin and 3 µM CGP-55845. Representative traces were taken at time points (1 and 2) and are shown at top. Summary plots showing PP-LTP induced by TBS in Controls (Ctl, 3 mice, 7 slices (G) and 9 slices (H)), HA-NL1ΔC (ΔC, 3 mice; 8 slices) and HA-NL1FL (FL, 3 mice, 9 slices) mice. All experiments included an independent, PP-CA1 naive pathway ("no TBS"). Insets, Summary of PPR before (1) and after (2) LTP induction for FL and ΔC mice. All data are presented as mean ± SEM, and traces are illustrated as averages of 10 –15 individual responses. Stimulus artifacts were digitally removed. *$p < 0.05$, **$p < 0.01$, ***$p < 0.001$.

few key synaptic proteins in the SLM and SR of the hippocampus. We failed to identify any changes in measures of NR2B immunofluorescence within the hippocampus of HA-NL1-FL mice (Fig. 3C). However, the intensity and area of NR2B puncta specifically within the SLM of HA-NL1ΔC animals were enhanced relative to controls (Intensity: 136.8 ± 3.8 vs 100 ± 9.4%, $p < 0.05$, Area: 143.5 ± 7.4 vs 100 ± 8.3, $p < 0.01$; Fig. 3D). We observed no significant difference of NR2B staining within the SR (Intensity: 130.8 ± 11.5 vs 100 ± 7.6, $p > 0.05$, Area: 132.2 ± 16.9% vs 100 ± 7.0%, $p > 0.05$), nor the stratum lucidum of CA3 (Intensity: 100 ± 9.6% vs 111.3 ± 7.1%, $p > 0.05$).

Immunolabeling with an antibody to all three Shank family members (pan-Shank) revealed that levels of one or all members were specifically increased in the SLM of HA-NL1FL mice relative to controls (Intensity: 135.2 ± 1.6% vs 100 ± 2.7%, respectively, $p < 0.01$, Area: 131.7 ± 18.9% vs 100 ± 12.6%, $p < 0.05$; Fig. 3E). There was no significant change in pan-Shank labeling in HA-NL1ΔC mice (Fig. 3F). Our results demonstrate that our manipulations induced the largest changes in regions with higher levels of transgene expression, specifically, the SLM. Therefore, given our biochemical data and the clear differences between HA-NL1FL and HA-NL1ΔC mice, we conclude that the intracellular C-terminal region that is missing from the HA-NL1ΔC protein is required for the additional recruitment of Synapsin1, SAP97, PICK1, and Shank family members observed when NL1FL is overexpressed. Moreover, the differences between overexpressing NL1FL and NL1ΔC modulate NMDAR subunit composition *in vivo.* Such activities have been implicated in the normal maturation of excitatory synapses over development.

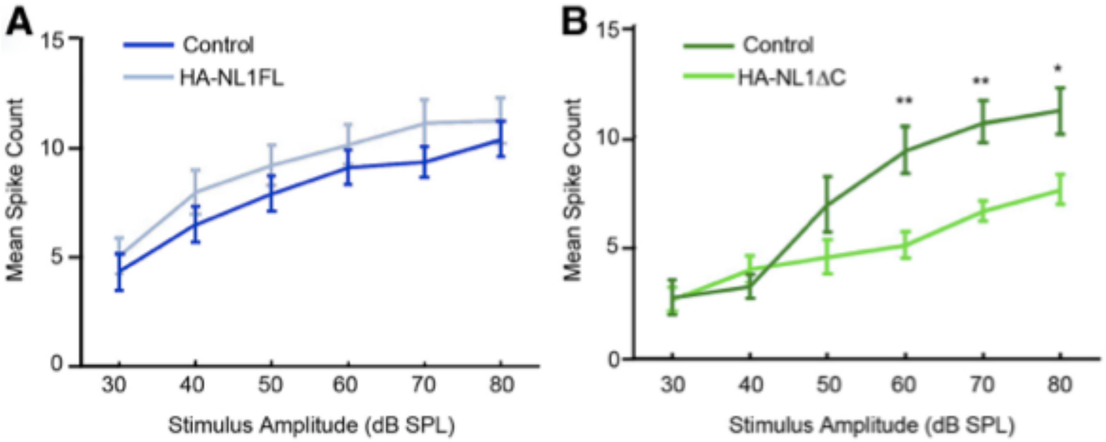

Figure 5. Changes in synaptic transmission in primary sensory cortex. Differences in the input/output function of synaptic transmission in auditory cortex. ***A,*** Mean spike counts for neurons in the auditory cortex activated by differing levels of stimulus strength (white noise clicks) are plotted for both controls (dark blue) and HA-NL1FL mice (light blue). ***B,*** HA-NL1ΔC mice showed an increase in the stimulus threshold necessary for eliciting an increase in firing rate. All data are shown mean ± SEM, and significance was determined by repeated-measures ANOVA, $n = 5$ pairs (5 animals in each group),$^*p < 0.05$ and $^{**}p < 0.01$.

Discrete changes in synaptic transmission characterize HA-NL1FL and HA-NL1ΔC overexpressing mice

Given the observed changes in morphology and biochemistry, and previous reports of NL1's influence on NMDARs, we specifically compared the ratio of NMDAR to AMPAR-mediated synaptic transmission, NMDAR decay kinetics, and paired-pulse facilitation in the SLM and SR. AMPAR and NMDAR-mediated EPSCs in CA1 pyramidal cells were elicited by stimulating either perforant path (PP) fibers that innervate SLM or Schaffer collaterals (Sch) that innervate SR in the acute hippocampal slice preparation (see Materials and Methods). HA-NL1FL overexpression in both the PP and in the Sch-CA1 synapses, led to significant enhancement in the NMDAR/AMPAR ratio relative to controls (0.38 ± 0.03, $n = 13$, HA-NL1FL vs 0.20 ± 0.02, $n = 8$; controls, *p* = 6.66 x 10^{-5}, at PP-CA1; 0.13 ± 0.02, *n* = 10; HA-NL1FL vs 0.08 ± 0.007, *n* = 9; Controls, *p* = 0.011 at Sch-CA1; Fig. 4A,B). Note that the ratio was only significantly different between the HA-NL1FL mice and HA-NL1ΔC mice in the SLM (0.38 ± 0.03, *n* = 13, HA-NL1FL vs 0.22 ± 0.02, *n* = 10, HA-NL1ΔC, *p* = 1.72 x 10^{-4}). Consistent with our other findings, HA-NL1ΔC failed to induce a change in the NMDAR/AM-PAR ratio in both SLM and SR. Surprisingly, we also found that overexpression of HA-NL1FL led to longer NMDAR decay kinetics at PP-CA1 synapses (156.44 ± 10.67 ms, *n* = 10, HA-NL1FL vs 118.39 ± 7.93 ms, *n* = 6, Controls, *p* = 0.02; Fig. 4C). Overexpression of HA-NL1ΔC did not induce this change (115.04 ± 14.58 ms, *n* = 7, HA-NL1ΔC vs 118.39 ± 7.93 ms, *n* = 6, Controls, *p* = 0.85). In contrast, we found no significant alteration between genotypes in NMDAR EPSC decay kinetics at Sch-CA1 synapses showing that this phenotype is specific to the SLM (Fig. 4E).

To examine whether our manipulations could also affect presynaptic function, we measured paired-pulse facilitation. We found no significant differences in this measure between any group (Fig. 4D,F). Finally, to quantify the contribution of NR2B to PP-CA1 synaptic transmission in HA-NL1ΔC mice, we tested the effect of the selective NR2B antagonist Ro 25-6981 on NMDAR-mediated transmission in the SLM (see Materials and Methods). Application of Ro (500 nM) reduced NMDAR transmission, but this reduction was not significantly different between groups (HA-NL1ΔC 80.5 ± 1.95% of baseline, *n* = 8; Control 83.8 ± 2.0% of baseline, *n* = 6; *p* = 0.23, data not shown). The modest increase in NR2B localization in the SLM of the HA-NL1ΔC mice (Fig. 3 *B, D)* did not result in a specific and significant increase in NR1/NR2B containing heterodimers, but may have instead increased the number of NR1/NR2A/NR2B heterotrimers, which are less sensitive to Ro (Tovar and Westbrook 1999).

We next investigated whether overexpression of HA-NL1FL and HA-NL1ΔC could affect the induction of NMDAR-dependent LTP at PP-CA1 synapses (PP LTP) (see Materials and Methods). We found no significant difference in the magnitude of PP LTP in hippocampal slices prepared from HA-NL1FL and HA-NL1ΔC mice compared with interleaved control slices (HA-NL1FL 126.27 ± 3.41% of baseline, three mice, nine slices; Control 131.92 ± 5.22% of baseline, three mice, seven slices; HA-NL1FL vs Control $p = 0.3616$; HA-NL1ΔC 131 ± 5.16% of baseline, three mice, eight slices; Control 136.45 ± 6.70% of baseline, three mice, nine slices; HA-NL1ΔC vs Control $p = 0.5515$; Fig. 4G,H). PP LTP was associated with a significant reduction in PPR (HA-NL1FL 1.45 ± 0.024 before, 1.38 ± 0.02 after $p = 0.00045$; Control 1.44 ± 0.053 before, 1.36 ± 0.051 after, $p = 0.00031$; HA-NL1ΔC 1.40 ± 0.043 before, 1.34 ± 0.039 after, $p = 0.00172$; Control: 1.38 ± 0.028 before, 1.31 ± 0.021 after, $p = 0.00058$; Fig. 4G,H, insets). This result is consistent with a previous report that an important component of this form of plasticity is expressed presynaptically (Ahmed and Siegelbaum 2009). Collectively, our functional analysis supports the idea that NL1FL overexpression affected NMDAR-mediated synaptic transmission, and that this effect requires the NL1 C-terminal region as overexpressing NL1ΔC yielded no significant physiological changes in our measures.

We primarily investigated synaptic changes in the hippocampus in our transgenic animals as we saw the strongest expression levels within a specific target layer in this structure. However, our transgenes were also expressed throughout other forebrain structures, including specific layers within primary sensory cortices (Fig. 1). Moreover, our data and others show that overexpression of NL1FL reliably impacts synaptic spine morphology, while our data additionally shows that HA-NL1-ΔC overexpression impacts spine number. Both of these synaptic features, abnormal spine number and morphology, have been observed in temporal lobe cortex in humans with ASD (Hutsler and Zhang 2010; Penzes et al. 2011). As this region of cortex in humans processes auditory information, we additionally assayed for changes in sensory-evoked responses in primary auditory cortex in our mice. We could not detect a significant change in the relationship between neuronal firing rates and stimulus strength in the auditory cortex of HA-NL1FL mice (Fig. 5A). However, we found a significant shift in the threshold for evoking sensory responses in the HA-NL1ΔC mice as compared with controls (Fig. 5B). Basic auditory responses such as the startle reflex were unaffected (data not shown). Interestingly, such a shift in the threshold for sensory-evoked responses is a characteristic developmental milestone in the auditory cortex, where a decrease in the threshold to elicit a change in firing rate accompanies developmental progression (de Villers-Sidani et al. 2007; Moore and Irvine 1979). Thus, our findings suggest that the changes elicited by NL1ΔC overexpression in cortex correlate to developmentally relevant changes in sensory-evoked responses in at least the primary auditory cortex, while the NL1FL overexpression effects were unable to bring about a change in this measure.

Figure 6 (Next page). Manipulations of NL1 intracellular signaling distinctly alters performance in learning and memory behaviors. ***A,*** Mean latency in seconds (s) of transgenics (solid, light blue, and green lines) and their controls (dashed, dark blue, and green lines) during the visually cued training trials. Days of training labeled D1–D2. ***A',*** Mean distance traveled before reaching the platform in the visually cued training trials. ***B,*** Mean latency in seconds (s) to find hidden platform during acquisition training showing significant differences in the performance of only the HA-NL1FL mice from controls. ***B',*** Mean distance traveled before reaching the hidden platform during acquisition training showing significant differences in distances traveled to reach the platform. ***C,*** Representative paths traveled from each group of mice during a 60 s probe trial after acquisition training showing significant changes in searching behavior. All plots were oriented to align the target quadrant to the lower left for comparison purposes. ***D,*** Significant differences in percentage time spent in either the target quadrant, quadrants adjacent to the target, or the opposite quadrant during the 60 s probe trial for the transgenics (light blue and green bars) versus each other and their controls (dark blue and green bars). ***E,*** Significant differences in mean number of crosses of former platform location and (E') mean distance in centimeters to reach former target location during the 60 s probe trial following acquisition. ***F,*** Significant differences in mean latency in seconds (s) and (F') mean distance traveled (cm) to reach new platform location in reversal training. Transgenics are labeled as solid, light blue, and green lines and their controls are dark blue and green, dashed lines. Days of training labeled D1–D3. ***G,*** Representative search paths on the fourth training trial of Day 1 of reversal training revealing distinct differences between transgenics and their controls. The former target location has been aligned to the lower left quadrant for comparison between groups, meaning the new location is in the upper right quadrant. ***H,*** Mean number of crosses over former target location and (H') percentage time in former target quadrant during the fourth training trial of the first day between transgenics and controls serves as a measure of persistence in using old information after experiencing new conditions. ***I,*** Object recognition memory to assess short-term memory, 1 h delay between object exposure, and (J) long-term memory, 24 h delay, differences between HA-NL1FL mice (light blue bars) and HA-NL1ΔC mice (light green bars). ***K,*** Comparison of swim speeds in cm/s between transgenic mice (solid, light blue, and green lines) and their controls (dashed, dark blue, and green lines) during distinct phases of water maze training. Days of visual training, V1–V2; days of acquisition training, A1–A7; and days of reversal training, R1–R3. All data shown are mean ± SEM, significance determined with repeated-measures ANOVA with Tukey–Kramer HSD, *post hoc,* $^*p < 0.05$, *n* = 21 littermate pairs (10 –11 double positive transgenic in each group or 10 –11 mixed single transgenic controls).

Overexpression of HA-NL1FL versus HA-NL1ΔC differentially impact behavioral performance in learning and memory tasks

Distinct behavioral differences between the HA-NL1FL mice and the HA-NL1ΔC mice would argue that the intracellular domain of NL1 that is removed in NL1ΔC is key in modulating changes to synaptic function and behavior when NL1 is overexpressed.

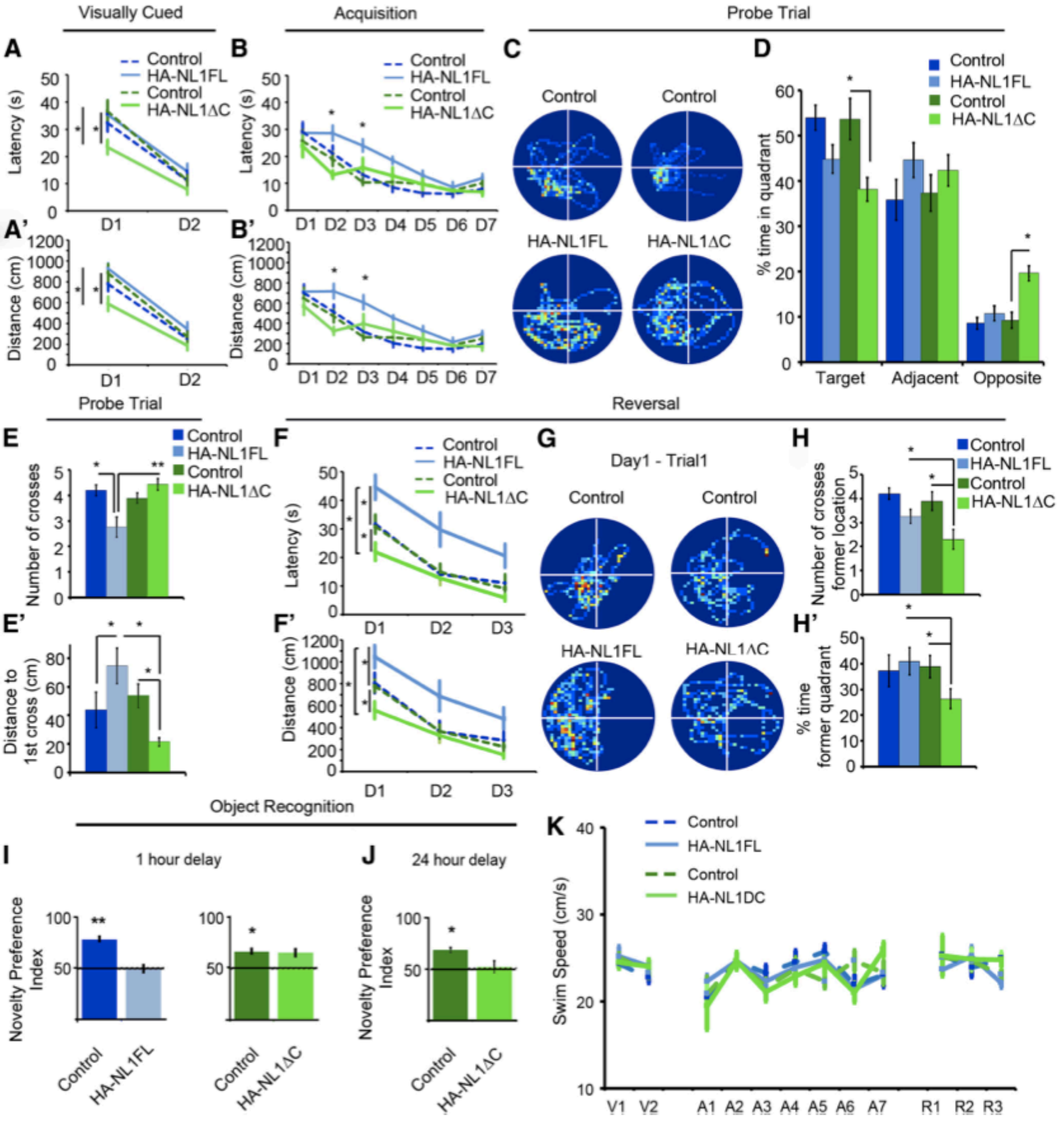

Given that overexpression and knock-out of NL1 has been found to impact explicit learning and memory behaviors as assessed by the Morris water maze (Blundell et al. 2010; Dahlhaus and El-Husseini 2010), we first characterized the behavior of our transgenic mice in the same task. Importantly, we directly compared the behavior of both lines and their respective controls in the same experiment.

Specific aspects of performance in the water maze task were different between the HA-NL1FL and HA-NL1ΔC mice, while swim speed and thigmotaxic behavior were not significantly different between all groups throughout training (Fig. 6K; not shown). First, we noticed that HA-NL1ΔC overexpressing mice learned to reach a visually cued platform in less time and with less distance traveled than all the other groups on the first day of training (main effect of genotype on latency: $F_{(3,74)} = 4.14$, $p < 0.01$, main effect of day: $F_{(1,74)} = 101.62$, $p < 0.001$, no significant effect of genotype x day interaction; Fig. 6A,A'). Second, during acquisition training, only the HA-NL1FL overexpressing mice took significantly more time and distance over more days to learn the target location relative to all other groups (main effect of genotype on latency: $F_{(3,259)} = 14.26$, $p < 0.001$, main effect of day: $F_{(6,259)} = 38.63$, $p < 0.001$, main effect of genotype x day interaction: $F_{(18,259)} = 1.67$, $p < 0.05$; Fig. 6 *B, B').* These data support the idea that the two transgenic lines exhibit distinct learning behaviors during the acquisition phases of the Morris water maze task.

Analysis of probe trial performance after acquisition training also revealed differences between the HA-NL1FL and theHA-NL1ΔC mice with respect to recall-related behaviors. The HA-NL1ΔC mice were the only ones to spend a significantly reduced amount of time in the target quadrant (38.11 ± 2.64%, HA-NL1ΔC mice vs 53.58 ± 4.54%, controls, $p < 0.001$; Fig. 6C,D). Concurrently, there was also a significant increase in dwell time spent by the HA-NL1ΔC mice in the quadrant opposite to the target location relative to their controls (19.57 ± 1.65% vs 9.18 ± 1.75%, $p < 0.001$) and relative to the HA-NL1FL mice (19.57 ± 1.65% vs 10.68 ± 1.62%, $p < 0.001$). Interestingly, the HA-NL1ΔC mice also traveled a significantly shorter distance to their first cross of the former platform location relative to their controls (ΔC controls, 53.78 ± 8.39 cm, $p < 0.0167$) and there were no significant differences in the distances traveled between the two control groups ($p > 0.05$). This suggests enhanced flexibility in search strategy. In contrast, the HA-NL1FL mice traveled more distance before making their first cross of the former platform location relative to the HA-NL1ΔC mice (74.63 ± 12.42 cm vs 21.31 ± 2.75 cm, $p < 0.01$; Fig. 6E'), and made significantly fewer crosses of the former platform location relative to their controls (2.75 ± 0.39 vs 4.10 ± 0.24, $p < 0.01$; Fig. 6E) and relative to the HA-NL1ΔC mice (4.23 ± 0.34, $p < 0.01$), despite comparable dwell time in the correct area. Therefore, the HA-NL1FL mice presented classical deficits associated with impaired recall performance, whereas the HA-NL1ΔC mice showed a distinct set of behavioral traits that suggested subtle enhancements in learning and increased flexibility in search strategy.

As further evidence for change in behavioral flexibility in the water maze task in our transgenic lines, we also found differences in behavior during reversal training (main effect of genotype: $F_{(3,111)} = 15.32$, $p < 0.001$, main effect of day: $F_{(2,111)} = 35.16$, $p < 0.001$, main effect of genotype x day interaction: $F_{(6,111)} = 0.41$, $p > 0.05$; Fig. 6 F, F').

The number of crosses of the former platform location was reduced in the HA-NL1ΔC mice relative to controls (2.3 ± 0.40 crosses vs 3.89 ± 0.3 crosses, $p < 0.01$), and relative to the HA-NL1FL mice (3.29 ± 0.24, $p < 0.0167$; Fig. 6H). Similarly, dwell time in the quadrant that formerly contained the platform was significantly lower for the HA-NL1ΔC mice relative to their controls (25.97 ± 3.70% vs 39.76 ± 3.99%, $p < 0.0167$; Fig. 6H'), and relative to the HA-NL1FL mice (HA-NL1FL mice: 40.88 ± 5.27%, $p < 0.025$; Fig. 6H'). Moreover, the HA-NL1FL mice displayed increased dwell time in the former target quadrant and an increased number of crosses of the former platform location than their controls on the second day of reversal training (percentage dwell time: 33.31 ± 4.23 vs

---

Figure 7 (Next page). Manipulations of NL1 intracellular signaling affect social behavior. ***A,*** Performance in the three-chambered social preference task. Mean time in seconds (s) spent in the chamber, with either a social partner (Social) or an object (Object), is depicted for both controls (dark blue bars) and HA-NL1FL mice (light blue bars) in the left graph. ***B,*** Mean time spent in a chamber with either a familiar social partner (Familiar) or a novel social partner (Novel) is depicted. ***C,*** Representative exploration paths during a choice to investigate a familiar or a novel social partner, control performance at top, and HA-NL1FL performance at bottom. ***D,*** Preference for social interaction over interaction with an object for control (dark green bars) and HA-NL1ΔC mice (light green bars). ***E,*** Significant differences in preference for familiar animals versus novel animals in controls (dark green bars) versus HA-NL1ΔC mice (light green bars). ***F,*** Representative exploration paths during a choice to investigate a familiar or a novel social partner, control performance at top, and HA-NL1ΔC performance at bottom. ***G,*** Left, Attack frequency differences during the resident–intruder task after prolonged social isolation between controls (dark blue) and HA-NL1FL mice (light blue). Right, Win frequency during the dominance tube test is graphed to the right. ***H,*** Left, Attack frequency differences during the resident–intruder task after prolonged social isolation between controls (dark green) and HA-NL1ΔC mice (light green). Right, Win frequency differences between controls and the HA-NL1ΔC mice. All data shown are mean ± SEM, significance was determined with repeated-measures ANOVA, with Tukey–Kramer HSD *post hoc,* $^{*}p < 0.05$, $^{**}p < 0.01$, $n = 21$ pairs (10 –11 double positive transgenic in each group or 10 –11 mixed single transgenic controls).

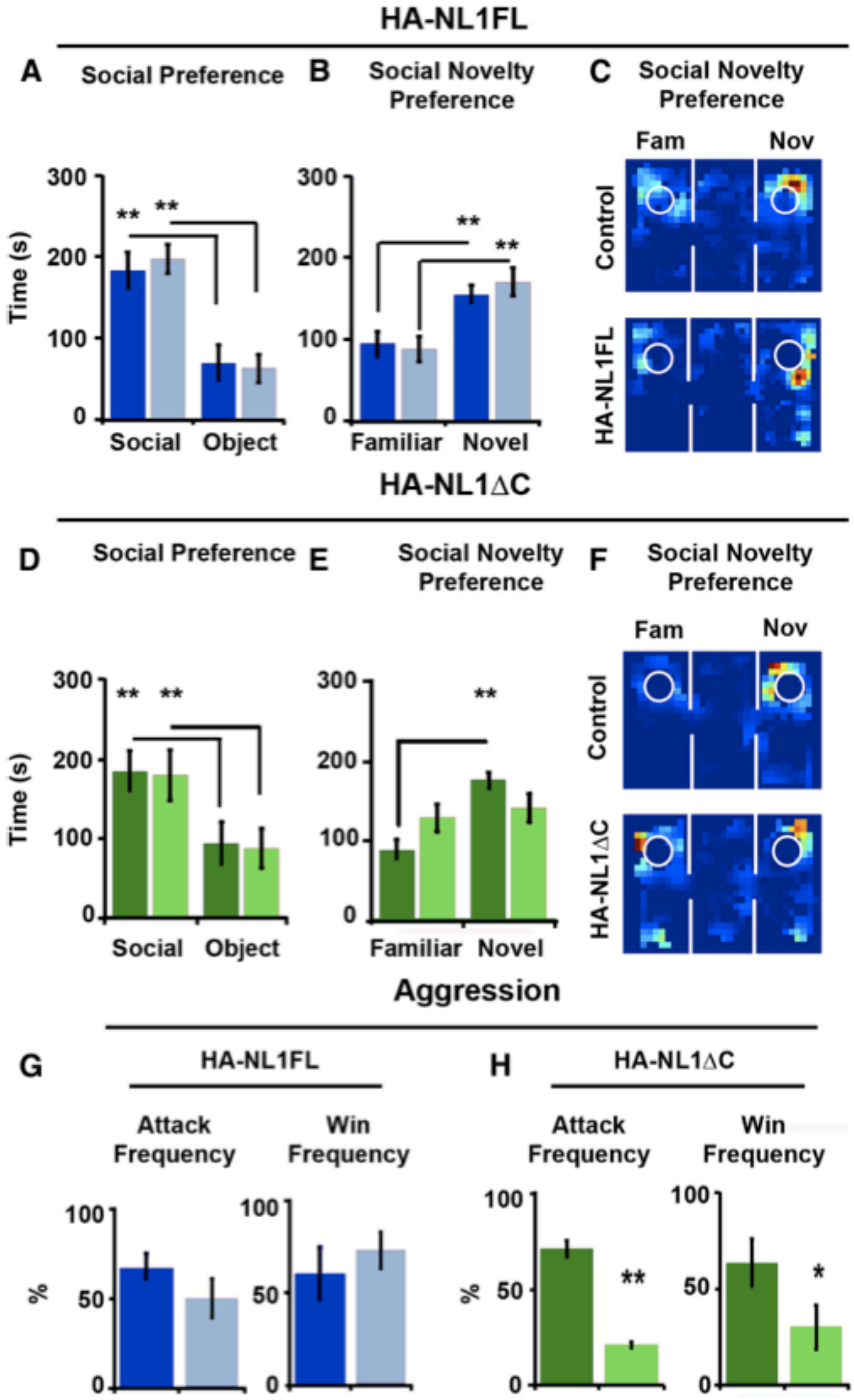
HA-NL1FL
A
Social Preference
B
Social Novelty Preference
C
Social Novelty Preference
Time (s)
300
200
100
0
**
**
Social
Object
Familiar
Novel
Fam
Nov
Control
HA-NL1FL
HA-NL1ΔC
D
Social Preference
E
Social Novelty Preference
F
Social Novelty Preference
Control
HA-NL1ΔC
Aggression
G
HA-NL1FL
Attack Frequency
Win Frequency
H
HA-NL1ΔC
Attack Frequency
Win Frequency
%
100
50
0
**
*

18.24 ± 3.98%, $p < 0.05$,crosses: 3.02 ± 0.51 vs 1.31 ± 0.34 $p < 0.05$). Together, this suggests that the HA-NL1ΔC mice abandoned searching the former location faster than all other groups during the first day of reversal training, whereas NL1FL mice persisted in searching the former location longer than all other groups. The enhanced perseverance observed in the HA-NL1FL mice relative to the control groups suggests a significant decrease in flexibility when this protein is overexpressed. These important differences highlight that overexpression of HA-NL1ΔC brought about distinct gain of function effects as opposed to the specific perturbations in behavior brought about by HA-NL1FL overexpression in this task.

To further interpret how the changes in water maze behavior related to learning and memory we also used the object recognition task. Only the HA-NL1FL mice displayed a lack of preference for the novel object after an hour delay between object familiarization and re-exposure (49.9 ± 5.4% time with new object vs 50% chance performance, $p > 0.05$, Wilcoxon signed rank test, $n = 10$ pairs; Fig. 6I). This result is consistent with a deficit in learning and recall behavior. However, we observed impairment for recall after a single exposure with a delay of 24 h in the HA-NL1ΔC mice (Novelty preference: 49.9 ± 8.8% vs 50% chance performance, $p < 0.05$, $n = 10$ pairs, Wilcoxon signed rank test; Fig. 6J). This suggested that object recognition learning over the short term occurred similarly to controls in this task, but that the single trial learning was less stable over 24 h in this group. The same differences were found in a spatial version of the object recognition task (data not shown), suggesting that these changes in recall behavior generalized to multiple forms of explicit memory formation.

Overall, the data gathered on learning and memory behaviors between the HA-NL1FL and HA-NL1ΔC mice suggest distinct differences in how the two lines of mice perform these tasks. In particular, the data reflect impaired learning and flexibility in the FL mice, yet enhanced flexibility in the ΔC mice with a weak deficit in recognition memory after a 24 h delay.

Only overexpression of NLΔC affects social behavior

NL1 function has also been linked to social behavior in studies where genetic manipulations were ubiquitous throughout the brain (Blundell et al. 2010). Moreover, it is unclear which neural circuits may process social information (Insel and Fernald 2004). We therefore studied whether our manipulations could also impact social behavior. First, the three-chambered social preference test allowed us to gauge basic social preferences (Moy et al. 2004). Typically, mice of our background strain prefer social interaction over that with an object, and interaction with a novel partner over that of a familiar (Moy et al. 2004). Surprisingly, we observed no significant differences in the behavior of the HA-NL1FL mice relative to the controls in any phase of this task (Fig. 7A–C). Both the HA-NL1FL mice and their controls showed significant preferences for social interaction ($p < 0.01$; Fig. 7A) and social novelty ($p < 0.01$; Fig. 7 B, C). In contrast, HA-NL1ΔC mice failed to show a characteristic preference for social novelty, spending equal amounts of time with a familiar mouse and a novel mouse ($p > 0.05$; Fig. 7 E, F). However, they still displayed a strong preference for social interaction relative to interaction with an object ($p < 0.025$; Fig. 7D).

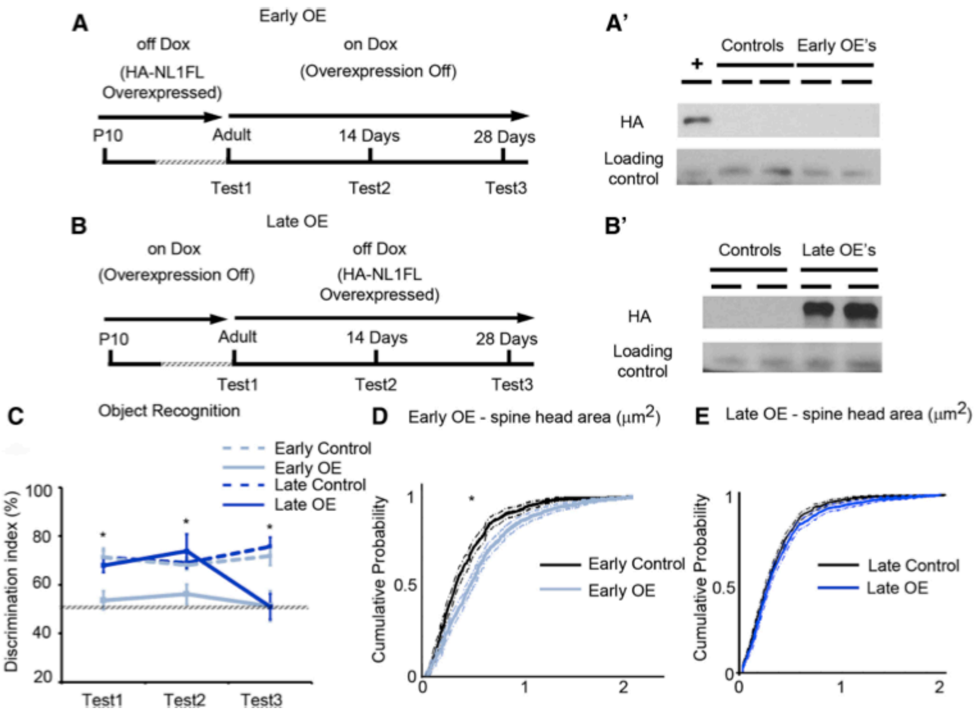

Figure 8. Overexpression of NL1FL is not required to maintain changes in synaptic maturation nor behavior, and can initiate behavioral changes in the adult. ***A,*** Summary of the experimental procedure to induce overexpression of HA-NL1FL only during development in adolescence, the Early OEs. Behavioral testing occurred first at the time when HA-NL1FL was still overexpressed (Test1), then 2 weeks after transgene expression was inhibited (Test2), and then again after 4 weeks of transgene inhibition (Test3). ***A',*** Western blots performed on forebrain homogenate of mice upon completion of behavioral testing to assess presence of transgene, + is cell lysate with HA-NL1FL present to confirm HA immunolabeling. ***B,*** Summary of the experimental procedure to induce HA-NL1FL overexpression only in the adult, leaving critical developmental periods unperturbed, the Late OEs. Initial behavior testing in these animals started just before HA-NL1 overexpression was induced in the Late OEs, (Test1), 2 weeks after transgene expression induction (Test2) and 4 weeks after induction (Test3). ***B',*** Western blot confirmation of HA-NL1FL overexpression in Late OEs. All experimental groups were compared with cohoused single positive littermates simultaneously on the same Dox diet regime. ***C,*** Performance in the object recognition task as measured by the novel object discrimination index (%) at the designated testing periods. Transgenic performances are shown in light and dark solid lines and control performances are depicted by light and dark dashed lines. All data shown are mean ± SEM, and significance determined by repeated-measures ANOVA. ***D,*** Cumulative distributions with associated confidence intervals for spine head size of the synaptic population within the SLM from the Early OEs (light blue) and their controls (black), $*p < 0.05$, Kolmogorov–Smirnov test. ***E,*** Cumulative distributions with associated confidence intervals for spine head size in the Late OEs (dark blue) and their controls (black), $p < 0.05$, Kolmogorov–Smirnov test, $n = 36$ dendritic spine segments from three to four animals in each group.

The lack of preference for a novel partner in the HA-NL1ΔC mice is unlikely to be due to the previously described differences in learning and memory, as similar tests for novel objects revealed a preference for novel objects with a delay between exposures of up to an hour. In these tests for social novelty, the delay between different phases of testing is only 15 min. Therefore, we observed a selective change in social novelty preference and not a change in preference for novelty.

We also assessed aggression and dominance behavior in male mice using both the resident-intruder task and dominance tube test (Duncan et al. 2004; Messeri et al. 1975; Moy et al. 2004). In the resident-intruder task, we saw no significant difference between the HA-NL1FL mice and controls in their interaction during this task (Fig. 7G, left). However, we found that the HA-NL1ΔC mice were less likely to initiate an attack than their controls (16.7 ± 1.1% vs 56.7 ± 3.3%, $p < 0.025$, $n = 9$ pairs; Fig. 7H, left). We saw no other significant effects in other forms of social interactions during this test, including dominant mounting behaviors (data not shown). The dominance tube test can also be used to confirm differences in dominance as it pits two mice against each other in a confined tube in which a more dominant male would force the less dominant to retreat. This test assesses more subtle levels of dominance in social interaction that may be present, but may not result in more aggressive acts such as mounting or fighting. We again found no difference in this behavioral test between the HA-NL1FL mice and their controls (Fig. 7G, right). Consistent with the observed differences in likelihood to attack, the HA-NL1ΔC mice were also more likely to be submissive when pitted against group housed control mice in the dominance tube test (Fig. 7H, right). Overall, these results suggested that expression of HA-NL1ΔC resulted in a decrease in overt acts of aggression in addition to the lack of preference for social novelty, while overexpression of HA-NL1FL failed to yield significant differences in social interaction in our assays.

Overexpression of NL1FL is not necessary to maintain changes in synaptic maturation nor behavior, but can initiate changes in behavior in the adult

It is currently an open question as to whether NL1 levels at the synapse are required to maintain synapses in a mature state or whether they only initiate the cascade of events that bring about important changes at the synapse. Addressing this question would advance our understanding of when NL1 is most able to influence synaptic state and behavior. To examine this question, we characterized the consequences of transient

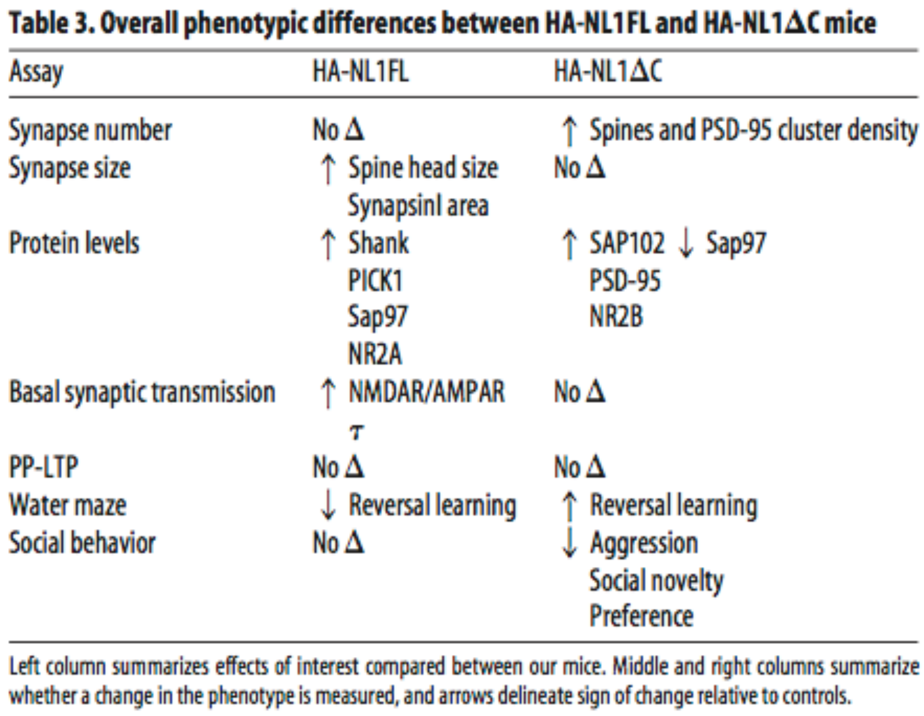

Table 3. Overall phenotypic differences between HA-NL1FL and HA-NL1ΔC mice

Assay	HA-NL1FL	HA-NL1ΔC
Synapse number	No Δ	↑ Spines and PSD-95 cluster density
Synapse size	↑ Spine head size Synapsinl area	No Δ
Protein levels	↑ Shank PICK1 Sap97 NR2A	↑ SAP102 ↓ Sap97 PSD-95 NR2B
Basal synaptic transmission	↑ NMDAR/AMPAR τ	No Δ
PP-LTP	No Δ	No Δ
Water maze	↓ Reversal learning	↑ Reversal learning
Social behavior	No Δ	↓ Aggression Social novelty Preference

Left column summarizes effects of interest compared between our mice. Middle and right columns summarize whether a change in the phenotype is measured, and arrows delineate sign of change relative to controls.

overexpression of full-length NL1 during development on adult synaptic state and behavior. In our transgenic mice, the capability to overexpress NL1 was regulated by the tTA genetic system, affording temporal control of transgene expression. We examined the synaptic and behavioral consequences when NL1FL was conditionally overexpressed once adulthood had already been reached. We previously demonstrated that constitutive

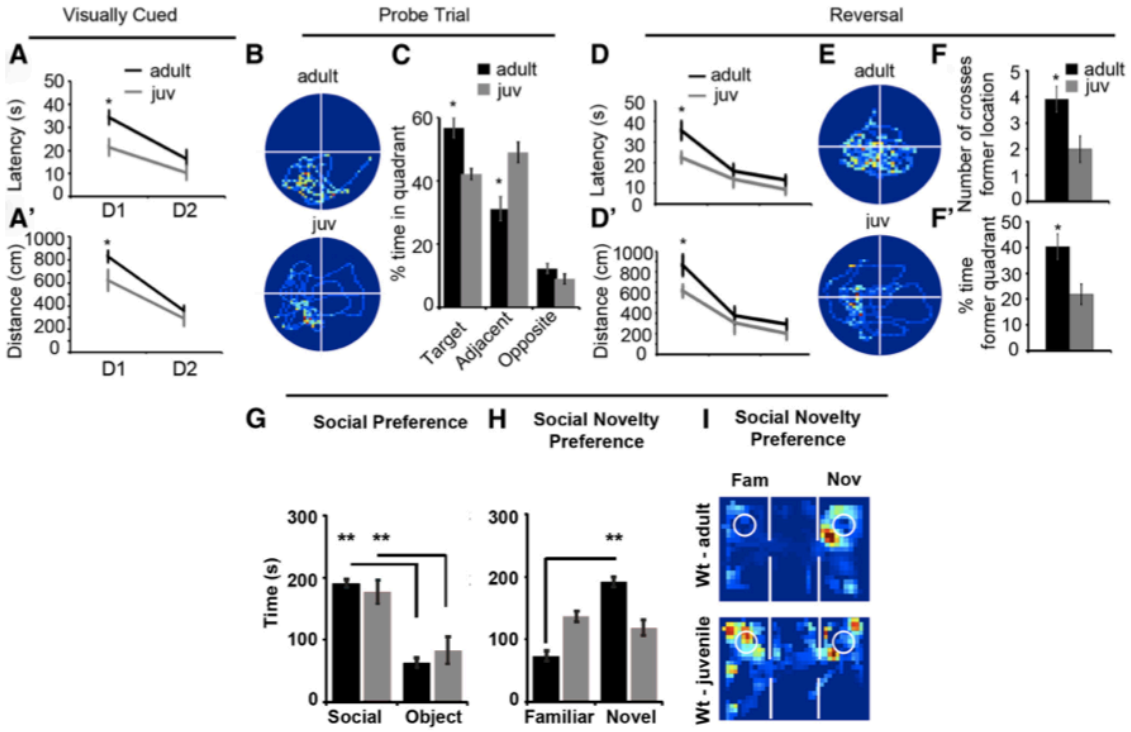

Figure 9. Learning, memory. and social behavior of wild-type juvenile mice. Water maze performance of 1-month-old wild-type Bl6 juvenile males (gray lines and bars) relative to their strain and sex matched adult controls (black lines and bars) for measures that we found significantly different in the HA-NL1ΔC mice: mean latency (A) and distance (A') of visually cued training, representative paths of probe trial (B), and percentage time spent in target quadrant (C), mean latency (D), and distance (D') during reversal training, representative paths, and number of crosses of former location (F) and percentage of time spent in former target quadrant (F'). All target quadrants have been aligned to place the target in the lower left quadrant. ***G–I,*** Wild-type adult social preferences (black) versus wild-type juvenile social preferences (gray). All data shown are mean ± SEM, significance determined with repeated-measures ANOVA with Tukey–Kramer HSD, *post hoc,* *$p < 0.05$, $n = 10$ pairs (10 juveniles and 10 adults).

overexpression of NL1 (from P10 to time of testing) inhibits learning and memory behavior in adult mice with the object recognition task (Fig. 6 I, J). Mice in which HA-NL1FL was overexpressed from P10 through 2 months of age, the Early OE mice (Fig. 8A), also displayed learning and recall deficits in the object recognition task when tested up to a month beyond returning NL1 expression to wild-type levels (Test 3: 51.28 ± 9.21% vs chance performance, $p > 0.05$; Fig. 8C). Western blots confirmed the absence of transgene expression after 1 week of Dox administration and at the time of behavioral testing (Fig. 8A'; see Materials and Methods). DiI labeling and characterization of spine morphology revealed that the average spine head area of the Early OEs was also significantly larger than those from littermate single positive controls ($p < 0.001$, Kolmogorov–Smirnov test; Fig. 8D). There were no significant differences in the number of spines per unit of dendrite length in the SLM of these mice ($p > 0.05$). These results suggest that NL1FL overexpression-induced maturation of synaptic structures and memory impairment was stable even when NL1 overexpression was removed.

We compared these results to those of mice where overexpression of full-length NL1 was inhibited until adulthood (Late OE). We confirmed that overexpression of HA-NL1FL was driven to levels similar to constitutive animals within 10 d of induction in the Late OE mice (Fig. 8B; see Materials and Methods). Remarkably, after only 28 d of transgene induction, we detected an effect on behavioral performance ($p < 0.01$; Fig. 8C). However, at this time point we did not detect a significant change in spine density, nor spine head area in the Late OE mice ($p > 0.05$; Fig. 8E). This suggests that NL1 is capable of initiating changes to synaptic function that impact behavior in the adult; but those changes occur without measurable changes in synaptic morphology. Together these data support the idea that overexpression of NL1 is not necessary to maintain decreased learning ability and enlarged synapses, but that the effects incurred earlier in development translate to lifelong changes in synaptic structure and behavior. Surprisingly, NL1 is sufficient to alter learning behavior and presumably synaptic function in the adult, without measurable changes in spine head size.

Flexibility in learning and memory tasks and lack of social preference are distinctly different in juveniles during normal development

Given that we had evidence that NL1 overexpression impacted processes in the juvenile phase of development, we sought to establish whether the changes in behavior that we observed in our transgenics could relate to how these behaviors normally matured. Therefore, we characterized wild-type juvenile performance in C57BL/6J mice relative to adult mice in the Morris water maze and social approach tasks. To our knowledge, this had not previously been characterized, and this information would help establish whether our genetic perturbations, and how they affected synaptic development, had any relevance to normal behavioral development in addition to pathological states. Twenty-eight-day-old mice were the youngest juveniles that were able to perform the water maze task without a significant difference in thigmotaxic behavior and swim speed relative to the adults (data not shown). We found a significant decrease in the latency and distance to reach the visually cued platform on the first day of visually cued training for the juveniles relative to adults (21.37 ± 3.60 s vs 34.26 ± 2.69 s, $p < 0.025$, *post hoc,* main effect of age on latency: $F_{(1,22)} = 8.2$, $p < 0.01$, main effect of day: $F_{(1,22)} = 18.92$, $p < 0.001$; Fig. 9A,A'). While it is difficult to know how improved performance on this phase of the task relates to learning and memory behaviors per se, it is nonetheless an interesting phenotype that appears to change over normal development.

We next observed key differences in behavior between adults and 28-d-old juveniles during probe trial performance and reversal training. Juveniles and adults both spent more time in the target quadrant than would be expected by chance, but significantly differed in their degree of preference (43.9 ± 2.9% vs 54.9 ± 3.3%, respectively, $p < 0.025$; Fig. 9 B, C). However, there were no differences between the juveniles and the adults in the number of crosses made over the former platform location during the 60s trial (4.3 ± 0.7 vs 5.0 ± 0.6, p > 0.05), nor was the distance to first cross the former target location different (48.21 ± 4.32 cm vs 55.21 ± 8.1 cm, $p > 0.05$). Thus, juveniles tended to occupy a greater area on the pool when searching during the probe trial. Juveniles also performed significantly different from adults during reversal training (main effect of age on latency: $F_{(1,36)} = 8.85$, $p < 0.01$, main effect of day: $F_{(2,36)} = 21.82$, $p < 0.001$, and no age x day interaction, $p > 0.05$). Twenty-eight-day-old mice located the new platform location significantly faster than their adult counterparts (22.45 ± 2.66 s vs 35.57 ± 4.42 s, $p < 0.05$; Fig. 9 D, D'), made fewer crosses of the former target location (2.00 ± 0.51 vs 3.90 ± 0.5, $p < 0.01$; Fig. 9F) and had lower dwell times in the former target quadrant (21.87 ± 4.39% vs 40.26 ± 5.08%, $p < 0.01$; Fig. 9F'). Overall, these results suggest that wild-type juvenile mice exhibit more flexibility in learning the water maze task and suggest that flexibility is a behavioral trait that undergoes developmental transitions.

Finally, we found that 28-d-old juvenile mice of the same background strain (C57BL/6J) lacked a preference for social novelty without lacking preference for social interaction as compared with adult mice (social vs object preference in juveniles: $p < 0.01$, familiar vs novel partner: $p > 0.05$; Fig. 9G–I). This suggests that complex features of social interaction also undergo important developmental transitions and it would be interesting to further explore how other developmental states and social contexts modulate this behavioral tendency.

Discussion

In this study, we explored the molecular, cellular, and behavioral phenotypes associated with regionally and temporally restricted NL1 overexpression. We contrasted that manipulation to one in which we overexpressed NL1 missing the last 55 aa within the C terminus (Table 3). This comparison was intended to provide insight into the molecular mechanisms by which NL1 affects synaptic structure and behavior relevant to both the normal development of mice, as well pathological states observed in humans with neurodevelopmental disorders. We present evidence that the NL1 C terminus is necessary for the induction of key features of synaptic maturation when NL1 is overexpressed *in vivo.* Moreover, we show for the first time that such molecular and cellular changes correlated with changes in flexibility in learning and memory, and, social preference. Importantly, we also provide novel evidence that these same behavioral traits change over normal development in mice. Thus, we link our specific NL1 manipulations to behaviors that are distinct at juvenile and mature phases of development. Finally, as flexibility in learning and memory and social preference are traits affected in ASD, we believe that our results have significant implications for our understanding of how NL1 relates to the etiology of pervasive neurodevelopmental disorders in addition to its roles during normal development.

Specific molecular targets are affected by our manipulations of NL1

At the cellular level, our studies found important differences between HA-NL1FL overexpression and that of HA-NL1ΔC. We discovered that HA-NL1FL overexpression resulted in a bias toward synapses with larger spine heads containing more Shanks, PICK1, SAP97, NR2A, and Synapsin1; these features are associated with mature synaptic structures (Fig. 2 *A, C,* 3 *A, E).* Recordings in CA1 showed that NL1FL overexpression drove an increase in the NMDAR to AMPAR ratio (Fig. 4A; Chubykin et al. 2007), presumably revealing more NMDARs in each large spine head. These results are consistent with previous studies of NL1FL overexpression *in vivo* (Dahlhaus et al. 2010) and suggest that overexpression of NL1FL leads to a reliable increase in specific molecular and structural features associated with mature synapses, in addition to a strong positive effect on NMDAR recruitment and function *in vivo.* The increase in NMDA/AMPA ratio was not associated with changes in the magnitude of NMDAR-dependent TBS LTP in animals assayed at the ages where behavior is observed. This is in contrast to the deficits observed in high-frequency stimulation LTP measured in mice with ubiquitous NL1 overexpression (Dahlhaus et al. 2010). This specific discrepancy can be explained by the significant differences in expression pattern between the two animal models and our choice to employ a TBS protocol (Capocchi et al. 1992; Larson and Lynch 1988; Larson et al. 1986). Although we did not find a deficit in TBS LTP induction at the perforant path, the difference in NMDAR to AMPAR ratio and the longer decay constant in the FL overexpressing mice might be expected to alter network dynamics and potentially alter information processing or encoding (Daw et al. 1993; Schiller and Schiller 2001). Our evidence will therefore direct future investigations toward understanding how alternative forms of plasticity and/or changes in basal NMDAR-mediated synaptic transmission in the adult are sufficient to account for the behavioral phenotypes described here. Additionally, we find evidence that NL1 shapes neural circuit function later in life via processes occurring earlier in development (Fig. 8). Therefore, future investigations of how NL1 function during the development of the hippocampus specifically affects later plasticity processes will provide additional understanding of how NL1 mechanistically supports changes in behavior.

In contrast, overexpression of HA-NL1ΔC generated a distinct set of synaptic consequences that were still related to a similar network of developmentally relevant postsynaptic scaffolding molecules and glutamate receptors. In the NL1ΔC mice, we observed an increase in the number of spines, decreased levels of Synapsin1 and SAP97, and increased levels of SAP102 and NR2B (Figs. 2 B, D, 3 B, D). Moreover, overexpression of this form of NL1 did not result in a significant change in NMDAR to AMPAR ratio (Fig. 4A). Therefore HA-NL1ΔC did not induce identical changes in molecular and cellular synaptic phenotypes. Since there were no significant differences in overexpression levels, or localization characteristics between HA-NL1FL and HA-NL1ΔC mice (Fig. 1), these results provide evidence that the induction of an abundance of mature synaptic features by the overexpression of HA-NL1FL required the last 55 aa of the molecule. This is one of the first accounts that this region of NL1 is required for these specific activities at the synapse.

Surprisingly, however, overexpression of NL1ΔC positively affected synapse number and at least two developmentally relevant synaptic molecules, SAP102 and NR2B (Petralia et al. 2005; Sans et al. 2003; van Zundert et al. 2004; Vicini et al. 1998; Washbourne et al. 2004; Zheng et al. 2011). While we may not completely rule out nonphysiological gain of function effects resulting from overexpressing HA-NL1ΔC, this manipulation does alter synaptic structure and biochemical composition in a manner predicted based on the molecular pathways that NL1 is known to specifically affect *in vivo* and *in vitro.* In particular, previous biochemical and cellular studies suggest that manipulations of NL would differentially affect SAP102 levels, which could in turn influence NR2B localization to synaptic structures, relative to other synaptogenic molecules (Meyer et al. 2004). Therefore, the molecular effects of HA-NL1ΔC overexpression are specific in the sense that they do not ubiquitously affect all postsynaptic excitatory molecules, and are restricted to the subset of effectors and receptors predicted to interact with NLs through the course of normal synaptic development (Blundell et al. 2010; Chubykin et al. 2007; Dahlhaus and El-Husseini 2010; Dahlhaus et al. 2010; Schapitz et al. 2010). Finally, at least three other recent studies have argued that under specific conditions where endogenous NL1 is removed, extracellular portions of the protein, and a novel domain within the intracellular tail region also perform important roles in NMDAR recruitment and synapse formation (Budreck et al. 2013; Shipman and Nicoll 2012; Shipman et al. 2011). This does not necessarily negate our conclusion that the last 55 aa also serve important roles at the synapse, especially in the context of an otherwise unaltered mouse. At least one region within the last 55 aa of NL1 is necessary to induce the overabundance of mature synaptic features when NL1FL is overexpressed because such structures cannot be induced via NL1ΔC overexpression in our studies (Table 1). Therefore, our study uniquely adds to this growing body of work as we provide the first evidence that abnormal levels of different regions of this protein differentially impact developmentally relevant aspects of behavior in mice.

Notably, we now show important ways that NL1FL and NL1ΔC overexpression differs from that of SynCAM1 (Robbins et al. 2010). SynCAM1 is a distinct synaptogenic CAM that modulates distinct downstream targets (Meyer et al. 2004). First, targeted NL1FL overexpression did not strongly increase the number of synapses in the adult while SynCAM1 overexpression does. Second, NL1 alters the NMDAR/AMPAR ratio, changing basal synaptic transmission. SynCAM1 overexpression does not. Third, NL1FL overexpression appears to alter learning and memory behavior to a lesser extent than SynCAM1. SynCAM1 overexpressing adult mice are unable to learn to find the hidden platform efficiently. Fourth, and possibly most intriguingly, we find that the consequences of transient NL1 overexpression in the younger animal persist into adulthood in mice, while SynCAM1 must be maintained at synapses to affect synapse number. Importantly, Robbins et al., (2010) used the same CaMKII-tTA expression system. Therefore, this novel data support the idea that the overexpression of these molecules distinctly perturbs synapse number, function, and maturation, and are relevant at different developmental phases.

Distinct manipulations of NL1 differentially perturb behavior

If we consider behavioral changes as a whole, then there are clear quantitative differences in how the HA-NL1FL and HA-NL1ΔC perform in learning, memory, and social behaviors. We first consider differences in performance during the water maze task. The HA-NL1FL mice show clear deficits in initially reaching the hidden platform in the most efficient manner relative to all other groups, and trend toward less time in the target quadrant during the probe trial than control groups (Fig. 6 B, D). Careful consideration of simultaneously measured parameters during the probe trial additionally suggests that HA-NL1FL mice significantly differ from HA-NL1ΔC mice. Of particular note, HA-NL1ΔC spend significantly more time in the opposite quadrant over the probe trial, while the HA-NL1FL mice distribute their searching behavior between the target and directly adjacent quadrants (Fig. 6D). Importantly, HA-NL1ΔC-expressing mice showed a significantly higher number of crosses and a shorter distance to first cross the former platform location. This is quite the opposite of the behavior observed in the HA-NL1FL animals. These data support that HA-NL1ΔC mice did not display learning and memory deficits per se; rather, they displayed decreased perseverance in searching the target quadrant during the probe trial. This argues that differences between these groups of mice relate to systems that implement flexibility of search strategy as opposed to pure memory per se (Fig. 6C). The differences in the reversal data (Fig. 6F–H), as well as the fact that the HA-NL1ΔC mice are quicker to reach a visually cued platform without significant changes in their basic locomotor behavior (Fig. 6 A, A',K), all point to robust, yet differential, changes in flexibility between the two lines of mice. Indeed, other research groups have similarly argued for the need to consider that differences in persistent searching behavior during the reversal component of the water maze task could point to changes in behavioral flexibility in using stored information (Arque et al. 2008; Brown and Kraemer 1997; Dolleman-van der Weel et al. 2009; Izquierdo and Jentsch 2012; Janus 2004; McKirdy et al. 2009; Vorhees and Williams 2006). Because of the significant quantitative differences we observed in behavior in the water maze between the two groups, we conclude that overexpressing HA-NL1FL distinctly impacted learning, memory, and flexibility in behavior as compared with when HA-NL1ΔC was overexpressed to similar levels.

Finally, social interaction behaviors are also affected differentially between the groups of mice. We are unable to detect significant changes in social approach or aggression in mice overexpressing HA-NL1FL (Fig. 7 A, G). This dissociates our observed molecular and cellular changes within targeted regions from significant alterations to these aspects of this behavioral domain. However, other work suggests that more complicated aspects of social interaction such as normal vocal behavior could still be impacted via manipulations to downstream targets such as Shank3 that we may have modulated by HA-NL1FL overexpression (Bozdagi et al. 2010). Interestingly, overexpression of HA-NL1ΔC significantly affected both aggression and social preference (Fig. 7D–F,H). Together, these behavioral data argue that important behavioral differences exist between our two transgenic lines.

These manipulations model synaptic changes and behaviors relevant to neurodevelopmental disease

It is still unclear how differences in synaptic development may alter learning, memory and social behaviors that are relevant to those affected in human neurodevelopmental disorders. However, previous investigations of NL family function *in vivo* suggested links between the cellular processes governed by NLs and these complex behavioral domains (Blundell et al. 2010; Dahlhaus and El-Husseini 2010; Hines et al. 2008; Jamain et al. 2008). Additional work shows that *in vivo* manipulations of the scaffolding molecules that we show are positively regulated by NL1 overexpression yields pathologically relevant changes in learning, memory, and social behavior in mice, changes reminiscent of developmental disorders (Bangash et al. 2011; Bozdagi et al. 2010; Hung et al. 2008; Kim and Sheng 2004; Peca et al. 2011; Poglia et al. 2011). Thus, forced recruitment of such scaffolding molecules by NL1FL overexpression are likely to have been related to the observed behavioral changes described here.

There is an association between ASDs and incidence of copy number variation (CNV) of the postsynaptic molecules we find modulated here (Glessner et al. 2009).

Additionally, mutations in NL1's 3' region have also been implicated in ASD (Ylisaukko-oja et al. 2005). The 3' mutations are found in introns close to the end of the coding sequence corresponding to the intracellular region. Furthermore, targeted HA-NL1FL overexpression in our studies led to decreases in flexibility in learning and memory behaviors. This contrasted a surprising enhancement in flexibility and social preference in HA-NL1ΔC overexpressing mice. Indeed, the behavioral data gathered on HA-NL1ΔC mice bore remarkable similarities to those traits exhibited by typically developing juvenile mice across multiple behavioral domains relevant to neurodevelopmental disorders (Fig. 9). This specific data argue that it will be important in future studies to consider how the changes in synaptic state induced by the overexpression of HA-NL1ΔC led to juvenile-like tendencies in these aspects of behavior. The data considered as a whole, in conjunction with known mutations associated with ASDs, speak to the relevance of both the NL1FL and NL1ΔC overexpressing mice as animal models of the biological etiology of changes in flexibility associated with neurodevelopmental disorders.

Importantly for future considerations of potential gene therapies to overcome genetic forms of ASD, our results suggest that NL1 overexpression (or CNV), resulting in learning and memory deficits, cannot be reversed by knockdown in the adult (Fig. 8C). This implies that there may be an early critical period for RNAi-based interventions in these cases. In contrast, the ability of exogenous NL1 to drive learning and memory deficits, implying the induction of synaptic changes in the adult (Fig. 8C), suggests that null mutations in NL1 may be overcome by viral-based expression of a NL1 transgene even in the mature nervous system, as has been shown for NL3 (Baudouin et al. 2012). These observations may pave the way to identifying critical periods of gene therapy-based interventions for NL1-dependent and other forms of nonsyndromic ASD.

Together, this set of studies validates the role of NL1-mediated processes in the maturation of complex behaviors, and hones in on the molecular pathways that may specifically regulate flexibility in such behaviors. Furthermore, our results validate the idea that NL1 intracellular signaling domains regulate late stages of synaptic maturation *in vivo,* and provide the first evidence, that artificially manipulating the relative proportion of glutamatergic synapses in one state versus another *in vivo,* within specific neural systems, alters behavioral traits that change as a function of development.

APPENDIX B

TRANSGENIC SILENCING OF NEURONS IN THE MAMMALIAN BRAIN BY EXPRESSION OF THE ALLATOSTATIN RECEPTOR (ALSTR)

Reproduced with permission from Wehr M, Hostick U, Kyweriga M, Tan A, Weible AP, Wu H, Wu W, Callaway EM, Kentros C. Transgenic silencing of neurons in the mammalian brain by expression of the Allatostatin receptor (AlstR). *J Neurophysiol* 102: 2554-2562, 2009. (Corrigendum. *J Neurophysiol* 102: 3781-3781, 2009).

Abstract

The mammalian brain is an enormously complex set of circuits composed of interconnected neuronal cell types. The analysis of central neural circuits will be greatly served by the ability to turn off specific neuronal cell types while recording from others in intact brains. Because drug delivery cannot be restricted to specific cell types, this can only be achieved by putting "silencer" transgenes under the control of neuron-specific promoters. Towards this end we have created a line of transgenic mice putting the *Drosophila* allatostatin (AL) neuropeptide receptor (AlstR) under the control of the tetO element, thus enabling its inducible expression when crossed to tet-transactivator lines. Mammals have no endogenous AL or AlstR, but activation of exogenously expressed AlstR in mammalian neurons leads to membrane hyperpolarization via endogenous G-protein-coupled inward rectifier K^+ channels, making the neurons much less likely to fire action potentials. Here we show that this tetO/AlstR line is capable of broadly expressing

AlstR mRNA in principal neurons throughout the forebrain when crossed to a commercially available transactivator line. We electrophysiologically characterize this cross in hippocampal slices, demonstrating that bath application of AL leads to hyperpolarization of CA1 pyramidal neurons, making them refractory to the induction of action potentials by injected current. Finally, we demonstrate the ability of AL application to silence the sound-evoked spiking responses of auditory cortical neurons in intact brains of AlstR/tetO transgenic mice. When crossed to other transactivator lines expressing in defined neuronal cell types, this AlstR/tetO line should prove a very useful tool for the analysis of intact central neural circuits.

Introduction

The mammalian nervous system is composed of innumerable different neurons, each connected to thousands of other neurons. Communication between neurons is critically dependent on neurotransmitter release triggered by action potentials, which in turn depend on the membrane potential. Thus one can "silence" neurons by preventing the membrane potential from rising, effectively removing them from the circuit. The neuron-specific expression of silencer transgenes should enable investigators to perform circuit analysis of the intact mammalian brain: recording from one circuit element (i.e., neuronal cell type) before and after "shorting out" another one.

Toward this end, we have created and characterized a line of transgenic mice [called allatostatin (AL) neuropeptide receptor (AlstR)/tetO] capable of expressing one such neuronal silencer, the allatostatin receptor (AlstR) under the control of the tetO element. The AL receptor is an invertebrate neuropeptide receptor (Birgul et al. 1999) developed by Callaway and colleagues for use as a silencer of mammalian neurons (Lechner et al. 2002). When expressed in mammalian neurons, AlstR is capable of activating G-protein-coupled inward rectifier K^+ (GIRK) channels, nearly ubiquitous K^+ channels that provide strong outward currents at subthreshold voltages (Gosgnach et al. 2006). GIRK activation thus serves to keep the membrane from depolarizing above threshold, thereby inhibiting action potentials. Because mammals do not have anything similar to the AL neuropeptide or its receptor, application of AL to the brains of intact animals should specifically turn off only those neurons that express the AlstR transgene.

The tetO element is part of the two-part system developed by Bujard and colleagues (Mansuy and Bujard 2000) to provide temporal control of transgene expression by combining elements of the bacterial tetracycline resistance operon with a viral transactivator. This two-part system involves crossing a transactivator line expressing the tTA fusion protein (also called “tet-off,” or its converse, rtTA or “tet-on”) from a cell-specific promoter to a “payload” line expressing a transgene under the control of the bacterial tetO promoter element. Wherever the tTA transgene is expressed, the expression of the transgenic payload can be controlled by the presence or absence of doxycycline in the animals’ diet. Because the AlstR silencer transgene is activated by a ligand, the temporal control afforded by the tetO/tTA system is of secondary importance. The key feature of this system for our purposes is its modularity: a tetO silencer line can be crossed to any tTA (or rtTA) line to take advantage of whatever anatomical specificity it may afford.

Here we describe the creation of a tetO/AlstR line via pronuclear injection of mouse oocytes and demonstrate its ability to specifically express mRNA for the AlstR silencer transgene in many regions of the forebrain when crossed to a commercially available tTA line. We then use in vitro patch-clamp recordings in the hippocampal slice preparation to show functional silencing of CA1 pyramidal cells. Finally, we demonstrate the utility of the line for in vivo electrophysiology in intact brains by reversibly silencing the responses of neurons in the primary auditory cortex to auditory stimuli. We expect these mice will lead to an enormous amount of information about the functional roles of the various elements comprising the circuitry of the mammalian brain when distributed to the scientific community and crossed to other transactivator lines that express only in defined sets of CNS neurons.

Methods

Construct generation

The plasmid AlstR_pBMN was cut with *HindIII* and *XbaI* to generate a fragment containing the entire AL receptor coding sequence. This fragment was directionally ligated into the polylinker of the pTRE-tight plasmid (Clontech, Mountain View, CA). The resulting pTRE-AlstR plasmid was cut with *XhoI* to yield our injection construct (Fig. 1) consisting of the Ptight promoter, the full-length coding sequence of AlstR mRNA, and an SV40 polyadenylation site. *Ptight* is a modified tetracycline response element (TREmod) consisting of seven direct repeats of a 36-bp sequence that contains the 19-bp tet operator sequence (tetO) and the minimal CMV promoter (PminCMVΔ),

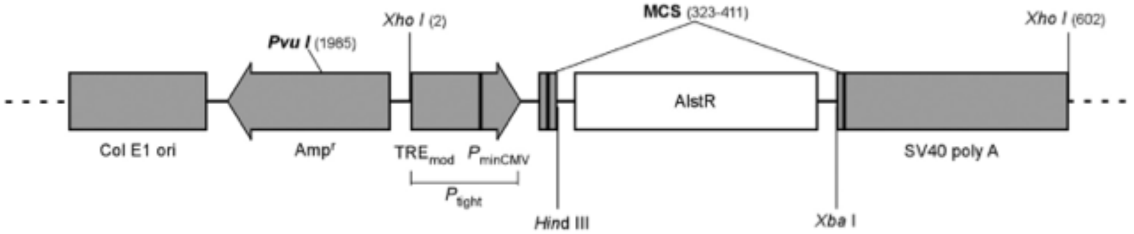

Fig. 1. Injection construct for the generation of allatostatin (AL) neuropeptide receptor (AlstR)/tetO mice. The cDNA encoding the AlstR transgene was excised with *BamHI* and *XbaI* and ligated into the multiple cloning site of the pTRE-tight vector (Clontech). The resulting plasmid was cut with *XhoI* to yield a fragment containing the pTRE element driving the entire coding sequence of the allatostatin receptor followed by the SV40 polyadenylation site. The 2 pairs (inner and outer) of genotyping primers used were OF: 5'-CACTGGAAACGGTAGTATC-3'; OR: 5'-CGTGACTCTGCGGAAGG-3'; IF: 5'-GGATCACAATGCCAACGAC-3'; IR: 5'-CAGATCTCCTCCTCCGTG-3'.

which lacks the enhancer part of the complete CMV promoter. Consequently, *Ptight* is thought to be transcriptionally silent in the absence of binding of tTA or rtTA to the *tetO* sequences. The same *HindIII/XbaI* fragment was ligated into pBluescript to make antisense riboprobes for nonradioactive in situ hybridization.

Animals and genotyping

The preceding construct was injected into B6D2F1 oocytes (due to their relative ease of transgenesis) by the Trangenic Mouse Facility at the University of Oregon. Pups were then evaluated for transgene incorporation via PCR of genomic DNA isolated from tail biopsies (see Fig. 1 legend for genotyping primer sets). Because B6D2F1 is the F1 generation of a cross between C57BL/6J and DBA/2J, founders should ideally be backcrossed to C57BL/6J for at least five successive generations to obtain a more homogeneous genetic background. The animals described here have not yet been back-crossed enough generations to be considered congenic C57BL/6J, although these matings are ongoing. The reason for this is because not every genotypically positive founder line necessarily expresses transgene; we first tested for expression by crossing mice from each line to a commercially available transactivator line that expresses tTA in the forebrain from the CamKIIα promoter [B6; CBA-Tg(Camk2a-tTA)1Mmay/J mouse; Jackson Laboratories, strain 003010, Bar Harbor, ME]. We then used in situ hybridization (ISH) to test whether genotypically double-positive (for both tetO-AlstR and tTA) individuals actually expressed AlstR mRNA in the forebrain. Finally, we used in vitro hippocampal and in vivo cortical electrophysiology to test whether expression led to functional silencing. Only then did we know whether a given line was worth backcrossing, and indeed, only one of the seven founders turned out to pass all of these tests. Only after all this did we know that the line was worth back-crossing to C57Bl6J. All procedures were in strict accordance with the National Institutes of Health guidelines as approved by the University of Oregon Animal Care and Use Committee.

In situ hybridization and anatomical analysis

Animals were anesthetized with a lethal dose of pentobarbital (50 mg/kg) and perfused transcardially with freshly made 4% paraformaldehyde in phosphate-buffered saline (PBS). Following craniotomy, brains were postfixed in the perfusion solution overnight at 4°C and then kept in 30% sucrose at 4°C until the brains no longer floated (typically 16–24 h). Brains used for slice electrophysiology were hemisected, and hemispheres not used for recordings were placed directly in the postfix solution and then otherwise treated identically. Cryostat sections (30 µm) were affixed to microscope slides, air-dried, and kept at -80°C until needed. Room temperature sections were covered with 0.3 ml of hot (62°C) hybridization solution (50% formamide, 10% dextran sulfate, 1x Denhardt's solution, 1 mg/ml rRNA, 1x SSC in DEPC-treated H_2O), fitted with a coverslip, and hybridized over-night in a humidity chamber at 62°C.

Nonradioactive in situ hybridization was performed using a digoxygenin-labeled riboprobe at an estimated concentration of 0.0125 µg/µl visualized by anti-digoxygenin sheep Fab fragments conjugated to horseradish peroxidase (Roche No. 11207733907). The riboprobe was a 746-bp transcript using T7 RNA polymerase in the presence of dig-labeled nucleotides using the pBlu-AlstR construct linearized with *PstI* as template. Sections were washed 3x 30' at 62°C in wash buffer (50% Formamide, 0.5x SSC, 0.1% Tween-20), then 3x 30' at room temperature in MABT (1x maleic acid, 20% Tween-20). Slides were then incubated in blocking solution (MABT + 20% sheep serum + 2% blocking reagent, Roche No. 11096176001) for 3 h. The alkaline phosphatase-linked anti-digoxygenin antibody was then added, and the slices incubated at RT overnight. The slices were then washed at RT with MABT buffer 5 x 5' and then AP staining buffer (0.1 M NaCl, 50 mM MgCl2, 10% polyvinyl alcohol 100,000–150,000 MW, 0.1 M Tris-HCl, pH 9.5), 2 x 10', after which 3.5 µl/ml NBT and 2.6 µl/ml BCIP, and 80 µl/ml levamisole were added, and the colorimetric reaction was allowed to develop for 3–7 h at 37°C under agitation, then stopped by washing twice with PBS (.1% Tween-20), then twice in DI H_2O. Slides were then dehydrated in graded ethanols and mounted with Permount.

Hippocampal slice electrophysiology

Mice were anesthetized with isofluorane and rapidly decapitated. The brain was rapidly removed, and slices from the left middle third of the hippocampus were cut using a vibrating microtome (VT 1000s; Leica Instrument, Leitz, Nussloch, Germany) into 300 μm thickness in ice-cold artificial cerebrospinal fluid (ACSF) of the following composition (in mM): 119 NaCl, 26 $NaHCO_3$, 2.5 KCl, 1 $NaH_2PO_4*H_2O$, 1.3 $MgCl_2*6H_2O$, 2 $CaCl_2*2H_2O$, and 25 dextrose (saturated with carbogen). Slices recovered in the oxygenated ACSF at 35°C for 30 min, then maintained at room temperature for ≥1 h prior to recording. Experiments were performed at room

---

Fig. 2 (Next page). AL receptor-associated mRNA expression was observed in principal neurons throughout the forebrain. The most striking exception to this expression pattern was the complete lack of expression in neu- rons of the thalamus. *A:* AlstR mRNA-expressing neurons were observed in visual (V1) and somatosensory (S1BF) cortices, the entorhinal cortex (MEnt), and components of the amygdalar complex (CxA, BMP, AHi, PMCo). *B:* AlstR mRNA-expressing neurons were observed, in addition to the aforementioned regions, in the piriform cortex (Pir), olfactory tubercle (Tu), dorsal endopiriform cortex (DEn), subiculum (Sub), and retrospenial cortex (RSC). *C:* AlstR mRNA-expressing neurons were observed, in addition to the aforementioned regions, in the granule cell layer of the olfactory bulb (GrO), accumbens (Acb), nucleus of the lateral olfactory tract (LOT), and components of the amygdalar complex (AAV, AHiPM, MeA, MePV). *D:* AlstR mRNA-expressing neurons were observed, in addition to the aforementioned regions, in components of the olfactory system (AOL, LO) and the claustrum (Cl). mRNA expression was completely absent in thalamic nuclei (e.g., DLG, MGD, Po, VPM) as well as in the cerebellum (e.g., Crus1). *E:* AlstR mRNA-expressing neurons were observed, in addition to the aforementioned regions, in the anterior cingulate cortex (CG1, CG2), indusium griseum (IG), and the lateral septum (LS). *F:* AlstR mRNA-expressing neurons were observed, in addition to the aforementioned regions, in the retrosplenial cortex (RSA, RSG), components of the ventral hypothalamus (VH), and components of the amygdalar complex (BLA, BMP, BLV, PMCo, PLCo). aca: anterior commissure, anterior; acp: anterior commissure, posterior; cc: corpus callosum; fmj: forceps major; opt: optic tract; rf: rhinal fissue. 1x photomicrographs illustrate whole coronal and sagittal sections. Outlines (gray) indicate locations of 5x photomicrograph composites.

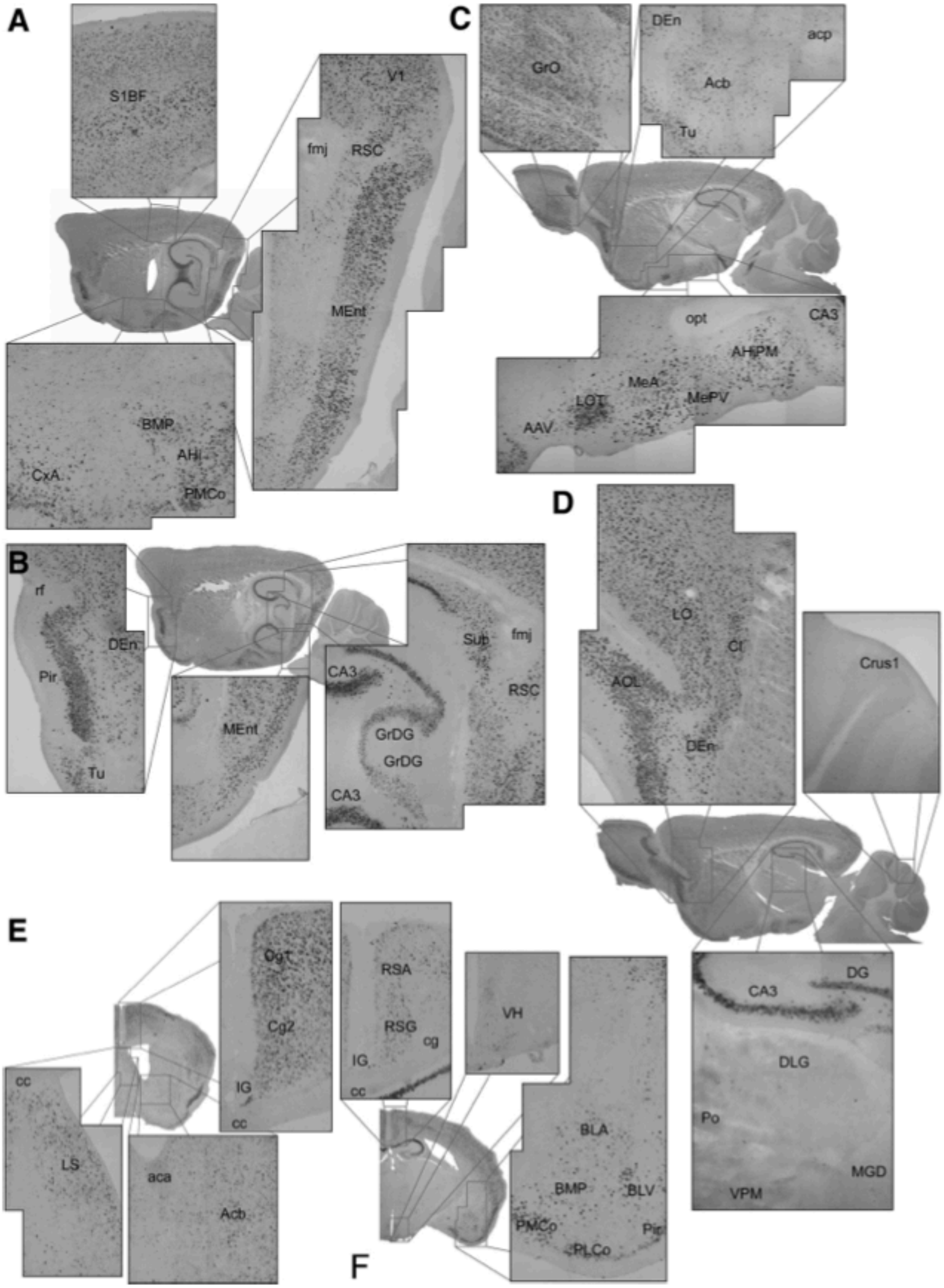
A
S1BF
V1
fmj
RSC
MEnt
BMP
AHi
CxA
PMCo
B
rf
DEn
Pir
Tu
MEnt
Sub
fmj
RSC
CA3
GrDG
GrDG
CA3
C
GrO
DEn
acp
Acb
Tu
opt
CA3
AHiPM
MeA
LOT
MePV
AAV
D
LO
Cl
AOL
DEn
Crus1
CA3
DG
DLG
Po
MGD
VPM
E
cc
LS
aca
Acb
Cg1
Cg2
IG
cc
F
RSA
RSG
cg
IG
cc
VH
BLA
BMP
BLV
PMCo
Pir
PLCo

TABLE 1. *Regional distribution of AlstR mRNA*

Category	Region	Cell Density	Expression
Sensory Cortices	L2,3	Dense	Mod
	L4	Dense	Light
	L5	Dense	Dark
	L6	Dense	Mod
Motor Cortex	L2,3	Dense	Light
	L5	Dense	Mod
	L6	Sparse	Light
Amygdalar	CxA	Dense	Dark
	ACo	Dense	Dark
	BLA	Mixed	Light
	BLP	Mixed	Light
	BMA	Mixed	Light
	BMP	Dense	Mod
	PLCo	Dense	Mod
	AHi	Dense	Dark
	PMCo	Dense	Mod
	AAV	Sparse	Light
	MePD	Dense	Light
	LOT	Dense	Dark
Striatum	CPu	Dense	Light
	LAcbSh	Mixed	Light
	AcbSh	Mixed	Light
	AcbC	Mixed	Light
Hippocampal Formation	CA1,3	Dense	Dark
	DG	Dense	Light
	FC	Dense	Dark
	Sub	Dense	Dark
	PrS	Dense	Light
	PaS	Dense	Dark
	MEn	Dense	Dark
Agranular Insular Ctx	L2,3	Dense	Light
	L4	Dense	Mod
	L5	Dense	Dark
	L6	Dense	Mod
Retrosplenial Ctx	L2,3	Dense	Light
	L5	Dense	Mod
	L6	Sparse	Light
Anterior Cingulate Ctx	L2,3	Dense	Mod
	L5	Dense	Mod
	L6	Dense	Light
Lateral Orbital Ctx		Mixed	Light
Piriform Ctx		Dense	Dark
Olfactory Structures	Tu	Dense	Dark
	AOL	Mixed	Dark
	AOV	Dense	Dark
	EPI	Dense	Dark
	GI	Dense	Dark
	AOB	Dense	Dark
	AOD	Dense	Mod
	AOE	Dense	Mod
Cholinergic System	VDB	Sparse	Mod
	SI	Sparse	Light
	LS	Dense	Light
Other Structures	CI	Dense	Dark
	DEn	Dense	Dark
	SNR	Sparse	Dark
	DpMe	Sparse	Mod
	IG	Dense	Dark
	VHN	Sparse	Light

CxA, cortex-amygdala transition zone; ACo, anterior cortical amygdaloid nucleus; BLA, basolateral anterior amygdala; BLP, basolateral posterior amygdala.

temperature. Slices were transferred to a small volume (<0.5 ml) recording chamber mounted on a fixed-stage, upright microscope (Axioskop FS2; Carl Zeiss, Thornwood, NY) equipped with infrared differential interference contrast (IR-DIC) optics. The recording chamber was continuously superfused with carbogen-saturated ACSF flowing at a rate of ~2 ml/min. Whole cell patch-clamp recordings were performed on visually identified CA1 pyramidal neurons. Patch electrodes were pulled from filamented, thick-walled borosilicate glass pipettes (BF150-86-10, Sutter Instruments, Novato, CA) and heat-polished to a resistance of 2~3 MΩ when filled with the following internal solutions (in mM): 140 $KMeSO_4$, 10 KCl, 10 HEPES, 2 Mg_2ATP , 0.4 Na_3GTP, and 10 Tris-phosphocreatine; pH adjusted to 7.25 with KOH; final osmolarity ~290 mosM. Whole cell patch–clamp recordings were obtained from CA1 pyramidal cells using a Multiclamp 700A amplifier (Molecular Devices, Sunnyvale, CA), digitized using an Digidata 1440A analog–to–digital converter (Molecular Devices), and transferred to a computer using pClamp10 software (Molecular Devices). Experiments were performed in the presence of SR95531 (5 μM), CGP55845 (2.5 μM), 6-cyano-7-nitroquinoxalene-2,3-dione (CNQX, 25 μM), and d-2-amino-5-phosphonopentanoic acid (D-AP5, 50 μM) to block $GABA_A$, $GABA_B$, AMPA, and *N-methyl-D-aspartate* (NMDA) receptors, respectively. Current-clamp recordings were performed to assess the membrane properties of CA1 pyramidal neurons in control ACSF followed by bath application of AL (5 nM). Input resistance was measured with a series of hyperpolarizing current steps in 20-pA decrements. IE of the neurons was characterized with a series of depolarizing current steps in 25-pA increments. Solutions and channel blockers: SR95531, CGP55845, CNQX, and D-AP5

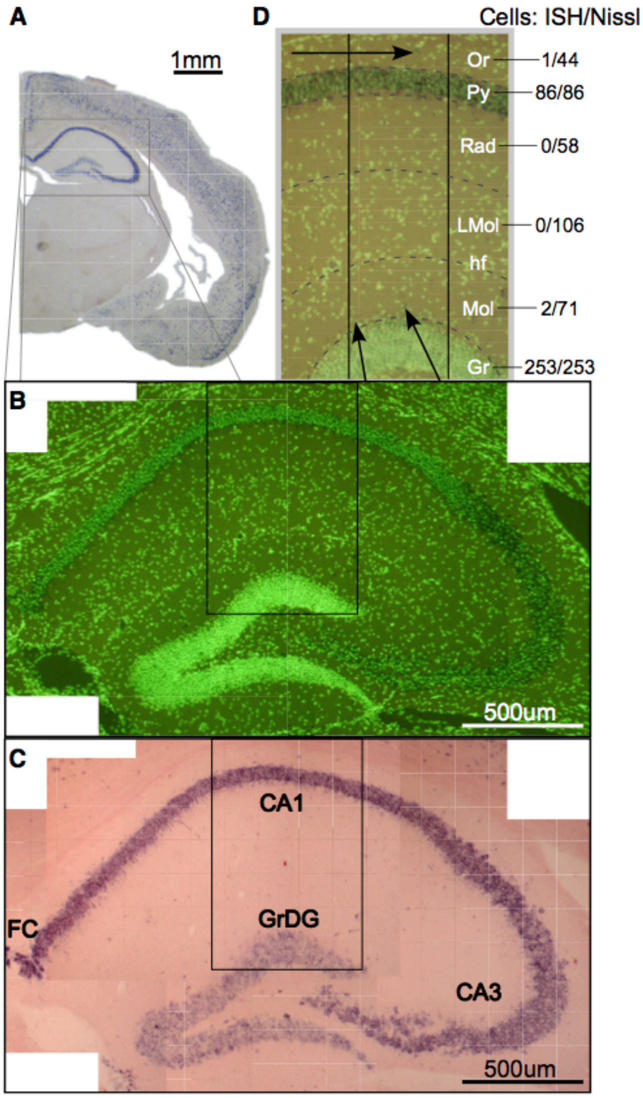

Fig. 3. Robust penetrance of allatostatin receptor-associated mRNA was observed in principal neurons of the hippocampus in contrast to an almost complete lack of receptor-associated mRNA in hippocampal interneurons. *A:* 1X bright-field photomicrograph of a coronal section from the hemisphere opposite that used for in vitro characterization of silencing resulting from bath-application of AL. *B:* a composite of 10x dark-field photomicrographs illustrating fluorescent Nissl labeling in the hippocampus. The composite corresponds to the rectangular outline illustrated in *A*. *C:* a composite of 10x bright-field photomicrographs illustrating mRNA labeling of principal neurons in cornu ammonis 1 and 3 (CA1 and CA3, respectively), granule cells of the dentate gyrus (GrDG), and fasciola cinereum (FC). *D:* a magnified view of the rectangular region identified in *B* and *C* illustrating a semi-transparent view of fluorescent Nissl labeling overlain on the corresponding view of mRNA expression. Numbers in *D* indicate the number of soma co-expressing AlstR-associated mRNA and fluorescence (numerator) compared with the total count of fluorescing cells (denominator). hf: hippocampal fissue; LMol: lacunosum moleculare; Mol: molecular layer; Or: stratum oriens; Rad: stratum radiatum.

were purchased from Tocris Cookson (Ballwin, MO); AL peptide (Ser-Arg-Pro-Tyr-Ser-Phe-Gly-Leu-NH2) synthesized by Biomatik LLC, Wilmington, DE. All other drugs were purchased from Sigma (St. Louis, MO). CGP55845 was dissolved as a stock solution in DMSO. When used, the final concentration of DMSO was always <0.1%.

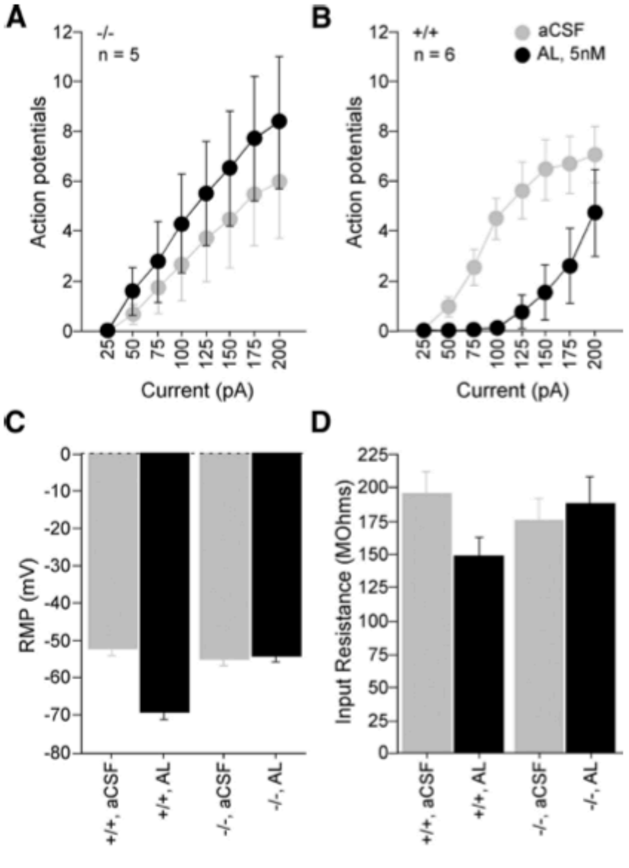

Fig. 4. A and B: AL significantly decreased intrinsic membrane excitability in neurons from +/+ (B) but not -/- (A) mice as evidenced by the increase in the number of action potentials elicited across a range of depolarizing current injections. Black represents recordings acquired in control artificial cerebrospinal fluid (ACSF); red represents recordings acquired following bath application of AL. *C* and *D:* consistent with G-protein-coupled inward rectifier K+ (GIRK) activation, bath application of AL significantly hyperpolarized the membrane (C) and reduced the resting input resistance (D) of CA1 pyramidal neurons from +/+ mice only.

In vivo electrophysiology

We recorded from the left primary auditory cortex of anesthetized [(in mg/kg)120 ketamine, 0.24 medetomidine, 3 acepromazine) mice aged 3–3.5 mo. Recordings were made from well-tuned regions of auditory cortex (as determined by the frequency-amplitude tuning properties of multi-unit spiking responses and local field potentials), which probably correspond to cortical areas A1, AAF, or A2 (Linden et al. 2003). Subpial depth of recordings ranged from 330 to 435 μm, as determined from micromanipulator travel. For multi-unit recordings we used 1–2 MΩ tungsten electrodes amplified with an A-M Systems 1800 extracellular amplifier and band-pass filtered from 300–5000 Hz). 10 μM AL (Biomatik) in saline, or saline (0.9% NaCl) was continually superfused at a rate of 0.1–0.3 ml/min to the cortical surface. We used a pseudo-randomly interleaved stimulus array consisting of nine intensities of white noise bursts, linearly spaced from 0 to 80 dB SPL, with 25-ms duration, 3-ms 10–90% cosine-squared ramps, and a 500-ms interstimulus interval. We thresholded multiunit activity at a fixed voltage threshold for each recording site, which was set to 5 SDs of the extracellular voltage for the first measurement protocol for each site. We quantified spiking responses by counting spikes in a 100 ms window following sound onset. Recording sites for which spiking responses permanently increased or decreased during the recording, and did not recover, were excluded from analysis (n = 3 mice). In addition, at the end of each recording, we verified that the recording depth matched the distance traveled to return to the cortical surface; sites for which these two distances differed by >50 μm were excluded from analysis (n = 2 mice).

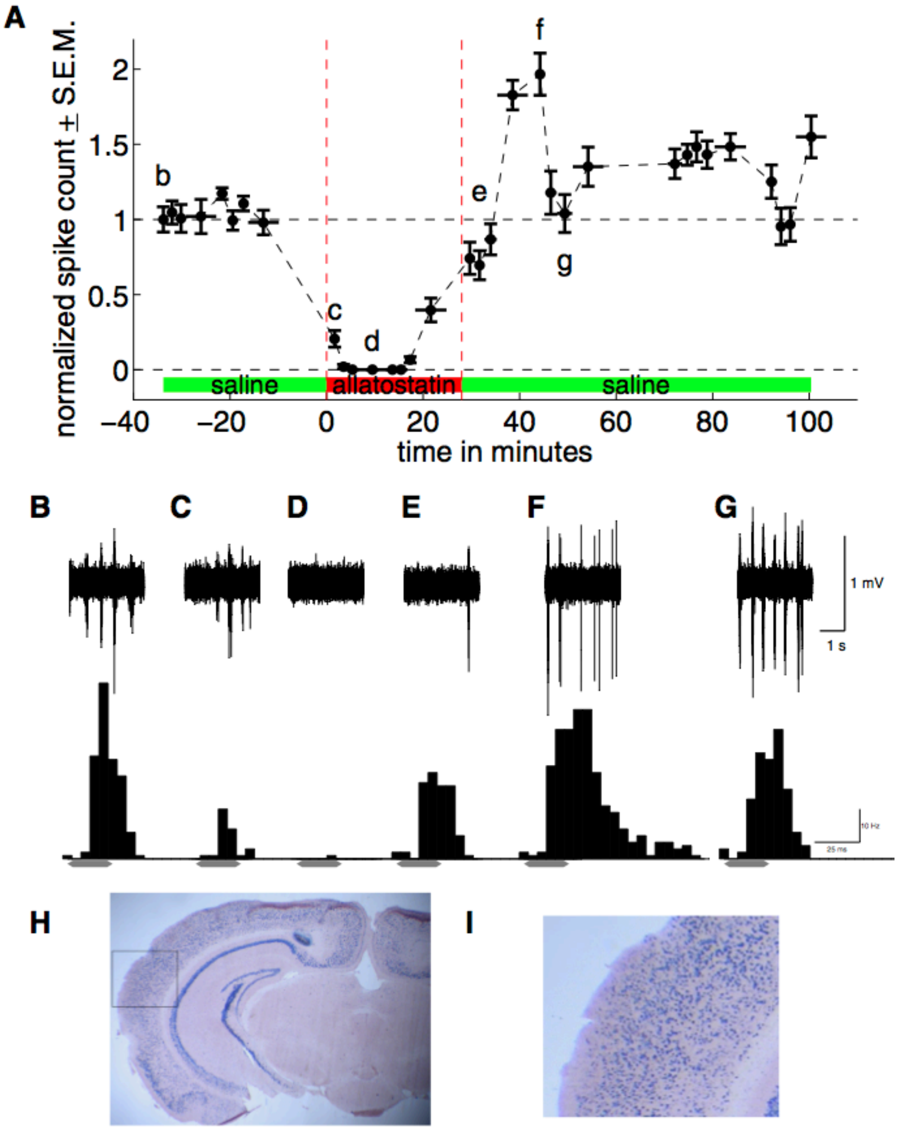

Fig. 5. A: Multiunit spiking responses to white noise bursts (70 dB SPL, 25 ms) before, during, and after 10 μM AL application. Recordings are from middle layers of primary auditory cortex. Each dot is the spike count (mean ± SE, *n* = 20 repetitions) in a 100-ms window following sound onset. The horizontal line for each dot indicates the duration of each stimulus protocol. Responses are normalized to the first measurement in the series. Note that spiking responses are markedly diminished within ~2 min and completely silenced shortly thereafter. Note also that evoked responses began to recover even before the end of AL application and showed a rebound effect after ~10 min of saline application. *B–G, top row:* extracellular voltage waveforms at each of the time points indicated in *A*. White noise bursts (interleaved intensities) were delivered at a rate 2/s. *Bottom row:* post-stimulus time histograms at the same time points (70 dB bursts). Gray bar: sound presentation. *H* and *I:* photomicrographs of AlstR mRNA in situ hybridization of a coronal slice from the brain of this mouse. Primary auditory cortex is located in the boxed region, which is expanded in *I.*

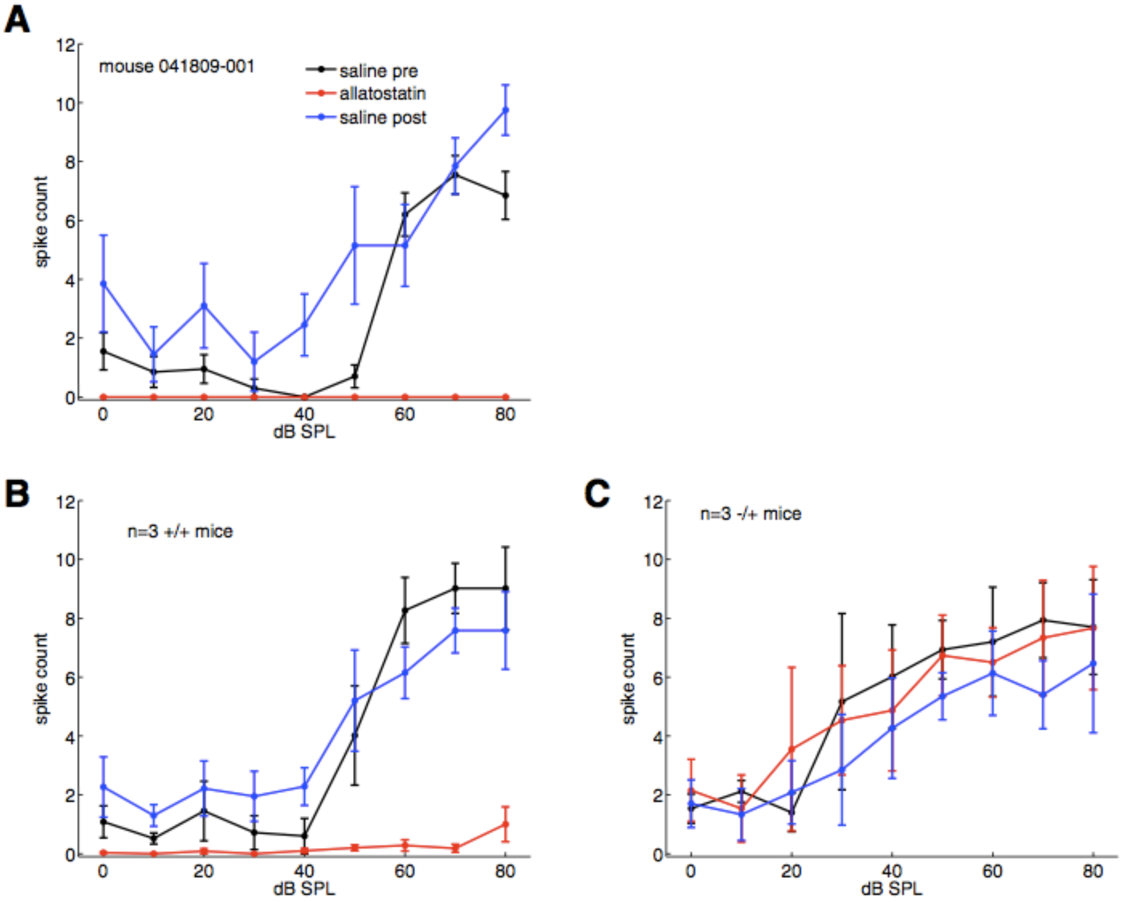

Fig. 6. A: Multiunit spiking responses to white noise bursts across a range of stimulus intensities (0–80 dB SPL). Each dot is the spike count (mean ± SE, *n* = 20 repetitions) in a 100-ms window following sound onset. Same recording site and animal as Fig. 1. Black line represents saline superfusion 35 min prior to allatostatin; red line represents 12 min after start of AL superfusion; blue line represents 19 min after start of 2nd saline superfusion. Note that spiking responses were silenced even at the highest stimulus intensities used (80 dB SPL). *B:* multiunit spiking responses across the same stimulus intensities in 3 +/+ mice (error bars indicate SE with *n* = 3 mice). Responses during AL (red line) were recorded at maximal silencing (12, 5, and 2 min after start of AL application). *C:* multiunit spiking responses across the same stimulus intensities, in 3 -/+ or -/- mice (n = 3 mice).

Results

Figure 1 shows our injection construct consisting of the AL receptor coding sequence under the control of a modified tetO element (pTRE-Tight, Clontech). Our injections yielded seven distinct founder lines, six of which transmitted genotypically. All lines were then mated to a commercially available line expressing tTA from the CamKIIα promoter to check whether they were capable of driving AlstR expression in the forebrain. Only one of the lines (AlstR/tetO) was found to express significant levels of AlstR mRNA. Luckily, as shown in Fig. 2, this line expressed AlstR mRNA in all major brain areas that this tTA line has been shown to drive transgene expression (Mayford et al. 1996). As expected, the pattern of AlstR expression (Table 1) is quite similar to the distribution of the alpha subunit of calmodulin-dependent kinase II (αCamKII) (Liu and Jones 1996) , the promoter used to drive tTA expression in this cross.

To determine the degree of penetrance of transgene expression (i.e., what percentage of cells of a certain type express the transgene), we compared cell counts of in situ results with the AlstR probe with Nissl stains (see Fig. 3). We concentrated on the hippocampus proper because the cell types are relatively well characterized there, sidestepping the quite involved task of defining cell types throughout the forebrain. We superimposed the Nissl stain with the in situ to count how many nuclei in the various layers of the hippocampus were positive for the AlstR mRNA. The results are shown in Fig. 3D, and although the quantitation may slightly exaggerate positive neurons in stratum pyramidale because the strong colorimetric signal spreads somewhat there, essentially all of the primary neurons (CA1 and CA3 pyramidal neurons and, to a lesser extent, dentate granule neurons) express AlstR mRNA. Consistent with both the native expression patterns of CamKIIα (Liu and Jones 1996) and prior work with this tTA line (Mayford et al. 1996), few if any interneurons express the transgene (as judged by the low ratio of positive neurons outside of stratum pyramidale). Thus the AlstR/tetO line appears to be able to strongly express AlstR mRNA in primary neurons throughout the forebrain.

However, the most important aspect of the AlstR/tetO line is its ability to functionally silence the neurons it is expressed in. Because of the strong AlstR mRNA expression in hippocampal pyramidal neurons (see Fig. 3), we used in vitro whole cell patch-clamp methods to record from CA1 neurons in hippocampal slices (Fig. 4). The current-clamp configuration was used to minimize complications of space clamp. Figure 4A shows that bath application of 5 nM AL to wild-type slices has no significant effect on the ability of known amounts of somatically injected current to drive spiking of the neurons (if anything, the trend is toward a requirement for less current during AL application). However, as seen in Fig. 4B, slices made from double (tTA and tetO)-positive animals require more than twice as much current to get similar amounts of action potentials in the presence of AL. Consistent with the induction of GIRK channel activity, AL application also hyperpolarized the membrane (Fig. 4C) and decreased its input resistance.

To test whether the transgenic expression of AlstR can silence neurons in the intact brain, we obtained multi-unit responses to auditory stimuli from the middle layers of auditory cortex in ketamine-anesthetized mice. We measured the spiking responses to brief bursts of white noise during continuous superfusion of the cortical surface with saline, then switched to superfusion with 10 μM AL solution and then back to saline. Within 1–2 min of AL application, spiking responses were strongly diminished (Fig. 5A) and were completely silenced in ~3 min. The first measurement began 46 s after the start of AL application and was completed 110 s later; the second measurement began 160 s after AL and was completed in 100 s. Because no spikes were evoked during the second measurement, this suggests that complete silencing occurred within 160 s. After switching back to saline superfusion, responses rapidly recovered to baseline levels and then increased to nearly two-fold greater than baseline levels for ~10 min. The suppression of spiking responses during AL application was effective across the entire range of stimulus intensities tested (0–80 dB SPL, Fig. 6A) for all three +/+ mice we successfully tested (Fig. 6B) but not for three littermate controls (either +/- or -/- mice), which showed no effect of AL at the population level.

While these data are entirely consistent with complete, rapid and reversible silencing of sound-evoked responses in the mice expressing AlstR in auditory cortex, there are some interesting deviations from this straightforward interpretation that warrant further investigation. Most notably, in all three +/+ mice, we observed a partial recovery of sensory-evoked responses within ~20 min despite continued superfusion of AL. In addition, the animal shown in Fig. 5 demonstrated hyperexcitability following saline washout (Fig. 5F). Both of these phenomena could be explained either by cell-autonomous mechanisms such as receptor desensitization or homeostatic plasticity or network phenomena such as a gradual reduction in steady-state inhibition. Future experiments, ideally involving in vivo whole cell recordings, will be required to determine the nature of these phenomena.

Discussion

Transgenic technologies arguably have the potential to revolutionize systems neurophysiology much as the advent of the slice preparation revolutionized the cellular neurophysiology of the mammalian brain in the 1960s (Skrede and Westgaard 1971) previously dominated by recordings from intact brains. Beyond simply increasing yield, the hippocampal slice preparation (and other reduced preparations) basically brought cellular specificity to the neurophysiological study of local circuits in the mammalian brain. In the slice, one can place extracellular electrodes with sufficient accuracy to evoke and record specific synaptic potentials and with the advent of differential interference contrast techniques (Dodt and Zieglgansberger 1990) directly visualize the specific neurons one records from. This enables the investigation of the electrophysiological properties of specific neuronal cell types. Moreover, reduced preparations greatly streamline pharmacological manipulations, facilitating the investigation of the molecular bases of observed physiological phenomena.

However, these enormous advantages come at great cost: typically only the most local of circuits remain intact in reduced preparations. Thus in vivo recordings in intact brains are required to study the neural processing of information in the mammalian CNS at the systems level. However, it is extremely difficult to distinguish between diverse classes of neurons with in vivo recordings and even more difficult to manipulate specific classes of neurons. The promise of mouse molecular genetics for systems neurophysiology comes from its potential to provide something approaching the access and specificity afforded by the slice preparation to recordings from intact brains, ideally even in freely behaving animals. The AlstR/tetO line of mice presented here should aid in this goal by providing the means to express a ligand-gated silencer transgene in specific populations of CNS neurons.

There are two key requirements for the successful application of transgenics to the functional analysis of neural circuits: transgene expression needs to be limited to a defined set of neurons and the functional consequences of transgene expression in a given neuron must be electrophysiologically unambiguous. The tetO/AlstR line presented here has utility on both counts. We chose to use a tTA line that broadly expresses in forebrain neurons to facilitate the characterization of our tetO/ AlstR line, but many other cell-specific transactivator (tTA or rtTA) lines that these mice could be crossed with have already been described (Chen et al. 1998; Nakashiba et al. 2008; Ralph et al. 2000; Yasuda and Mayford 2006) and more are surely forthcoming. The modularity of the tTA/ tetO system is thereby one of the line's major strengths. Each different cross could yield distinct and interesting results because silencing of neuronal cell types mainly probes circuit-level function, which may well be unique to each circuit. Recent experiments showing the change in the network properties of the spinal cord when AlstR is expressed in a particular set of spinal motoneurons by a recombinase-based approach (Gosgnach et al. 2006) provide an excellent illustration of the promise of these techniques, and the extensive silencing of auditory-evoked multi-unit responses demonstrated here bodes well for AlstR's efficacy in other parts of the intact brain. Tools such as these are likely to be of considerable use in addressing questions at multiple levels of analysis, including cellular, local circuit, systems, perception, and behavioral, as they are in essence very selective molecular lesions with a granularity approaching that of the nervous system.

The silencing of neuronal activity described here is unambiguous. AL application in +/+ mice completely abolished spiking activity in auditory cortex neurons. However, reversing the effect in vivo was not as straightforward as previously seen with this silencer (Tan et al. 2006) for reasons that may be biologically interesting (i.e., it may have to do with which specific subsets of cortical neurons express the transgene). We observed the first signs of recovery of neuronal activity prior to washout. In a subset of animals, we also saw hyperexcitability after washout, which declined over time back toward baseline. These results suggest that silencing and subsequent restoration of neuronal activity may show complex dynamics in vivo. This is perhaps not surprising given the complexity of cortical circuits and the homeostatic mechanisms that regulate their activity. However, it is worth noting that these interesting dynamics may more accurately portray what happens in vivo following disruption or damage to a discrete neural locus.

Our technique adds to a growing arsenal of genetically encoded systems designed to selectively and reversibly perturb the activity of specific neuronal populations in vivo. Each of these systems has considerable merit, and one may be more appropriate than another depending on the specific application (Tervo and Karpova 2007). Two systems involve the expression of nonmammalian transmitter receptors that hyperpolarize neurons, either directly (the ionotropic GluCl system; Lerchner et al. 2007) or indirectly (the AlstR system) (Lechner et al. 2002). The onset and recovery of GluCl silencing take 1 and 4 days, respectively, which may be ideal for learning and other behavioral paradigms but may be too slow for reversibly silencing neurons when using most electrophysiological recording techniques. The time course of the AlstR system may be better suited for electrophysiology but requires that the targeted neurons express endogenous GIRK channels. AL also does not cross the blood brain barrier, whereas the GluCl ligand does. Because both systems act by hyperpolarization, they may be overwhelmed by strong synaptic drive, although we observed complete or near-complete silencing even for strong sensory stimuli (80 dB white noise bursts, see Fig. 6). A system that does not act by hyperpolarization is molecular inactivation of synaptic transmission (MIST), which instead involves the dimerization of modified synaptic proteins using an exogenous cell-permeable dimerizer. This system may therefore achieve silencing regardless of the strength of synaptic drive and indeed has been demonstrated to rapidly (~20 min) and reversibly block synaptic transmission in vitro and to affect behavior in vivo (Karpova et al. 2005). All of these systems require the application of a ligand (either systemically or intracerebrally); the advantage of rhodopsin-based systems is that they are instead activated by light. Channelrhodopsin-2 is a light-gated cation channel that has received much attention for its ability to optically stimulate neurons with exquisite temporal precision and reliability (Aravanis et al. 2007; Boyden et al. 2005; Huber et al. 2008; Lima et al. 2009; Tsai et al. 2009). Optical silencing of neurons using the halorhodopsin system, which activates a chloride pump, offers similarly impressive temporal precision (Zhang et al. 2007; Zhao et al. 2008). Optical silencing, however, requires optical access to the neurons in question. Surface illumination may work for superficial neurons, but deep structures require the use of fiber optics, with tissue scattering and absorption limiting the effective range to ~1.4 mm from the fiber tip (Aravanis et al. 2007). As with local application of silencer ligands, this can be advantageous if locally restricted silencing is desirable or can be a serious limitation if the desired target population is widely distributed. The unique advantages and limitations of each of these systems are good news for neuroscientists, as an ever-expanding toolbox is much more likely to provide the right tool for the job.

The functional consequences of AlstR activation are particularly unambiguous from an electrophysiological perspective. It is reversible, its effects can be quantitated relatively easily, and its time frame is fast enough following AL application to do the before-and-after experiments so critical for circuit-level questions. A potential issue is that because AlstR recruits endogenous GIRK channels, the target neurons must express GIRK channels to be silenced. Fortunately, these are relatively ubiquitous in the mammalian CNS (Del Burgo et al. 2008; Ponce et al. 1996) and are clearly sufficient to silence the firing of CNS neurons, both in our hands and that of others (Gosgnach et al. 2006). There are lingering questions such as whether AlstR-induced activation of G-protein-mediated cascades does more than simply activate GIRK or indeed what the longer-term ramifications of sustained GIRK activation are. However, these can perhaps best be thought of as interesting questions in their own right that should not interfere with the immediate circuit-level manipulation of turning off specific neurons. Thus assuming the continuing generation of specific transactivator lines, these animals should enable a multitude of experiments that all ask the same basic question: what happens to the rest of the system when you remove *these* neurons?

REFERENCES CITED

Ahmed MS, and Siegelbaum SA. Recruitment of N-Type Ca2+ Channels during LTP Enhances Low Release Efficacy of Hippocampal CA1 Perforant Path Synapses. *Neuron* 63: 372-385, 2009.

Altshuler MW, and Comalli PE. Effect of stimulus intensity and frequency on median horizontal plane sound localization. *Journal of Auditory Research* 15: 262-265, 1975.

Amaral DG, Schumann CM, and Nordahl CW. Neuroanatomy of autism. *Trends in Neurosciences* 31: 137-145, 2008.

Aravanis AM, Wang L-P, Zhang F, Meltzer LA, Mogri MZ, Schneider MB, and Deisseroth K. An optical neural interface: in vivo control of rodent motor cortex with integrated fiberoptic and optogenetic technology. *Journal of Neural Engineering* 4: S143-S156, 2007.

Arnott SR, and Alain C. The auditory dorsal pathway: orienting vision. *Neurosci Biobehav Rev* 35: 2162-2173, 2011.

Arque G, Fotaki V, Fernandez D, Martinez de Lagran M, Arbones ML, and Dierssen M. Impaired Spatial Learning Strategies and Novel Object Recognition in Mice Haploinsufficient for the Dual Specificity Tyrosine-Regulated Kinase-1A (Dyrk1A). *PLoS One* 3: 2008.

Bangash MA, Park JM, Melnikova T, Wang D, Jeon SK, Lee D, Syeda S, Kim J, Kouser M, Schwartz J, Cui Y, Zhao X, Speed HE, Kee SE, Tu JC, Hu J-H, Petralia RS, Linden DJ, Powell CM, Savonenko A, Xiao B, and Worley PF. Enhanced Polyubiquitination of Shank3 and NMDA Receptor in a Mouse Model of Autism (Retracted article. See vol. 152, pg. 367, 2013). *Cell* 145: 758-772, 2011.

Barrow SL, Constable JRL, Clark E, El-Sabeawy F, McAllister AK, and Washbourne P. Neuroligin I: a cell adhesion molecule that recruits PSD-95 and NMDA receptors by distinct mechanisms during synaptogenesis. *Neural Development* 4: 2009.

Barry PH. JPCalc, a software package for calculating liquid junction potential corrections in patch-clamp, intracellular, epithelial and bilayer measurements and for correcting junction potential measurements. *J Neurosci Methods* 51: 107-116, 1994.

Baudouin SJ, Gaudias J, Gerharz S, Hatstatt L, Zhou K, Punnakkal P, Tanaka KF, Spooren W, Hen R, De Zeeuw CI, Vogt K, and Scheiffele P. Shared Synaptic Pathophysiology in Syndromic and Nonsyndromic Rodent Models of Autism. *Science* 338: 128-132, 2012.

Bevins RA, and Besheer J. Object recognition in rats and mice: a one-trial non-matching-to-sample learning task to study 'recognition memory'. *Nature Protocols* 1: 1306-1311, 2006.

Birgul N, Weise C, Kreienkamp HJ, and Richter D. Reverse physiology in Drosophila: identification of a novel allatostatin-like neuropeptide and its cognate receptor structurally related to the mammalian somatostatin/galanin/opioid receptor family. *Embo Journal* 18: 5892-5900, 1999.

Blundell J, Blaiss CA, Etherton MR, Espinosa F, Tabuchi K, Walz C, Bolliger MF, Suedhof TC, and Powell CM. Neuroligin-1 Deletion Results in Impaired Spatial Memory and Increased Repetitive Behavior. *Journal of Neuroscience* 30: 2115-2129, 2010.

Bourgeron T. A synaptic trek to autism. *Current Opinion in Neurobiology* 19: 231-234, 2009.

Boyden ES, Zhang F, Bamberg E, Nagel G, and Deisseroth K. Millisecond-timescale, genetically targeted optical control of neural activity. *Nat Neurosci* 8: 1263-1268, 2005.

Bozdagi O, Sakurai T, Papapetrou D, Wang X, Dickstein DL, Takahashi N, Kajiwara Y, Yang M, Katz AM, Scattoni ML, Harris MJ, Saxena R, Silverman JL, Crawley JN, Zhou Q, Hof PR, and Buxbaum JD. Haploinsufficiency of the autism-associated Shank3 gene leads to deficits in synaptic function, social interaction, and social communication. *Molecular Autism* 1: 2010.

Brown RW, and Kraemer PJ. Ontogenetic differences in retention of spatial learning tested with the Morris water maze. *Developmental Psychobiology* 30: 329-341, 1997.

Budreck EC, Kwon O-B, Jung JH, Baudouin S, Thommen A, Kim H-S, Fukazawa Y, Harada H, Tabuchi K, Shigemoto R, Scheiffele P, and Kim J-H. Neuroligin-1 controls synaptic abundance of NMDA-type glutamate receptors through extracellular coupling. *Proceedings of the National Academy of Sciences of the United States of America* 110: 725-730, 2013.

Burton SD, Johnson JW, Zeringue HC, and Meriney SD. DISTINCT ROLES OF NEUROLIGIN-1 AND SYNCAM1 IN SYNAPSE FORMATION AND FUNCTION IN PRIMARY HIPPOCAMPAL NEURONAL CULTURES. *Neuroscience* 215: 1-16, 2012.

Campbell RA, Schnupp JW, Shial A, and King AJ. Binaural-level functions in ferret auditory cortex: evidence for a continuous distribution of response properties. *J Neurophysiol* 95: 3742-3755, 2006.

Capocchi G, Zampolini M, and Larson J. THETA-BURST STIMULATION IS OPTIMAL FOR INDUCTION OF LTP AT BOTH APICAL AND BASAL DENDRITIC SYNAPSES ON HIPPOCAMPAL CA1 NEURONS. *Brain Research* 591: 332-336, 1992.

Chadderton P, Agapiou JP, McAlpine D, and Margrie TW. The synaptic representation of sound source location in auditory cortex. *J Neurosci* 29: 14127-14135, 2009.

Chang EF, Bao SW, Imaizumi K, Schreiner CE, and Merzenich MM. Development of spectral and temporal response selectivity in the auditory cortex. *Proceedings of the National Academy of Sciences of the United States of America* 102: 16460-16465, 2005.

Chen JS, Kelz MB, Zeng GQ, Sakai N, Steffen C, Shockett PE, Picciotto MR, Duman RS, and Nestler EJ. Transgenic animals with inducible, targeted gene expression in brain. *Molecular Pharmacology* 54: 495-503, 1998.

Chih B, Engelman H, and Scheiffele P. Control of excitatory and inhibitory synapse formation by neuroligins. *Science* 307: 1324-1328, 2005.

Chubykin AA, Atasoy D, Etherton MR, Brose N, Kavalali ET, Gibson JR, and Suedhof TC. Activity-dependent validation of excitatory versus inhibitory synapses by neuroligin-1 versus neuroligin-2. *Neuron* 54: 919-931, 2007.

Comoletti D, De Jaco A, Jennings LL, Flynn RE, Gaietta G, Tsigelny I, Ellisman MH, and Taylor P. The Arg451Cys-neuroligin-3 mutation associated with autism reveals a defect in protein processing. *Journal of Neuroscience* 24: 4889-4893, 2004.

Dahlhaus R, and El-Husseini A. Altered neuroligin expression is involved in social deficits in a mouse model of the fragile X syndrome. *Behavioural Brain Research* 208: 96-105, 2010.

Dahlhaus R, Hines RM, Eadie BD, Kannangara TS, Hines DJ, Brown CE, Christie BR, and El-Husseini A. Overexpression of the Cell Adhesion Protein Neuroligin-1 Induces Learning Deficits and Impairs Synaptic Plasticity by Altering the Ratio of Excitation to Inhibition in the Hippocampus. *Hippocampus* 20: 305-322, 2010.

Daw NW, Stein PSG, and Fox K. THE ROLE OF NMDA RECEPTORS IN INFORMATION-PROCESSING. *Annual Review of Neuroscience* 16: 207-222, 1993.

de Villers-Sidani E, Chang EF, Bao SW, and Merzenich MM. Critical period window for spectral tuning defined in the primary auditory cortex (A1) in the rat. *Journal of Neuroscience* 27: 180-189, 2007.

Del Burgo LS, Cortes R, Mengod G, Zarate J, Echevarria E, and Salles J. Distribution and neurochemical characterization of neurons expressing GIRK channels in the rat brain. *Journal of Comparative Neurology* 510: 581-606, 2008.

DeWeese MR, Wehr M, and Zador AM. Binary spiking in auditory cortex. *J Neurosci* 23: 7940-7949, 2003.

Dodt HU, and Zieglgansberger W. VISUALIZING UNSTAINED NEURONS IN LIVING BRAIN-SLICES BY INFRARED DIC-VIDEOMICROSCOPY. *Brain Research* 537: 333-336, 1990.

Dolleman-van der Weel MJ, Morris RGM, and Witter MP. Neurotoxic lesions of the thalamic reuniens or mediodorsal nucleus in rats affect non-mnemonic aspects of watermaze learning. *Brain structure & function* 213: 329-342, 2009.

Dresbach T, Neeb A, Meyer G, Gundelfinger ED, and Brose N. Synaptic targeting of neuroligin is independent of neurexin and SAP90/PSD95 binding. *Molecular and Cellular Neuroscience* 27: 227-235, 2004.

Duncan GE, Moy SS, Perez A, Eddy DM, Zinzow WM, Lieberman JA, Snouwaert JN, and Koller BH. Deficits in sensorimotor gating and tests of social behavior in a genetic model of reduced NMDA receptor function. *Behavioural Brain Research* 153: 507-519, 2004.

Fu ZY, Washbourne P, Ortinski P, and Vicini S. Functional excitatory synapses in HEK293 cells expressing neuroligin and glutamate receptors. *Journal of Neurophysiology* 90: 3950-3957, 2003.

Fuzessery ZM, Wenstrup JJ, and Pollak GD. Determinants of horizontal sound location selectivity of binaurally excited neurons in an isofrequency region of the mustache bat inferior colliculus. *J Neurophysiol* 63: 1128-1147, 1990.

Gherri E, Driver J, and Eimer M. Eye movement preparation causes spatially-specific modulation of auditory processing: new evidence from event-related brain potentials. *Brain Res* 1224: 88-101, 2008.

Gilman SR, Iossifov I, Levy D, Ronemus M, Wigler M, and Vitkup D. Rare De Novo Variants Associated with Autism Implicate a Large Functional Network of Genes Involved in Formation and Function of Synapses. *Neuron* 70: 898-907, 2011.

Glessner JT, Wang K, Cai G, Korvatska O, Kim CE, Wood S, Zhang H, Estes A, Brune CW, Bradfield JP, Imielinski M, Frackelton EC, Reichert J, Crawford EL, Munson J, Sleiman PMA, Chiavacci R, Annaiah K, Thomas K, Hou C, Glaberson W, Flory J, Otieno F, Garris M, Soorya L, Klei L, Piven J, Meyer KJ, Anagnostou E, Sakurai T, Game RM, Rudd DS, Zurawiecki D, McDougle CJ, Davis LK, Miller J, Posey DJ, Michaels S, Kolevzon A, Silverman JM, Bernier R, Levy SE, Schultz RT, Dawson G, Owley T, McMahon WM, Wassink TH, Sweeney JA, Nurnberger JI, Jr., Coon H, Sutcliffe JS, Minshew NJ, Grant SFA, Bucan M, Cook EH, Jr., Buxbaum JD, Devlin B, Schellenberg GD, and Hakonarson H. Autism genome-wide copy number variation reveals ubiquitin and neuronal genes. *Nature* 459: 569-573, 2009.

Gosgnach S, Lanuza GM, Butt SJB, Saueressig H, Zhang Y, Velasquez T, Riethmacher D, Callaway EM, Kiehn O, and Goulding M. V1 spinal neurons regulate the speed of vertebrate locomotor outputs. *Nature* 440: 215-219, 2006.

Grothe B, Pecka M, and McAlpine D. Mechanisms of sound localization in mammals. *Physiol Rev* 90: 983-1012, 2010.

Heffner HE, Heffner RS, Contos C, and Ott T. Audiogram of the hooded Norway rat. *Hear Res* 73: 244-247, 1994.

Heffner RS. Primate hearing from a mammalian perspective. *Anat Rec A Discov Mol Cell Evol Biol* 281: 1111-1122, 2004.

Higgins NC, Storace DA, Escabi MA, and Read HL. Specialization of binaural responses in ventral auditory cortices. *J Neurosci* 30: 14522-14532, 2010.

Higley MJ, and Contreras D. Balanced excitation and inhibition determine spike timing during frequency adaptation. *J Neurosci* 26: 448-457, 2006.

Hines RM, Wu L, Hines DJ, Steenland H, Mansour S, Dahlhaus R, Singaraja RR, Cao X, Sammler E, Hormuzdi SG, Zhuo M, and El-Husseini A. Synaptic imbalance, stereotypies, and impaired social interactions in mice with altered neuroligin 2 expression. *Journal of Neuroscience* 28: 6055-6067, 2008.

Hirsch JA, and Martinez LM. Circuits that build visual cortical receptive fields. *Trends Neurosci* 29: 30-39, 2006.

Hromadka T, Deweese MR, and Zador AM. Sparse representation of sounds in the unanesthetized auditory cortex. *PLoS Biol* 6: e16, 2008.

Huber D, Petreanu L, Ghitani N, Ranade S, Hromadka T, Mainen Z, and Svoboda K. Sparse optical microstimulation in barrel cortex drives learned behaviour in freely moving mice. *Nature* 451: 61-U67, 2008.

Hung AY, Futai K, Sala C, Valtschanoff JG, Ryu J, Woodworth MA, Kidd FL, Sung CC, Miyakawa T, Bear MF, Weinberg RJ, and Sheng M. Smaller dendritic spines, weaker synaptic transmission, but enhanced spatial learning in mice lacking Shank1. *Journal of Neuroscience* 28: 1697-1708, 2008.

Hutsler JJ, and Zhang H. Increased dendritic spine densities on cortical projection neurons in autism spectrum disorders. *Brain Research* 1309: 83-94, 2010.

Huttner WB, Schiebler W, Greengard P, and Decamilli P. SYNAPSIN-I (PROTEIN-I), A NERVE TERMINAL-SPECIFIC PHOSPHOPROTEIN .3. ITS ASSOCIATION WITH SYNAPTIC VESICLES STUDIED IN A HIGHLY PURIFIED SYNAPTIC VESICLE PREPARATION. *Journal of Cell Biology* 96: 1374-1388, 1983.

Iida J, Hirabayashi S, Sato Y, and Hata Y. Synaptic scaffolding molecule is involved in the synaptic clustering of neuroligin. *Molecular and Cellular Neuroscience* 27: 497-508, 2004.

Imig TJ, and Adrian HO. Binaural columns in the primary field (A1) of cat auditory cortex. *Brain Res* 138: 241-257, 1977.

Insel TR, and Fernald RD. How the brain processes social information: Searching for the social brain. *Annual Review of Neuroscience* 27: 697-722, 2004.

Irvine DR, and Gago G. Binaural interaction in high-frequency neurons in inferior colliculus of the cat: effects of variations in sound pressure level on sensitivity to interaural intensity differences. *J Neurophysiol* 63: 570-591, 1990.

Isaacson JS, and Scanziani M. How inhibition shapes cortical activity. *Neuron* 72: 231-243, 2011.

Izquierdo A, and Jentsch JD. Reversal learning as a measure of impulsive and compulsive behavior in addictions. *Psychopharmacology* 219: 607-620, 2012.

Jamain S, Quach H, Betancur C, Rastam M, Colineaux C, Gillberg IC, Soderstrom H, Giros B, Leboyer M, Gillberg C, Bourgeron T, and Paris Autism Res Int Sibpair S. Mutations of the X-linked genes encoding neuroligins NLGN3 and NLGN4 are associated with autism. *Nature Genetics* 34: 27-29, 2003.

Jamain S, Radyushkin K, Hammerschmidt K, Granon S, Boretius S, Varoqueaux F, Ramanantsoa N, Gallego J, Ronnenberg A, Winter D, Frahm J, Fischer J, Bourgeron T, Ehrenreich H, and Brose N. Reduced social interaction and ultrasonic communication in a mouse model of monogenic heritable autism. *Proceedings of the National Academy of Sciences of the United States of America* 105: 1710-1715, 2008.

Janus C. Search strategies used by APP transgenic mice during navigation in the Morris water maze. *Learning & Memory* 11: 337-346, 2004.

Jung S-Y, Kim J, Kwon OB, Jung JH, An K, Jeong AY, Lee CJ, Choi Y-B, Bailey CH, Kandel ER, and Kim J-H. Input-specific synaptic plasticity in the amygdala is regulated by neuroligin-1 via postsynaptic NMDA receptors. *Proceedings of the National Academy of Sciences of the United States of America* 107: 4710-4715, 2010.

Kapfer C, Seidl AH, Schweizer H, and Grothe B. Experience-dependent refinement of inhibitory inputs to auditory coincidence-detector neurons. *Nat Neurosci* 5: 247-253, 2002.

Karpova AY, Tervo DGR, Gray NW, and Svoboda K. Rapid and reversible chemical inactivation of synaptic transmission in genetically targeted neurons. *Neuron* 48: 727-735, 2005.

Kavanagh GL, and Kelly JB. Midline and lateral field sound localization in the albino rat (Rattus norvegicus). *Behav Neurosci* 100: 200-205, 1986.

Kavanagh GL, and Kelly JB. Midline and lateral field sound localization in the ferret (Mustela putorius): contribution of the superior olivary complex. *J Neurophysiol* 67: 1643-1658, 1992.

Kelly JB. Effects of auditory cortical lesions on sound localization by the rat. *J Neurophysiol* 44: 1161-1174, 1980.

Kelly JB, and Glazier SJ. Auditory cortex lesions and discrimination of spatial location by the rat. *Brain Res* 145: 315-321, 1978.

Kelly JB, Judge PW, and Fraser IH. Development of the Auditory Orientation Response in the Albino-Rat (Rattus-Norvegicus). *Journal of Comparative Psychology* 101: 60-66, 1987.

Kelly JB, and Kavanagh GL. Effects of auditory cortical lesions on pure-tone sound localization by the albino rat. *Behav Neurosci* 100: 569-575, 1986.

Kelly JB, and Masterton B. Auditory sensitivity of the albino rat. *J Comp Physiol Psychol* 91: 930-936, 1977.

Kelly JB, and Sally SL. Organization of auditory cortex in the albino rat: binaural response properties. *J Neurophysiol* 59: 1756-1769, 1988.

Kim EJ, and Sheng M. PDZ domain proteins of synapses. *Nature Reviews Neuroscience* 5: 771-781, 2004.

Kim J, Jung S-Y, Lee YK, Park S, Choi J-S, Lee CJ, Kim H-S, Choi Y-B, Scheiffele P, Bailey CH, Kandel ER, and Kim J-H. Neuroligin-1 is required for normal expression of LTP and associative fear memory in the amygdala of adult animals. *Proceedings of the National Academy of Sciences of the United States of America* 105: 9087-9092, 2008.

Kitzes L. Binaural interactions shape binaural response structures and frequency response functions in primary auditory cortex. *Hear Res* 238: 68-76, 2008.

Koka K, Read HL, and Tollin DJ. The acoustical cues to sound location in the rat: measurements of directional transfer functions. *J Acoust Soc Am* 123: 4297-4309, 2008.

Kyweriga M, Stewart W, and Wehr M. Neuronal interaural level difference response shifts are level-dependent in the rat auditory cortex. *J Neurophysiol* 111: 930-938, 2014.

Larson J, and Lynch G. ROLE OF N-METHYL-D-ASPARTATE RECEPTORS IN THE INDUCTION OF SYNAPTIC POTENTIATION BY BURST STIMULATION PATTERNED AFTER THE HIPPOCAMPAL O-RHYTHM. *Brain Research* 441: 111-118, 1988.

Larson J, Wong D, and Lynch G. PATTERNED STIMULATION AT THE THETA-FREQUENCY IS OPTIMAL FOR THE INDUCTION OF HIPPOCAMPAL LONG-TERM POTENTIATION. *Brain Research* 368: 347-350, 1986.

Lechner HAE, Lein ES, and Callaway EM. A genetic method for selective and quickly reversible silencing of mammalian neurons. *Journal of Neuroscience* 22: 5287-5290, 2002.

Lee CC, and Middlebrooks JC. Auditory cortex spatial sensitivity sharpens during task performance. *Nat Neurosci* 14: 108-114, 2011.

Lerchner W, Xiao C, Nashmi R, Slimko EM, van Trigt L, Lester HA, and Anderson DJ. Reversible silencing of neuronal excitability in behaving mice by a genetically targeted, ivermectin-gated Cl(-) channel. *Neuron* 54: 35-49, 2007.

Li N, Gittelman JX, and Pollak GD. Intracellular recordings reveal novel features of neurons that code interaural intensity disparities in the inferior colliculus. *J Neurosci* 30: 14573-14584, 2010.

Lima SQ, Hromadka T, Znamenskiy P, and Zador AM. PINP: a new method of tagging neuronal populations for identification during in vivo electrophysiological recording. *PLoS One* 4: e6099, 2009.

Linden JF, Liu RC, Sahani M, Schreiner CE, and Merzenich MM. Spectrotemporal structure of receptive fields in areas AI and AAF of mouse auditory cortex. *Journal of Neurophysiology* 90: 2660-2675, 2003.

Liu XB, and Jones EG. Localization of alpha type II calcium calmodulin-dependent protein kinase at glutamatergic but not gamma-aminobutyric acid (GABAergic) synapses in thalamus and cerebral cortex. *Proceedings of the National Academy of Sciences of the United States of America* 93: 7332-7336, 1996.

Lord C, Cook EH, Leventhal BL, and Amaral DG. Autism spectrum disorders. *Neuron* 28: 355-363, 2000.

Lu JP, Cui YL, Cai R, Mao YT, Zhang JP, and Sun XD. Early auditory deprivation alters expression of NMDA receptor subunit NRI mRNA in the rat auditory cortex. *Journal of Neuroscience Research* 86: 1290-1296, 2008.

Mansuy IM, and Bujard H. Tetracycline-regulated gene expression in the brain. *Current Opinion in Neurobiology* 10: 593-596, 2000.

Markram H, Toledo-Rodriguez M, Wang Y, Gupta A, Silberberg G, and Wu C. Interneurons of the neocortical inhibitory system. *Nat Rev Neurosci* 5: 793-807, 2004.

Mayford M, Bach ME, Huang YY, Wang L, Hawkins RD, and Kandel ER. Control of memory formation through regulated expression of a CaMKII transgene. *Science* 274: 1678-1683, 1996.

McKirdy J, Sussmann JED, Hall J, Lawrie SM, Johnstone EC, and McIntosh AM. Set shifting and reversal learning in patients with bipolar disorder or schizophrenia. *Psychological Medicine* 39: 1289-1293, 2009.

Messeri P, Eleftheriou BE, and Oliverio A. DOMINANCE BEHAVIOR - PHYLOGENETIC ANALYSIS IN MOUSE. *Physiology & Behavior* 14: 53-58, 1975.

Meyer G, Varoqueaux F, Neeb A, Oschlies M, and Brose N. The complexity of PDZ domain-mediated interactions at glutamatergic synapses: a case study on neuroligin. *Neuropharmacology* 47: 724-733, 2004.

Mickey BJ, and Middlebrooks JC. Representation of auditory space by cortical neurons in awake cats. *J Neurosci* 23: 8649-8663, 2003.

Miller LM, Escabi MA, Read HL, and Schreiner CE. Functional convergence of response properties in the auditory thalamocortical system. *Neuron* 32: 151-160, 2001.

Moore DR, and Irvine DRF. DEVELOPMENT OF SOME PERIPHERAL AND CENTRAL AUDITORY RESPONSES IN THE NEONATAL CAT. *Brain Research* 163: 49-59, 1979.

Moore MJ, and Caspary DM. Strychnine blocks binaural inhibition in lateral superior olivary neurons. *J Neurosci* 3: 237-242, 1983.

Moy SS, Nadler JJ, Magnuson TR, and Crawley JN. Mouse models of autism spectrum disorders: The challenge for behavioral genetics. *American Journal of Medical Genetics Part C-Seminars in Medical Genetics* 142C: 40-51, 2006.

Moy SS, Nadler JJ, Perez A, Barbaro RP, Johns JM, Magnuson TR, Piven J, and Crawley JN. Sociability and preference for social novelty in five inbred strains: an approach to assess autistic-like behavior in mice. *Genes Brain and Behavior* 3: 287-302, 2004.

Nakashiba T, Young JZ, McHugh TJ, Buhl DL, and Tonegawa S. Transgenic inhibition of synaptic transmission reveals role of CA3 output in hippocampal learning. *Science* 319: 1260-1264, 2008.

Ojima H, and Murakami K. Intracellular characterization of suppressive responses in supragranular pyramidal neurons of cat primary auditory cortex in vivo. *Cereb Cortex* 12: 1079-1091, 2002.

Otmakhova NA, Otmakhov N, and Lisman JE. Pathway-specific properties of AMPA and NMDA-mediated transmission in CA1 hippocampal pyramidal cells. *Journal of Neuroscience* 22: 1199-1207, 2002.

Pardo CA, and Eberhart CG. The neurobiology of autism. *Brain Pathology* 17: 434-447, 2007.

Park TJ, Klug A, Holinstat M, and Grothe B. Interaural level difference processing in the lateral superior olive and the inferior colliculus. *J Neurophysiol* 92: 289-301, 2004.

Park TJ, and Pollak GD. GABA shapes sensitivity to interaural intensity disparities in the mustache bat's inferior colliculus: implications for encoding sound location. *J Neurosci* 13: 2050-2067, 1993.

Peca J, Feliciano C, Ting JT, Wang W, Wells MF, Venkatraman TN, Lascola CD, Fu Z, and Feng G. Shank3 mutant mice display autistic-like behaviours and striatal dysfunction. *Nature* 472: 437-U534, 2011.

Penzes P, Cahill ME, Jones KA, VanLeeuwen J-E, and Woolfrey KM. Dendritic spine pathology in neuropsychiatric disorders. *Nature Neuroscience* 14: 285-293, 2011.

Petralia RS, Sans N, Wang YX, and Wenthold RJ. Ontogeny of postsynaptic density proteins at glutamatergic synapses. *Molecular and Cellular Neuroscience* 29: 436-452, 2005.

Philippe A, Martinez M, Guilloud-Bataille M, Gillberg C, Rastam M, Sponheim E, Coleman M, Zappella M, Aschauer H, van Maldergem L, Penet C, Feingold J, Brice A, Leboyer M, and Paris Austim Res Int Sibpair S. Genome-wide scan for autism susceptibility genes. *Human Molecular Genetics* 8: 805-812, 1999.

Phillips DP, and Irvine DR. Some features of binaural input to single neurons in physiologically defined area AI of cat cerebral cortex. *J Neurophysiol* 49: 383-395, 1983.

Phillips DP, Quinlan CK, and Dingle RN. Stability of central binaural sound localization mechanisms in mammals, and the Heffner hypothesis. *Neurosci Biobehav Rev* 36: 889-900, 2012.

Poglia L, Muller D, and Nikonenko I. Ultrastructural Modifications of Spine and Synapse Morphology by SAP97. *Hippocampus* 21: 990-998, 2011.

Pollak GD, Wenstrup JJ, and Fuzessey ZM. Auditory Processing in the Moustache Bats Inferior Colliculus. *Trends in Neurosciences* 9: 556-561, 1986.

Polley DB, Read HL, Storace DA, and Merzenich MM. Multiparametric auditory receptive field organization across five cortical fields in the albino rat. *J Neurophysiol* 97: 3621-3638, 2007.

Ponce A, Bueno E, Kentros C, Vega-Saenz de Miera E, Chow A, Hillman D, Chen S, Zhu LX, Wu MB, Wu XY, Rudy B, and Thornhill WB. G-protein-gated inward rectifier K+ channel proteins (GIRK1) are present in the soma and dendrites as well as in nerve terminals of specific neurons in the brain. *Journal of Neuroscience* 16: 1990-2001, 1996.

Popescu MV, and Polley DB. Monaural Deprivation Disrupts Development of Binaural Selectivity in Auditory Midbrain and Cortex. *Neuron* 65: 718-731, 2010.

Prange O, Wong TP, Gerrow K, Wang YT, and El-Husseini A. A balance between excitatory and inhibitory synapses is controlled by PSD-95 and neuroligin. *Proceedings of the National Academy of Sciences of the United States of America* 101: 13915-13920, 2004.

Ralph GS, Bienemann A, Harding TC, Hopton M, Henley J, and Uney JB. Targeting of tetracycline-regulatable transgene expression specifically to neuronal and glial cell populations using adenoviral vectors. *Neuroreport* 11: 2051-2055, 2000.

Razak KA. Systematic representation of sound locations in the primary auditory cortex. *J Neurosci* 31: 13848-13859, 2011.

Razak KA, and Fuzessery ZM. GABA shapes a systematic map of binaural sensitivity in the auditory cortex. *J Neurophysiol* 104: 517-528, 2010.

Recanzone GH, and Beckerman NS. Effects of intensity and location on sound location discrimination in macaque monkeys. *Hear Res* 198: 116-124, 2004.

Reid RC, and Alonso JM. Specificity of monosynaptic connections from thalamus to visual cortex. *Nature* 378: 281-284, 1995.

Robbins EM, Krupp AJ, de Arce KP, Ghosh AK, Fogel AI, Boucard A, Suedhof TC, Stein V, and Biederer T. SynCAM 1 Adhesion Dynamically Regulates Synapse Number and Impacts Plasticity and Learning. *Neuron* 68: 894-906, 2010.

Rutkowski RG, Wallace MN, Shackleton TM, and Palmer AR. Organisation of binaural interactions in the primary and dorsocaudal fields of the guinea pig auditory cortex. *Hear Res* 145: 177-189, 2000.

Sabin AT, Macpherson EA, and Middlebrooks JC. Human sound localization at near-threshold levels. *Hear Res* 199: 124-134, 2005.

Salminen NH, Tiitinen H, and May PJ. Auditory spatial processing in the human cortex. *Neuroscientist* 18: 602-612, 2012.

Sans N, Prybylowski K, Petralia RS, Chang K, Wang YX, Racca C, Vicini S, and Wenthold RJ. NMDA receptor trafficking through an interaction between PDZ proteins and the exocyst complex. *Nature Cell Biology* 5: 520-530, 2003.

Sara Y, Biederer T, Atasoy D, Chubykin A, Mozhayeva MG, Sudhof TC, and Kavalali ET. Selective capability of SynCAM and neuroligin for functional synapse assembly. *Journal of Neuroscience* 25: 260-270, 2005.

Schapitz IU, Behrend B, Pechmann Y, Lappe-Siefke C, Kneussel SJ, Wallace KE, Stempel AV, Buck F, Grant SGN, Schweizer M, Schmitz D, Schwarz JR, Holzbaur ELF, and Kneussel M. Neuroligin 1 Is Dynamically Exchanged at Postsynaptic Sites. *Journal of Neuroscience* 30: 12733-12744, 2010.

Schiller J, and Schiller Y. NMDA receptor-mediated dendritic spikes and coincident signal amplification. *Current Opinion in Neurobiology* 11: 343-348, 2001.

Scholl B, Gao X, and Wehr M. Nonoverlapping sets of synapses drive on responses and off responses in auditory cortex. *Neuron* 65: 412-421, 2010.

Semple MN, and Kitzes LM. Binaural Processing of Sound Pressure Level in the Inferior Colliculus. *Journal of Neurophysiology* 57: 1130-1147, 1987.

Shao YJ, Wolpert CM, Raiford KL, Menold MM, Donnelly SL, Ravan SA, Bass MP, McClain C, von Wendt L, Vance JM, Abramson RH, Wright HH, Ashley-Koch A, Gilbert JR, DeLong RG, Cuccaro ML, and Pericak-Vance MA. Genomic screen and follow-up analysis for autistic disorder. *American Journal of Medical Genetics* 114: 99-105, 2002.

Shipman SL, and Nicoll RA. A Subtype-Specific Function for the Extracellular Domain of Neuroligin 1 in Hippocampal LTP. *Neuron* 76: 309-316, 2012.

Shipman SL, Schnell E, Hirai T, Chen B-S, Roche KW, and Nicoll RA. Functional dependence of neuroligin on a new non-PDZ intracellular domain. *Nature Neuroscience* 14: 718-U388, 2011.

Skrede KK, and Westgaar.Rh. TRANSVERSE HIPPOCAMPAL SLICE - WELL-DEFINED CORTICAL STRUCTURE MAINTAINED IN-VITRO. *Brain Research* 35: 589-&, 1971.

Stecker GC, Harrington IA, and Middlebrooks JC. Location coding by opponent neural populations in the auditory cortex. *PLoS Biol* 3: e78, 2005.

Stricanne B, Andersen RA, and Mazzoni P. Eye-centered, head-centered, and intermediate coding of remembered sound locations in area LIP. *J Neurophysiol* 76: 2071-2076, 1996.

Sykova E. The extracellular space in the CNS: Its regulation, volume and geometry in normal and pathological neuronal function. *Neuroscientist* 3: 28-41, 1997.

Tallafuss A, Constable JRL, and Washbourne P. Organization of central synapses by adhesion molecules. *European Journal of Neuroscience* 32: 198-206, 2010.

Tan AY, Atencio CA, Polley DB, Merzenich MM, and Schreiner CE. Unbalanced synaptic inhibition can create intensity-tuned auditory cortex neurons. *Neuroscience* 146: 449-462, 2007.

Tan AY, Brown BD, Scholl B, Mohanty D, and Priebe NJ. Orientation selectivity of synaptic input to neurons in mouse and cat primary visual cortex. *J Neurosci* 31: 12339-12350, 2011.

Tan EM, Yamaguchi Y, Horwitz GD, Gosgnach S, Lein ES, Goulding M, Albright TD, and Callaway EM. Reversible inactivation of mammalian neurons in vivo using the Drosophila allatostatin receptor. *Neuron* 51: 157-170, 2006.

Tervo D, and Karpova AY. Rapidly inducible, genetically targeted inactivation of neural and synaptic activity in vivo. *Current Opinion in Neurobiology* 17: 581-586, 2007.

Thomson AM, and Lamy C. Functional maps of neocortical local circuitry. *Front Neurosci* 1: 19-42, 2007.

Tovar KR, and Westbrook GL. The incorporation of NMDA receptors with a distinct subunit composition at nascent hippocampal synapses in vitro. *Journal of Neuroscience* 19: 4180-4188, 1999.

Tsai H-C, Zhang F, Adamantidis A, Stuber GD, Bonci A, de Lecea L, and Deisseroth K. Phasic Firing in Dopaminergic Neurons Is Sufficient for Behavioral Conditioning. *Science* 324: 1080-1084, 2009.

Tsai JJ, Koka K, and Tollin DJ. Varying overall sound intensity to the two ears impacts interaural level difference discrimination thresholds by single neurons in the lateral superior olive. *J Neurophysiol* 103: 875-886, 2010.

van Zundert B, Yoshii A, and Constantine-Paton M. Receptor compartmentalization and trafficking at glutamate synapses: a developmental proposal. *Trends in Neurosciences* 27: 428-437, 2004.

Vicini S, Wang JF, Li JH, Zhu WJ, Wang YH, Luo JAH, Wolfe BB, and Grayson DR. Functional and pharmacological differences between recombinant N-methyl-D-aspartate receptors. *Journal of Neurophysiology* 79: 555-566, 1998.

Vorhees CV, and Williams MT. Morris water maze: procedures for assessing spatial and related forms of learning and memory. *Nature Protocols* 1: 848-858, 2006.

Washbourne P, Liu XB, Jones EG, and McAllister AK. Cycling of NMDA receptors during trafficking in neurons before synapse formation. *Journal of Neuroscience* 24: 8253-8264, 2004.

Wehr M, and Zador AM. Balanced inhibition underlies tuning and sharpens spike timing in auditory cortex. *Nature* 426: 442-446, 2003.

Wesolek CM, Koay G, Heffner RS, and Heffner HE. Laboratory rats (Rattus norvegicus) do not use binaural phase differences to localize sound. *Hear Res* 265: 54-62, 2010.

Wilent WB, and Contreras D. Dynamics of excitation and inhibition underlying stimulus selectivity in rat somatosensory cortex. *Nat Neurosci* 8: 1364-1370, 2005.

Wittenmayer N, Koerber C, Liu H, Kremer T, Varoqueaux F, Chapman ER, Brose N, Kuner T, and Dresbach T. Postsynaptic Neuroligin1 regulates presynaptic maturation. *Proceedings of the National Academy of Sciences of the United States of America* 106: 13564-13569, 2009.

Wu GK, Li P, Tao HW, and Zhang LI. Nonmonotonic synaptic excitation and imbalanced inhibition underlying cortical intensity tuning. *Neuron* 52: 705-715, 2006.

Wu GK, Tao HW, and Zhang LI. From elementary synaptic circuits to information processing in primary auditory cortex. *Neurosci Biobehav Rev* 35: 2094-2104, 2011.

Xu F, Cai R, Xu JH, Zhang JP, and Sun XD. Early music exposure modifies GluR2 protein expression in rat auditory cortex and anterior cingulate cortex. *Neuroscience Letters* 420: 179-183, 2007.

Xu JH, Yu LP, Cai R, Zhang JP, and Sun XD. Early Continuous White Noise Exposure Alters Auditory Spatial Sensitivity and Expression of GAD65 and GABA(A) Receptor Subunits in Rat Auditory Cortex. *Cerebral Cortex* 20: 804-812, 2010.

Yao JD, Bremen P, and Middlebrooks JC. Rat primary auditory cortex is tuned exclusively to the contralateral hemifield. *J Neurophysiol* 110: 2140-2151, 2013.

Yasuda M, and Mayford MR. CaMKII activation in the entorhinal cortex disrupts previously encoded spatial memory. *Neuron* 50: 309-318, 2006.

Ylisaukko-oja T, Rehnstrom K, Auranen M, Vanhala R, Alen R, Kempas E, Ellonen P, Turunen JA, Makkonen I, Riikonen R, von Wendt TN, von Wendt L, Peltonen L, and Jarvela I. Analysis of four neuroligin genes as candidates for autism. *European Journal of Human Genetics* 13: 1285-1292, 2005.

Zhang F, Wang L-P, Brauner M, Liewald JF, Kay K, Watzke N, Wood PG, Bamberg E, Nagel G, Gottschalk A, and Deisseroth K. Multimodal fast optical interrogation of neural circuitry. *Nature* 446: 633-U634, 2007.

Zhang J, Nakamoto KT, and Kitzes LM. Binaural interaction revisited in the cat primary auditory cortex. *J Neurophysiol* 91: 101-117, 2004.

Zhang LI, Tan AY, Schreiner CE, and Merzenich MM. Topography and synaptic shaping of direction selectivity in primary auditory cortex. *Nature* 424: 201-205, 2003.

Zhao S, Cunha C, Zhang F, Liu Q, Gloss B, Deisseroth K, Augustine GJ, and Feng G. Improved expression of halorhodopsin for light-induced silencing of neuronal activity. *Brain Cell Biology* 36: 141-154, 2008.

Zheng CY, Wang YX, Kachar B, and Petralia RS. Differential localization of SAP102 and PSD-95 is revealed in hippocampal spines using super-resolution light microscopy. *Communicative & integrative biology* 4: 104-105, 2011.

Zhiling Y, Fujita E, Tanabe Y, Yamagata T, Momoi T, and Momoi MY. Mutations in the gene encoding CADM1 are associated with autism spectrum disorder. *Biochemical and Biophysical Research Communications* 377: 926-929, 2008.

Zhou Y, Liu BH, Wu GK, Kim YJ, Xiao Z, Tao HW, and Zhang LI. Preceding inhibition silences layer 6 neurons in auditory cortex. *Neuron* 65: 706-717, 2010.

Zhou Y, and Wang X. Level dependence of spatial processing in the primate auditory cortex. *J Neurophysiol* 108: 810-826, 2012.

Zoghbi HY. Postnatal neurodevelopmental disorders: Meeting at the synapse? *Science* 302: 826-830, 2003.